Ionospheric Clutter Models for High Frequency Surface Wave Radar

by

© *Shuyan Chen*, B. Eng., M. Eng.

A thesis submitted to the

School of Graduate Studies

in partial fulfilment of the

requirements for the degree of

Doctor of Philosophy

Faculty of Engineering and Applied Science

Memorial University of Newfoundland

May 2017

St. John's Newfoundland

Abstract

High frequency surface wave radar (HFSWR), operating at frequencies between 3 and 30 MHz, has long been employed as an important ocean remote sensing device. These high frequency (HF) radars can provide accurate and real-time information for sea state monitoring and hard-target detection, which is greatly beneficial for planning and executing oceanographic projects, search and rescue events, and other commercial marine activities. Ideally, in HFSWR operation, the radio waves may be coupled with ocean waves and propagate along the curvature of the ocean surface with ranges well beyond 200 km. However, during transmission, a portion of the radar radiation may travel upwards to the ionosphere from the transmitting antenna. This may be partially reflected back to the receiving antennas directly (vertical propagation) or via the ocean surface (mixed-path propagation). This ionospheric clutter may significantly impact the performance of HFSWR. Furthermore, the high intensity and random behaviour of the ionospheric spectral contamination of radar echoes make the suppression of this kind of clutter challenging.

In this thesis, comprehensive theoretical models of the ionospheric clutter are investigated. The physical influences of the ionospheric electron density on HF radar Doppler spectra are taken into account in the ionospheric reflection coefficient. Next, based on previous modeling involving the scattering of HF electromagnetic radiation from the ocean surface and a first-order mixed-path propagation theory, the second-order received electric field for mixed-path propagation is derived for a monostatic radar configuration. This is done by considering the reflection from the ionosphere and scattering on the ocean surface with second-order sea waves. Then, the field integrals are taken to the time domain, with the source field being that of a vertically polarized pulsed dipole antenna. Subsequently, the

second-order received power model is developed by assuming that the ocean surface and the ionosphere may be modeled as stochastic processes.

The ionospheric clutter model including a pulsed radar source is further investigated for the case of vertical propagation for a monostatic configuration and mixed-path propagation for a bistatic configuration.

Next, a theoretical mixed-path propagation model is developed by involving a frequency-modulated continuous waveform (FMCW) radar source.

In order to investigate the power spectrum of the resulting ionospheric clutter and its relative intensity to that of the first-order ocean clutter, the normalized ionospheric clutter power is simulated. Numerical simulation results are provided to indicate the performance of the ionospheric clutter under a variety of radar operating parameters, ionospheric conditions and sea states.

Acknowledgements

The challenging journey of pursuing my PhD has provided a wonderful and enjoyable collection of precious memories thanks to the inspiration and support of numerous people. My sincere thanks to all of you for being part of my PhD journey and making this thesis possible.

First and foremost I would like to express my deepest gratitude to my supervisors, Dr. Weimin Huang and Dr. Eric Gill, for their professional guidance and continuous academic and financial support throughout my research period. They have inspired me with their enthusiasm for research, and helped me to overcome difficulties at various key stages in my work with their deep insights and constructive suggestions. I feel fortunate to have had the opportunity to work with them. My PhD research was supported by Natural Sciences and Engineering Research Council of Canada grants (NSERC) and an Atlantic Innovation Fund (AIF) to my supervisors. I also appreciate my supervisory committee member, Dr. Cecilia Moloney, for providing helpful advice and discussions on my research. Further, my sincere respect goes to Dr. John Walsh for his sheer brilliance and outstanding contributions to HF radar oceanic remote sensing. His works have allowed me to further explore this area by being able to “stand on the shoulders of giants”.

I am indebted to present and past members of our radar group for providing a stimulating and comfortable environment in which to learn and grow. I also wish to thank all my lovely friends in St. John’s. They have brought me many delightful and memorable moments, and enriched my spare time during the last four years.

Finally, special thanks to my loving family: my father, Zhong Chen, my mother, Yan Sun, and my husband, Zhi Li, for all of your unconditional love and care, and constant

encouragement and understanding. I do not tell you often enough how lucky and grateful I am to have you in my life. Love you forever.

Contents

List of Figures

Table of Symbols and Abbreviations

The page numbers here indicate the place of first significant reference. Although not all symbols are explicitly referenced below, their definitions are obvious from the context.

Symbols

E_{0n}^{+}	Electric field normal to the rough surface immediately above the surface (P. 15).
$\varepsilon(x, y)$	Surface roughness profile at position (x, y) (P. 15).
$F(\rho)$	Sommerfeld surface attenuation function with $\rho = \sqrt{(x^2 + y^2))}$ (P. 16).
k	Wavenumber of the transmitted electromagnetic wave (P. 16).
$\mathcal{F}_{xy}$	Two dimensional (x, y) spatial Fourier transform (P. 16).
$\mathcal{F}_{xy}^{-1}$	Two dimensional spatial inverse Fourier transform (P. 16).
$\vec{E}_s$	Primary source vector electric field (P. 16).
$\vec{J}_s$	Primary source current density of the transmitting antenna (P. 16).
G_0	Green's function (P. 16).
Δ	Ocean surface impedance (P. 17).

C_0	Dipole coefficient for an antenna (P. 18).
Δl	Length of the dipole (P. 18).
I	Current of the dipole (P. 18).
ω	Radian frequency of the transmitted radio wave (P. 18).
η_0	Intrinsic impedance of the free space (P. 18).
$z = H/2$	Height of the ionospheric reflection (P. 20).
θ_i	Incidence angle on the ionosphere (P. 20).
ρ	Range of the surface wave path (P. 20).
R	Range of the free-space path (P. 20).
$R_i(x, y)$	Ionospheric reflection coefficient at surface observation point (x, y) (P. 20).
$(E_{0n}^{+})_1$	First-order component of the received electric field (E_{0n}^{+}) (P. 21).
$P_{\vec{K}_o}^{o}$	Fourier coefficient of ocean waves (P. 22).
$\vec{K}_o$	Wavenumber of ocean waves (P. 22).
$P_{\vec{K}_i}^{i}$	Fourier coefficient of the ionosphere reflection coefficient (P. 23).
K_i	Wavenumber of the ionospheric reflection coefficient (P. 23).
ρ_s	Apparent surface range (P. 24).
$h(\cdot)$	Heaviside function (P. 24).

$\Delta\rho_s$	Apparent range resolution (P. 24).
$Sa(\cdots)$	Sampling function with the usual form of $\sin(\cdots)/(\cdots)$ (P. 24).
$\Delta\rho$	Range resolution of the surface scattering patch (P. 24).
$P_i(\omega_d)$	Doppler power spectral density of the received electric field for ionospheric clutter where ω_d is the Doppler frequency (P. 25).
A_r	Receiving antenna effective area (P. 25).
$S_o(\vec{K}_o, \omega_o)$	Spectral density of the ocean surface waves (P. 25).
$S_i(\vec{K}_i, \omega_i)$	Spectral density of the ionospheric reflection coefficient (P. 25).
n	Refractive index (P. 33).
ω_p	Electron plasma frequency of the ionosphere (P. 33).
N_e	Electron density of the ionosphere (P. 33).
R_{ia}	Ionospheric absorption (P. 36).
ν	Collision frequency (P. 36).
μ	Magnetic permeability (P. 36).
$\mathcal{R}(\vec{r}, \tau)$	Spatial and temporal autocorrelation function (P. 39).
Φ	Phase error function of the ionospheric reflection coefficient (P. 37).
S_{Ne1}	Spectral density of the small-scale electron density irregularities (P. 40).

v_h Horizontal ionospheric plasma drift velocity (P. 41).

v_v Vertical ionospheric plasma drift velocity (P. 41).

P_{o1} Power spectrum of the first-order ocean clutter (P. 44).

$(E_{0n}^{+})_2$ Second-order component of the received electric field (E_{0n}^{+}) (P. 57).

(μ, δ) Elliptical coordinates (P. 60).

${}_E\Gamma_P$ Electromagnetic coupling coefficient for mixed-path patch scatter (P. 66).

${}_H\Gamma_P$ Hydrodynamic coupling coefficient for second-order ocean waves (P. 67).

ρ_{RT} Distance between transmitter and receiver for bistatic case (P. 90).

B Sweep bandwidth of FMCW signal (P. 108).

T_r Sweep interval of FMCW signal (P. 108).

Abbreviations

HFSWR High Frequency Surface Wave Radar (P. 1).

HF High Frequency (P. 1).

UTC Coordinated Universal Time (P. 4).

HPA Horizontally Polarized Antennas (P. 9).

VPA Vertically Polarized Antennas (P. 9).

2-D Two-Dimensional (P. 10).

OTH	Over-the-Horizon (P. 11).
GLRT	Generalized Likelihood Ratio Test (P. 11).
STAP	Space-Time Adaptive Processing (P. 10).
JDL	Joint Domain Localized (P. 11).
D3	Direct Data Domain (P. 11).
FFA	Fast Fully Adaptive (P. 11).
CPI	Coherent Pulse Interval (P. 13).
IRC	Ionospheric Reflection Coefficient (P. 20).
PM	Pierson-Moskowitz (P. 27).
PSD	Power Spectral Density (P. 25).
TID	Travelling Ionospheric Disturbance (P. 38).
FMCW	Frequency-Modulated Continuous Wave (P. 107).

Chapter 1

Introduction

1.1 Research Rationale

With the rapid development of marine-related enterprises, a significant challenge is to obtain accurate and comprehensive oceanographic information to support operations on the ocean. The complex and varying ocean conditions significantly affect the operational efficiency and safety of marine activities. Moreover, ocean state information would highly benefit the physical oceanography community [1].

High frequency surface wave radar (HFSWR) is a shore-based remote sensing system used to measure temporal and spatial ocean surface properties. Its successful application for sea state monitoring is based on the underlying relationship between radar sea-echo Doppler spectra and ocean surface characteristics [2]. The transmitted signals in the high frequency (HF) band (3 - 30 MHz) interact strongly with the ocean waves of decametric wavelengths. The highly conductive ocean surface allows the HF radiation to propagate along the curvature of the air-water interface to ranges well beyond 200 km [3, 4] depend-

ing on the actual operating frequency and power. The backscattered signals potentially contain significant information regarding the ocean dynamic characteristics. Therefore, by analysing the received Doppler spectra, various sea parameters, including surface current fields, wave directions, significant wave height, and wind velocities may be extracted from the radar returns [5–7]. These attributes make HFSWR an attractive tool for the remote sensing of sea state parameters. Aside from ocean parameters, HF radar is also used to determine the position, speed, and track of hard targets such as ships and icebergs.

The performance of HFSWR in an ocean environment may be impacted significantly by the existence of the ionosphere [8, 9]. The ionosphere surrounds the earth at a height of 50 to 500 km and protects the earth from the sun's dangerous radiation (extreme ultra-violet and X-ray). In the ionosphere, gases are ionized into free electrons and ions by intense solar and cosmic radiation. The ionosphere is often characterized as consisting of several stratified layers due to different levels of ionization. These layers are denoted as D (at altitudes between 50 to 90 km), E (90-150 km) and F (150-500 km). Additionally, the Sporadic-E (Es) layer is an erratically occurring layer that forms at E-region heights at higher electron density levels [10]. Due to their differing air and electron densities, the various layers have different effects on electromagnetic waves propagating within or through them. For example, because of high air density and low electron density of the D layer, the HF radio waves at lower frequencies (3-6 MHz) may be absorbed by the D layer via high collision frequencies between the electrons and neutrons, and those at higher frequencies may penetrate through it and be partly reflected or refracted by the E layer. In contrast, the F layer with low air density and high electron density is able to entirely reflect HF radio waves [11]. More specifically, the maximum frequency of the radio wave reflected

by a layer at vertical incidence, referred to as the layer critical frequency, is a function of the electron density. The relationship between the layers' critical frequencies and the heights at which signals are reflected from different layers can be found in a vertical incidence ionogram, which is obtained by an ionosonde [12]. The maximum frequency that can be reflected at oblique incidence from a particular layer is related to both the incidence angle and the layer critical frequency. During the day time, HF signals may be attenuated due to the existence of the D layer or reflected by higher layers. At night, the D and E layers virtually disappear since the solar radiation is blocked by the Earth. Then, HF signals arriving at the F layer may be reflected toward the ground with low losses, and sometimes HF signals are reflected from the Es layer before reaching the F layer. This characteristic has been utilized for long distance HF skywave communication. On the other hand, it may cause ionosphere clutter problems for surface wave radar.

Ideally, in HFSWR operation, it is desirable that the radio waves propagate horizontally along the ocean surface. However, due to constraints on antenna design and operational features, sometimes including complicated ground plane characteristics and wind-induced antenna motion, a portion of the radio waves is radiated upwards to the ionosphere. Under certain conditions, partial upward-radiated signal energy may then be reflected back from different ionospheric layers to the receiving antennas directly (vertical reflection) or via the ocean surface (ionosphere-ocean or mixed-path propagation). The two feasible propagation paths for the ionospheric clutter are shown in Figure 1.1. It should be noted that the term "mixed-path" in this thesis refers to a combination of ionosphere reflection and ocean scattering, which is different from its earlier meaning of land-sea transitions in surface wave propagation (e.g., [13]). When scattering from the ionosphere with dynamic electron den-

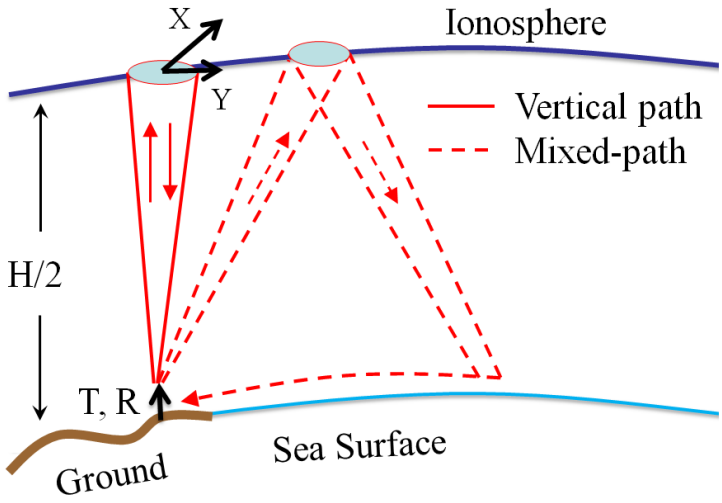

Figure 1.1: Propagation paths for ionospheric clutter.

sity irregularities, the returned echoes may be significantly spread in Doppler and range. This clutter may contaminate significant portions of the range-Doppler spectra and seriously impair the remote sensing capabilities at a range beyond 200 km or target detection performance beyond 300 km [14].

The left column of Figure 1.2 provides two examples of radar range-Doppler spectra based on data collected by a HFSWR operating at 4.1 MHz at Cape Race, NL, Canada on August 29, 2000 at 18:00 coordinated universal time (UTC) and August 30, 2000 at 02:00 UTC, respectively [15]. The right column of Figure 1.2 gives the corresponding ionograms obtained by the ionosonde located within a kilometer of the HFSWR at Cape Race. As shown in Figure 1.2(a), the radar range-Doppler spectrum involves ionospheric clutter from the Es layer at range bins from 100 to 125 km. The corresponding ionogram in Figure 1.2(b) displays an intense Es layer appears at a height of roughly 100 km and may reflect the radio waves with frequencies from 2 to 7 MHz. The ionospheric clutter due to vertical reflection appears in an interval of 5 to 10 km at the nearer range of the ionospheric clutter (100 to

110 km). The ionospheric clutter due to mixed-path propagation, involving the additional propagation along the sea surface, appears at further range bins (110 to 125 km). This Es layer ionospheric clutter reduces the performance of HFSWR at these ranges [16]. Figure 1.2(c) contains the F layer ionospheric clutter occurring from 310 to 330 km. This agrees with the ionogram shown in Figure 1.2(d), indicating that the radio wave with frequency of 4.1 MHz at vertical incidence is reflected at a height of 310 km. The separate traces of the F layer are associated with the F layer ordinary and extraordinary waves due to the existence of the Earth's magnetic field. The absence of E-layer clutter above 3.5 MHz allows the radar to have longer range detection performance. Specifically, radar echo Doppler spectra at particular ranges involving ionospheric clutter due to (a) vertical reflection and (b) mixed-path propagation are shown in Figure 1.3(a) and (b), respectively. These spectra were collected by an HF radar installation at Cape Race, Newfoundland, on January 6, 2002 at 20:00 UTC. The radar frequency was 4.1 MHz. In Figure 1.3(a), the continuum surrounding "-0.31 Hz" is due to direct reflection of the transmitted signal from the overhead F-layer ionosphere with a height of 230.8 km and the peak at "0.2 Hz" is the Bragg peak of the sea clutter. The power of the reflection from the F-layer is spread over a Doppler region of about 1 Hz. At ranges beyond 200 km, the Bragg sea-clutter components are relatively small compared with the F-layer reflection. Although the peak magnitude of ionospheric clutter due to mixed-path propagation in Figure 1.3(b) is relatively lower than that due to vertical reflection, the former is strong enough to contaminate the first-order sea clutter. Furthermore, this ionospheric clutter is subject to diurnal and seasonal variations as a result of temporal and spatial variations of the atmospheric layers [3].

For successful sea-state monitoring and target detection, HFSWR systems require target

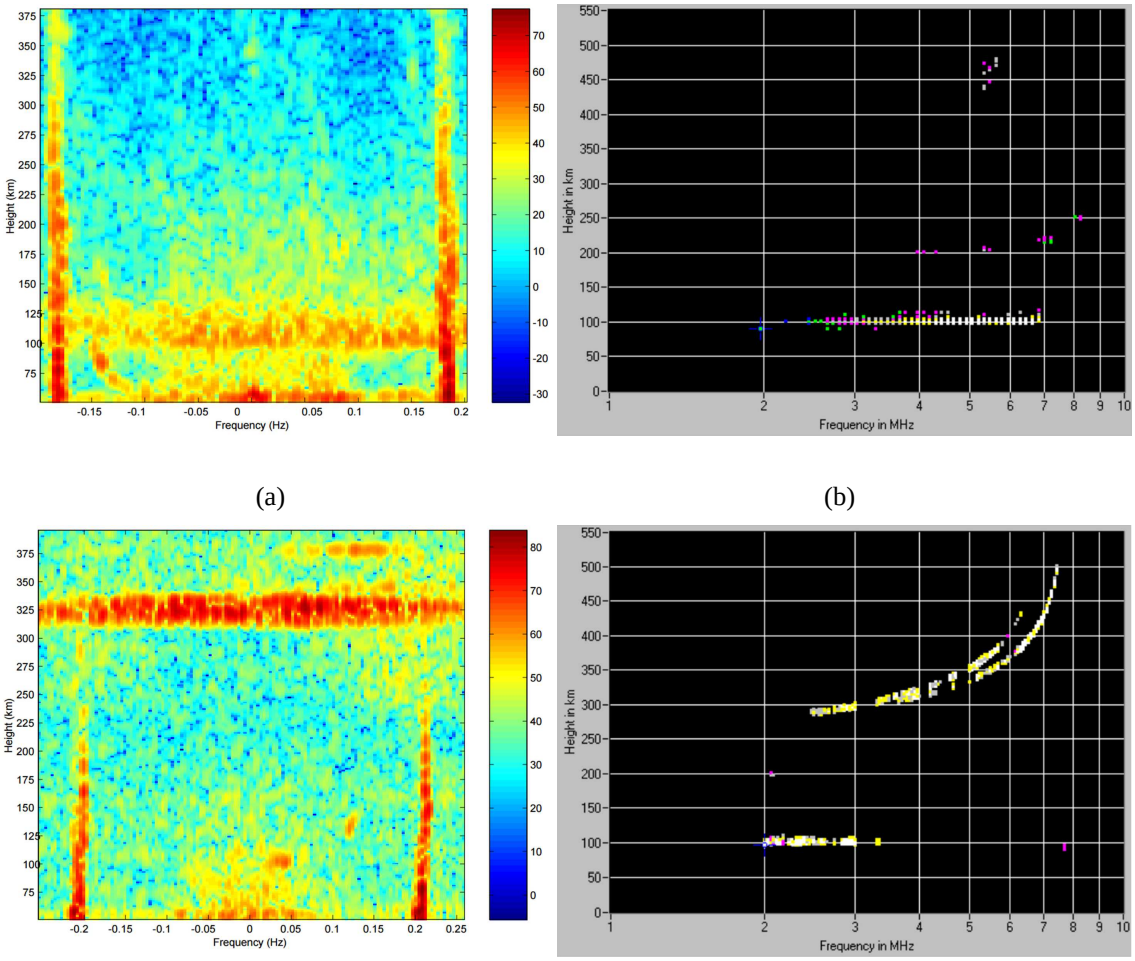

Figure 1.2: Radar range-Doppler spectra (a), (c) based on the data collected at Cape Race, NL, Canada on August 29, 2000 at 18:00 UTC and August 30, 2000 at 02:00 UTC, respectively, and their corresponding ionograms (b), (d) [14].

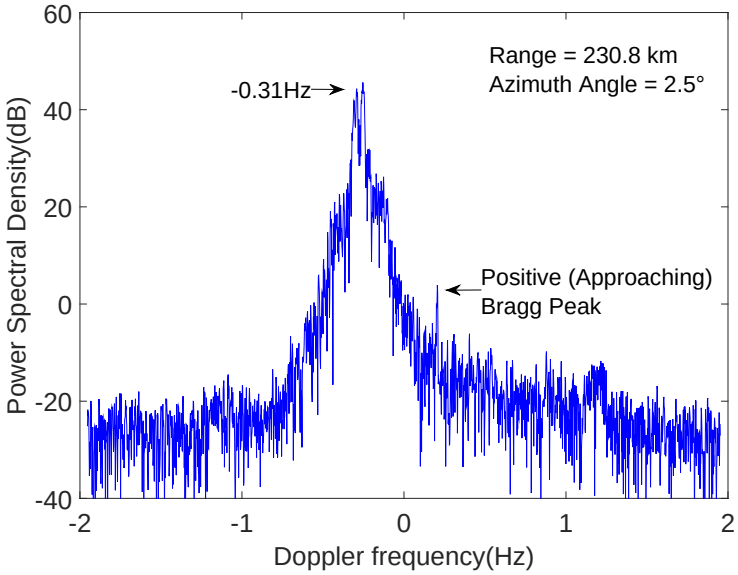

(a) Vertical reflection

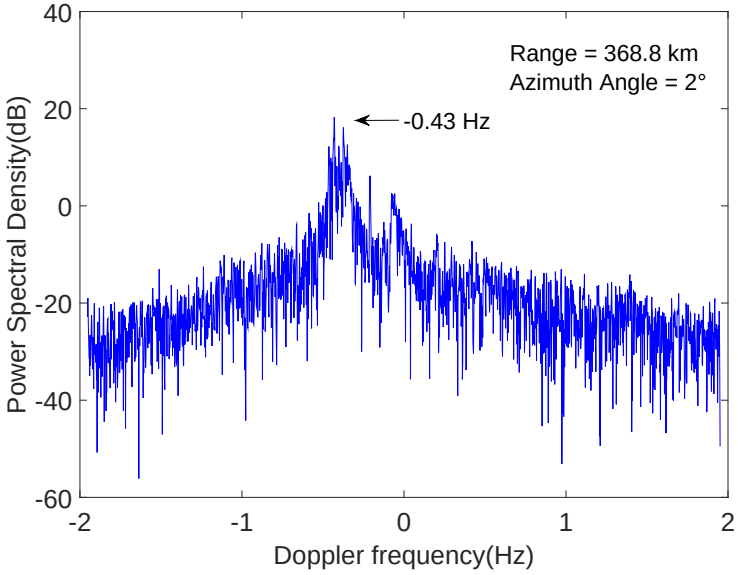

(b) Mixed-path propagation

Figure 1.3: Radar Doppler spectra based on the data collected at Cape Race, NL, Canada on January 6, 2002 at 20:00 UTC involving ionospheric clutter reflected from the F-layer for the case of (a) vertical reflection and (b) mixed-path propagation.

signals to be well separated from clutter in range and Doppler. Therefore, to improve the performance and the reliability of an HFSWR system, particularly during night time operation, it is necessary to find methods to distinguish the unwanted signals from the received ocean scatter. In addition to understanding the clutter in order to mitigate its effects on ocean Doppler spectra, this knowledge may also provide a valuable source for investigating the characteristics of the ionosphere itself [17].

The major focus in this thesis is on exploring how the ionosphere affects the propagation of the transmitted HF signals and the ionospheric clutter characteristics in the Doppler spectra of the radar echoes in the context of ocean remote sensing. A comprehensive model of the radar received power density incorporating ionospheric clutter from mixed-path and vertical propagation modes is developed. This work may lead to a better characterization of the ionospheric clutter at HF and provide theoretical foundations for enhanced suppression schemes.

1.2 Literature Review

This section reviews some of the previous work addressing the unwanted ionospheric clutter in the context of HFSWR. Research efforts have generally taken one of two approaches: developing ionospheric clutter suppression methods, or modelling the ionospheric clutter.

1.2.1 Methods for ionospheric clutter suppression

While not the primary focus of this thesis, a brief discussion on ionospheric clutter suppression is warranted for the sake of completeness.

Based on the mechanism of ionospheric reflection, the intensity of ionospheric clutter is sensitive to the radar operating frequency. If the operating frequency is increased beyond the critical frequency of a particular ionospheric layer, the upward HF signal will not be reflected back to the ground [18]. However, for long-range sea state measuring and ship detection, it is desirable to operate the radar at lower HF frequencies, since there will be more surface-wave attenuation at higher frequencies. Thus, there is a tradeoff in applying frequency agility to evade the interference. In order to improve the reliability of an HFSWR system, several approaches have been exploited to mitigate the influences of the ionospheric clutter.

Several adaptive processing techniques [19–22] are developed by employing horizontal or vertical dipoles as auxiliary antennas to take on the role of coherent sidelobe cancellers. These techniques may adaptively control the amplitude and phase of the signal from each array element in order to nullify interfering signals and maintain the response in the direction of the desired signal. In [19], Leong presented a method employing four auxiliary horizontally polarized antennas (HPA), configured in the form of two separate crosses, to form an adaptive system with the vertically polarized antennas (VPA) of a HFSWR system. The horizontally polarized components received by the HPAs can be used to estimate the interference component received by the VPAs. A subtraction of this estimate from the outputs of the VPAs can then result in interference cancellation. Leong derived adaptive weights to optimally suppress interference. However, in practice, sea echo from the horizontal direction and the ionospheric clutter from the zenith direction cannot be easily separated by this method. Therefore, the adaptive filtering process may lead to simultaneous weakening of the target signal.

Further efforts were made in [23] to investigate the angular spectrum characteristics of ionospheric clutter and to deduce the signal-to-clutter processing gain from this information by various adaptive receive antenna array configurations. In particular, it is shown that by using a planar two-dimensional (2-D) array, the radar can distinguish high-elevation ionospheric clutter signals from low-elevation surface target echo, such as sea echo. These methods involved additional antennas and relied on a large array aperture or a 2-D array configuration, making the radar system more complicated and reducing its applicability when the size of the test site is limited.

Other researchers have applied a signal processing technique called space-time adaptive processing (STAP) algorithms. This is an effective way to use training samples to adapt its algorithms to specifically suppress the ionospheric clutter component. The concept of STAP was proposed by Brennan and Reed in the 1970s [24]; in the Doppler-angle domain it has been mainly exploited to suppress homogeneous and nonhomogeneous clutter for airborne radar systems [25]. STAP involves a two-dimensional filtering technique using a phased-array antenna with multiple spatial channels. Coupling multiple spatial channels with a pulse-Doppler waveform leads to the name “space-time”. Applying the statistics of the interference environment, an adaptive STAP weight vector may be formed. This weight vector is then applied to the coherent samples received by the radar to deal with the interference problem.

In HFSWR systems, STAP has recently been adopted to counter sea clutter in ship-borne radar systems [26] and to suppress ionospheric clutter in shore-based radar systems. Giuseppe Fabrizio and his colleagues at the Defence Science and Technology Organization in Australia focused on the development of the adaptive coherence estimator (ACE) and

its variant, the spatial adaptive subspace detector (ASD) [27], for over-the-horizon (OTH) radar systems. The ACE and ASD tests satisfy the constant false alarm rate property. This property is used to determine the power threshold above which any return can be considered to originate from a target with a particular probability. However, the techniques are susceptible to unwanted signals present in the test cell but not in the reference cell. Such signals can cause masking of desired signals and preclude their detection. Recently, Fabrizio and Farina proposed a generalized likelihood ratio test (GLRT) detector to address this issue [28]. However, the implementation of the GLRT requires exact knowledge of the parameters of the interference.

Saleh and his colleagues [29, 30] in Canada, and Li and Zhang $etal.$ [31, 32] in China analyzed a group of STAP algorithms. These include the joint domain localized (JDL), the direct data domain (D3), hybrid, as well as a newly proposed fast fully adaptive (FFA) algorithm. JDL is a dimension-reduced version of STAP, which features low computational cost and high performance in homogeneous clutter suppression. Especially for clutter with distribution independent with the desired signal, JDL is highly effective. In HFSWR, it is always difficult to obtain enough training data for JDL. The D3 and hybrid techniques are STAP algorithms used for suppressing non-homogeneous clutter. These algorithms suffer from high computational cost and poor real-time performance for HFSWR due to the requirement of long coherent integration time and a large space-time dimension. FFA is presented in [30] and tested based on a Cape Race data set provided by Defence Research and Development Canada. This algorithm is able to exploit the entire space-time data set with limited training and with low computation load, but the issue of how to divide the space-time region into rectangular sub-matrices is still under investigation.

These existing signal processing techniques for mitigating ionospheric clutter require a tradeoff between computation load and the homogeneity of the sample support needed to train the adaptive filters. Furthermore, these techniques are usually more suitable for processing the steady or slowly varying disturbances of the ionospheric clutter than for dynamic applications. These motivate the research reported in this thesis.

1.2.2 Overview for ionospheric clutter modeling

A second approach to alleviating the ionospheric clutter problem involves describing the complicated physical scattering mechanisms based on a well-defined mathematical model. This model should explain the interactions of the radar signals and the ocean waves, and, additionally, it must address how the ionosphere affects the received signal. Such a model might then suggest how the ionospheric clutter might be analytically characterized within the radar echo spectrum. Due to the highly non-stationary characteristics of the ionosphere which vary widely with time of day, season, temperature, and location, modeling the ionospheric clutter is challenging. The level of ionization and the electron density are functions of both elevation and solar radiation intensity. As a result the electron density of the ionosphere, and consequently the characteristics of the ionospheric clutter, vary with elevation as well as time of day, season, and sun-spot activity.

For his Ph.D. thesis in 2000, Fabrizio introduced a space-time statistical model of narrowband signals reflected by different ionospheric layers and developed a parameter estimation technique to fit measured data into the model [33]. First, he derived a mathematical expression for the received signal-fields reflected by a constant structure of the irregular ionosphere at a time instant. This rough plasma surface was replaced by a series of flat

"phase screens" in the X-Y plane. Then, he determined the statistical properties of the wavefield received on the ground in terms of the space-time autocorrelation of the time-varying irregular ionosphere. This model is shown to be valid for the cases with a coherent pulse interval (CPI) shorter than a few seconds. For longer CPIs, he assumed the ionospheric reflections as a random process with a Gaussian representation and proposed hypothesis tests to evaluate this statistical model. One should emphasize that the parameters of the ionospheric model were experimentally validated from the field data collected at the Jindalee radar site operated by the Defense Science and Technology Organization (DSTO) in Australia. There was no guarantee that this model will be applicable to other HFSWR systems. Furthermore, this model does not involve the process of sea surface scattering via the ionosphere-ocean path, which can be significant for coastal HFSWR and should be considered.

Riddolls [34] introduced a geometric optics model, which was extended from the sky-wave model proposed by Coleman [35]. The scattered wave field was expressed in terms of a line integral of the refractive index fluctuations by simultaneously accounting for group delay, direction of arrival, location, and Doppler shift. He used a ray tracing model and treated ionospheric irregularities as perturbations of a "quiescent" path solution without irregularities. Finally, he built the relationship between the phase power spectrum for the signal received in the horizontal plane and the spectral density of the electron density irregularities within the ionosphere. This model was recently implemented by Ravan *et al.* [36] to develop a spatial-temporal phase spectrum of HF signals reflected from the ionosphere vertically or obliquely. However, the model did not provide the received power spectral density of the ionospheric clutter and also did not involve sea scattering via the ionosphere-

ocean path.

Walsh and Gill of the radar group at Memorial University in Canada laid a solid theoretical foundation for analyzing the monostatic and bistatic HF radar cross sections of the sea surface scattering for oceanic remote sensing [37–39]. The radar cross section is used to describe the physical mechanism of the sea surface to reflect radar energy. These first- and second-order models were derived using the general Maxwell equations to solve for the received electric fields, and then the received power density and the radar cross section are obtained through a series of Fourier transformation and statistical analysis. The models have been proven to be efficient in algorithms used for extracting ocean parameters from HFSWR data. Based on this theory, the first-order model has been extended to mixed-path ionosphere clutter modelling for a pulsed radar [40,41]. In these references, the effect of the ionosphere on the radio waves travelling within it was assumed to be a Gaussian process. However, the spectral density of this process was simplified to a uniform or exponential distribution without experimental verification, which may not be sufficient for describing the practical ionospheric conditions. The methodology of Walsh's mixed-path model is introduced in details in Section 1.2.3. In this thesis, it will be modified by considering more practical ionospheric conditions.

Comprehensive characteristics of ionospheric clutter are analysed by Chan [42]. His report includes various types of ionospheric clutter which were identified based on time-series mode and Doppler mode data collected at Cape Race, Newfoundland, Canada in 2003. The characteristics were catalogued in terms of the range, azimuth, frequency, and Doppler. The information provided in that report may be used for evaluating and testing the derived model of ionospheric clutter.

1.2.3 Review of Walsh's mixed-path propagation theory

The analysis of the mixed-path propagation was conducted based on the previous modeling involving the scattering of HF electromagnetic radiation from the ocean surface. Barrick [43] was the first to derive a complete radar cross section model for investigating the interaction between HF radar waves and ocean waves. It should be noted that the Bragg scatter mechanism in his techniques are simply accounted for by Dirac delta function, which is not the case in real radar Doppler spectra. Srivastava and Walsh [44] first addressed the Bragg peak broadening phenomenon by studying the mechanism of electromagnetic wave scattering at the boundary of two different media. Their analysis proceeded directly from Maxwell's equations and these solutions showed the boundary conditions were generated naturally from the initial formulation as auxiliary equations. Walsh and his colleagues [37, 45] further applied this basic approach to develop a variety of cross section models for different practical situations of ocean surface propagation and scattering. The mixed-path propagation is one of the applications, which is addressed by additionally involving the scattering of the HF radio waves from the ionosphere.

For the case of ionospheric clutter returning to the receiving antennas via ionosphere-ocean mixed-path propagation, the derivation begins from the rough surface scattering integral equation found in Eq. (46) of [37] as

$$\begin{aligned} &E_{0n}^{+} - \nabla\varepsilon \cdot \nabla(E_{0n}^{+}) \overset{xy}{*} F(\rho)\frac{e^{-jk\rho}}{2\pi\rho} \\ =&(\hat{z} - \nabla\varepsilon) \cdot \mathcal{F}_{xy}^{-1}[2u\mathcal{F}_{xy}(\vec{E}_{s}^{z^-})e^{-z^- u}] \overset{xy}{*} F(\rho)\frac{e^{-jk\rho}}{2\pi\rho}, \end{aligned} \tag{1.1}$$

where E_{0n}^{+} is the received electric field normal to the rough surface immediately above the surface, $\varepsilon(x, y)$ is the surface roughness profile at position (x, y), $\nabla\varepsilon$ is the surface gradient,

$\overset{xy}{*}$ is a two dimensional (x, y) convolution, $\rho = \sqrt{x^2 + y^2}$ is the planar distance variable, $F(\rho)$ is the Sommerfeld surface attenuation function, k is the electromagnetic wavenumber, $\hat{z}$ is the unit vector in the z (vertical) direction, $\mathcal{F}_{xy}$ is a two dimensional (x, y) spatial Fourier transform, $\mathcal{F}_{xy}^{-1}$ is the inverse transform operator, $u = \sqrt{K^2 - k^2}$, $K^2 = K_x^2 + K_y^2$, K_x and K_y are spatial Fourier transform variables, and $\vec{E}_s^{z^-}$ is the incidence electric field of the primary source vector evaluated in the plane $z = z^- < \varepsilon(x, y)$. This equation describes the process of the radio waves scattering at sea surface point (x, y) and propagating on the sea surface for a distance of ρ, and gives the relationship between the incidence and received electric field.

The general form of the primary source field $\vec{E}_s$ at a point (x, y, z) in free space is defined as [46]

$$\vec{E}_s(x, y, z) \equiv T_{sE}(\vec{J}_s(x, y, z)) \overset{xyz}{*} G_0(x, y, z), \tag{1.2}$$

where, $\vec{J}_s$ is the primary source current density of the transmitting antenna, $T_{sE}(\vec{J}_s) = \frac{1}{(j\omega\varepsilon_0)}[\nabla(\nabla \cdot \vec{J}_s) + k^2\vec{J}_s]$, $\overset{xyz}{*}$ is three dimensional (x, y, z) spatial convolution, $G_0 = \frac{e^{-jkr}}{4\pi r}$ is the Green's function, and $r = \sqrt{x^2 + y^2 + z^2}$ is the three dimensional radial distance variable. Taking the two dimensional (x, y) spatial Fourier transform of Eq. (1.2), the integral form of the source field at the plane $z = z^-$ is given as

$$\vec{E}_s(z^-) = e^{z^- u} \int_{z'} T_{sE}(z') \frac{e^{-z'u}}{2u} dz'. \tag{1.3}$$

The expression $2u\mathcal{F}_{xy}(\vec{E}_s^{z^-})e^{-z^- u}$ in Eq. (1.1) becomes

$$2u\mathcal{F}_{xy}(\vec{E}_s^{z^-})e^{-z^- u} = 2 \lim_{z \to 0^+} \frac{\partial}{\partial z} \mathcal{F}_{xy}(\vec{E}_s). \tag{1.4}$$

Substituting Eq. (1.4) into Eq. (1.1) yields

$$E_{0n}^{+} - \nabla\varepsilon \cdot \nabla(E_{0n}^{+}) \overset{xy}{*} F(\rho)\frac{e^{-jk\rho}}{2\pi\rho} = (\hat{z} - \nabla\varepsilon) \cdot 2 \lim_{z\to 0^{+}} \frac{\partial}{\partial z}(\vec{E}_s) \overset{xy}{*} F(\rho)\frac{e^{-jk\rho}}{2\pi\rho}. \quad (1.5)$$

The $\hat{z}$ component of the source term may be further simplified to

$$\begin{aligned} E_{szs} &= \mathcal{F}_{xy}\left[2 \lim_{z\to 0^{+}} \frac{\partial}{\partial z}(\vec{E}_s) * F(\rho)\frac{e^{-jk\rho}}{2\pi\rho}\hat{z}\right] \\ &= \int_{z'} T_{sEz}(z')\frac{e^{-z'u}}{u + jk\Delta}dz', \end{aligned}$$

where E_{szs} is defined to denote the z component of the incidence field in plane $z = 0$ resulting from the given radar source, Δ is the ocean surface impedance, and the subscript z indicates the z component of the vector field. Thus, Eq. (1.1) becomes

$$E_{0n}^{+} - \nabla\varepsilon \cdot \nabla(E_{0n}^{+}) \overset{xy}{*} F(\rho)\frac{e^{-jk\rho}}{2\pi\rho} = E_{szs} - \nabla\varepsilon \cdot 2 \lim_{z\to 0^{+}} \frac{\partial}{\partial z}(\vec{E}_s) \overset{xy}{*} F(\rho)\frac{e^{-jk\rho}}{2\pi\rho}. \quad (1.6)$$

To first order E_{0n}^{+} may be approximated by a Neumann series as

$$E_{0n}^{+} \approx E_{szs} + \nabla\varepsilon \cdot [\nabla(E_{szs}) - 2 \lim_{z\to 0^{+}} \frac{\partial}{\partial z}(\vec{E}_s)] \overset{xy}{*} F(\rho)\frac{e^{-jk\rho}}{2\pi\rho}. \quad (1.7)$$

The first term E_{szs} is the solution for a smooth surface, i.e., $\nabla\varepsilon = 0$. The remaining terms represent first-order scattering because of surface roughness. Thus, the first-order electric field normal to the rough surface immediately above the surface for a source field $\vec{E}_s$ is denoted by $(E_{0n}^{+})_1$ as

$$(E_{0n}^{+})_1 = \nabla\varepsilon \cdot [\nabla(E_{szs}) - 2 \lim_{z\to 0^{+}} \frac{\partial}{\partial z}(\vec{E}_s)] \overset{xy}{*} F(\rho)\frac{e^{-jk\rho}}{2\pi\rho}. \quad (1.8)$$

In the following, the primary source is specified to be an elementary dipole. The far-field free-space electric field $\vec{E}_T$, which is observed at $P(R, \theta, \phi)$, due to such a source located at the origin is given by

$$\vec{E}_T = E_\theta\hat{\theta} = jC_0 \sin\theta \frac{e^{-jkr}}{4\pi r}\hat{\theta}, \quad (1.9)$$

where (r, θ, ϕ) are the spherical coordinate variables with

$$r = \sqrt{x^2 + y^2 + z^2} = \sqrt{\rho^2 + z^2}, \quad \hat{\theta} = -\sin\theta\hat{z} + \cos\theta\hat{z}.$$

In addition, $C_0 = \frac{\eta_0 \Delta l}{c}\omega I(\omega)$ is the dipole coefficient for an antenna of length Δl carrying a current I whose radian frequency is ω and wavenumber is k in free space where the intrinsic impedance is η_0.

In order to proceed with the mixed-path propagation, an elevated source will be considered over a plane lossy earth. The original treatment and solution of the problem of determining the radiated fields from this rather simple source over a plane lossy earth was given by Sommerfeld [47]. However, Sommerfeld's solution was written in terms of complex integrals, which are quite difficult to evaluate. The commonly accepted asymptotic solution for the electric field $\vec{E}_T$, which may be found in modern texts addressing the issue of elevated sources above a lossy earth, e.g. [48], may be written in a simplified form for the present purposes as

$$\vec{E}_T = jC_0 \left\{ \sin\theta_1 \frac{e^{-jkR_1}}{4\pi R_1}\hat{\theta}_1 + R_V \sin\theta_2 \frac{e^{-jkR_2}}{4\pi R_2}\hat{\theta}_2 - (1 - R_V)F(\rho, z)\frac{e^{-jkR_2}}{4\pi R_2}[\hat{z} + b\hat{\rho}] \right\}. \tag{1.10}$$

The geometry of the elevated dipole source over a lossy plane earth is shown in Figure 1.4 and various terms of Eq. (1.10) are illustrated. It should be noted that the source dipole has been elevated at $z = h$ and its "image" is located at $z = -h$. R_v is the Fresnel reflection coefficient for a vertically polarized plane wave and $F(\rho, z)$ is the Sommerfeld attenuation function. Both of these parameters are functions of the ground relative permittivity ϵ_r, conductivity σ, and the frequency ω. The constant b depends on the ground parameters.

The first term in Eq. (1.10) is referred to as the direct field, i.e., the source dipole

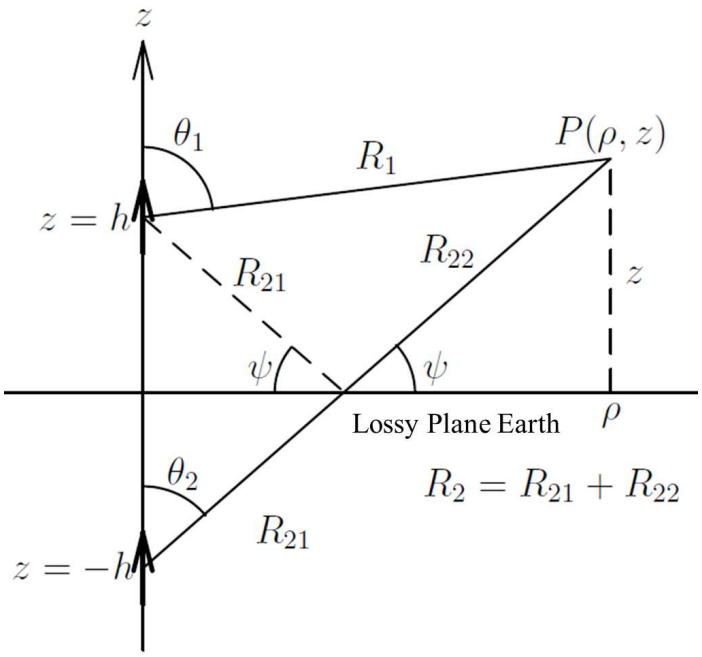

Figure 1.4: Vertical Dipole over Lossy Plane Earth.

radiated electrical field in the absence of earth. The other two terms represent the fields due to earth interactions. Certain special cases are of interest. If the earth is perfectly conducting, $R_v \to 1$ and the field $\vec{E}$ then consists of the first two terms only. Interpreting Eq. (1.10) in relation to Figure 1.4, if the observation point P is on the surface, then $E = 2E_s$ for this case, where E_s is the electrical field from the source dipole. If the earth has finite conductivity and both the source dipole and the observation point $P(\rho, z)$ approach the surface ($h, z \to 0^+$), then $R_v \to -1$ and $\theta_1, \theta_2 \to \pi/2$, and the first two terms in Eq. (1.10) cancel. In general, for good conducting surfaces such as the ocean, the $\hat{\rho}$ component is much smaller than the $\hat{z}$ component of the surface wave. On the other hand, if the observation point P is far removed from the surface, the third term in (1.10) may be neglected and the field $\vec{E}$ can be taken to consist of the first two terms only. The effect of

the earth is then

$$E_{earth} = jC_0 R_v \sin\theta_2 \frac{e^{-jkR_2}}{4\pi R_2}\hat{\theta}_2. \tag{1.11}$$

It should be noted that the reflection coefficient R_v is a function of the observation point P coordinates through its dependence on the reflection angle, i.e., $R_v = R_v(x, y, z, h)$. This implies that R_v can be treated as any other function. For example, it may be Fourier transformed.

In order to apply the above result to the case of the mixed-path propagation, the plane earth is replaced with the ionosphere reflection layer. The geometry of the mixed-path propagation is shown in Figure 1.5. The X-Y plane indicates the ocean surface and the observation point P is at $(x, y, 0^+)$ on the surface. The primary source transmitting antenna is taken to be a vertical dipole at the origin (0, 0, 0^+). Assuming the ionosphere to be a reflecting plane at a height $z = H/2$, the propagation path from the transmitting antenna up to the ionosphere and back to the rough ocean surface could be considered as a straight line from an elevated source at (0, 0, *H*), which is the image of the original source. Note that θ_i is the reflection angle, ρ is the range of the surface wave path, R is the range of the free-space path and $R + \rho$ is the total path of the mixed-path propagation.

The resulting electric field representing the ionospheric effect at $P(x, y, 0^+)$ is given as

$$\vec{E}_i = jR_i C_0 \sin\theta_i \frac{e^{-jkR}}{4\pi R}\hat{\theta}, \tag{1.12}$$

where R_i is the effective ionospheric reflection coefficient (IRC), which represents the ionospheric effect on the propagation of the radio waves.

In order to determine the first-order scattered surface field $(E^+_{on})_1$, $\vec{E}_i$ given by Eq. (1.12) will be substituted for $\vec{E}_s$ in Eq. (1.8). Moreover, the terms $2\lim_{z\to 0^+} \partial\vec{E}_i/\partial z$ and

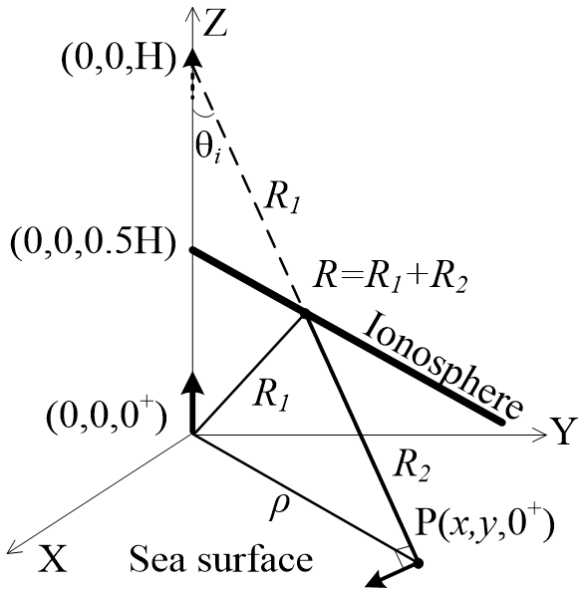

Figure 1.5: Scattering geometry for ionosphere-ocean return.

$\nabla_{xy}(E_{izs})$ in Eq. (1.12) are evaluated as

$$2\lim_{z\to 0^+}\frac{\partial \vec{E}_i}{\partial z} \sim kC_0R_i\sin\theta_i\cos^2\theta_i\frac{e^{-jkR}}{2\pi R}\hat{\rho},$$
$$\nabla_{xy}(E_{izs}) \sim -kC_0R_i\sin^3\theta_i\frac{e^{-jkR}}{2\pi R}\hat{\rho}.$$

Then the first-order electric field is given as

$$(E_{0n}^+)_1 \sim -kC_0[(\nabla\varepsilon\cdot\hat{\rho})R_i\sin\theta_i\frac{e^{-jkR}}{2\pi R}] \overset{xy}{*} F(\rho)\frac{e^{-jk\rho}}{2\pi\rho}. \tag{1.13}$$

Referring to Figure 1.5, Eq. (1.13) may be written in integral form as

$$\begin{aligned}(E_{0n}^+)_1(x,y) \sim -\frac{kC_0}{(2\pi)^2}\int\int_S(\nabla\varepsilon\cdot\hat{\rho})(x_1,y_1)R_i(x_1,y_1)\sin[\theta_i(x_1,y_1)]F(\rho_2)\\ \cdot\frac{e^{-jk(R_1+\rho_2)}}{R_1\rho_2}dx_1dy_1,\end{aligned} \tag{1.14}$$

where $R_1=\sqrt{\rho_1^2+h^2}$, $\rho_1=\sqrt{x_1^2+y_1^2}$, $\rho_2=\sqrt{(x-x_1)^2+(y-y_1)^2}$.

In the monostatic case, for which the transmitting and receiving antennas are co-located and the observation point (x,y) is at the origin (0,0), it can be inferred from Figure 1.5

that $\rho = 0$ and $\rho_2 = \rho_1$. Upon transformation from Cartesian to polar coordinates (ρ_1, θ_1), (1.14) then simplifies to

$$(E_{0n}^{+})_{1mo} \sim -\frac{kC_0}{(2\pi)^2} \int_{\rho_1} \int_{\theta_1} (\nabla\varepsilon \cdot \hat{\rho}_1)(\rho_1, \theta_1) R_i(\rho_1, \theta_1) \sin[\theta_i(\rho_1)] F(\rho_1) \cdot \frac{e^{-jk(R_1+\rho_1)}}{R_1} d\theta_1 d\rho_1, \tag{1.15}$$

where the subscript "mo" denotes the monostatic case. The limits of integration will be determined from the region of the scattering surface. The quantities associated with the ocean and ionosphere surfaces are represented using subscripts 'o' and 'i', respectively.

Here, the rough surface profile ε will be eventually assumed to be that of the ocean surface. As in [37–39], the sea surface, which is assumed to be a stochastic process, may be represented by a general Fourier form as

$$\varepsilon(x, y) = \sum_{\vec{K}_o} P_{\vec{K}_o}^{o} e^{j\vec{K}_o \cdot \vec{\rho}}, \tag{1.16}$$

where $P_{\vec{K}_o}^{o}$ is the Fourier coefficient for a surface component whose wave vector is $\vec{K}_o$, which is taken to be a continuous parameter. Of course, in reality, the sea surface is time-varying and will introduce an additional parameter t in (1.16). However, in the interest of simplicity and because any surface time variation will be on a considerably longer time scale than electromagnetic propagation times, this temporal variation is not immediately introduced.

The ionospheric reflection coefficient R_i depends on both position and frequency, i.e., $R_i = R_i(x, y, \omega)$ [40]. For simplicity, the zero-order reflection coefficient at the radar operating frequency ω_0 will be considered. A continuous parameter stochastic model will also be assumed for this zero-order ionosphere reflection coefficient $R_i(x, y, \omega_0)$. This seems reasonable since R_i certainly depends on the parameters of the ionosphere, e.g., ionospheric

electron densities. These will have certain average values depending on geophysical conditions, but there will be point-to-point variations which may well be viewed as random. It is then to be expected that R_i will have random variations with respect to the surface observation point (x, y), in particular, relating to phase. Furthermore, the electron densities and, therefore, R_i may very well have a low-frequency time variation profile. This can be incorporated in the same fashion as the temporal variation in ε, but, again, the time scales will be very much longer than electromagnetic propagation time scales and so may be included later. Of course, both the ocean surface and ionospheric reflection coefficient time variations will impact the observed Doppler frequencies of the received electromagnetic signal. With these considerations in place, the ionospheric reflection coefficient $R_i(x, y)$ for the ionosphere may be written in Fourier form, analogous to (1.16) for the ocean, as

$$R_i(x, y) = \sum_{\vec{K}_i} P^i_{\vec{K}_i} e^{j\vec{K}_i \cdot \vec{\rho}}, \tag{1.17}$$

where $P^i_{\vec{K}_i}$ is the Fourier coefficient of the ionosphere reflection coefficient for a component whose spectral wavenumber is K_i.

The integral with respect to θ_1 in (1.15) is evaluated asymptotically by the well-known stationary phase technique [49]. The stationary points for θ_1 for the technique is shown to be the same direction as that of the vector sum $\vec{K}_s = \vec{K}_i + \vec{K}_o$ [45]. The direction of this sum ϕ_s corresponds to the radar look direction for monostatic case.

The ρ_1-integral in (1.15) is solved approximately by incorporating a pulsed radar source. The frequency-domain antenna current I in the electric field equation (1.15) is specified as a gated sinusoidal signal with pulse width τ_0 and frequency ω_0. The time-domain version

of this current may be written as

$$i(t) = I_0 e^{j\omega_0 t} \left[h(t) - h(t - \tau_0) \right], \tag{1.18}$$

where I_0 is the current amplitude and $h(t)$ is the Heaviside function. For a given time t, the radial extent ρ_1 of the surface from which scatter contributes to the received signal at time t is limited by the Heaviside function. In order to incorporate this time-domain current, Eq. (1.15) is inverse Fourier transformed with respect to the frequency ω. After a series of derivations (see [41]), the expression of the received electric field in Eq. (1.15) becomes

$$\begin{aligned}(E_{0n}^{+})_{1mo}(\rho_s) \sim & - j \frac{k_0^2 \eta_0 \Delta l I_0}{(2\pi)^{3/2}} e^{-j\pi/4} e^{j2k_0(\rho_s + \frac{\Delta\rho_s}{2})} e^{-jk_0(\rho_0 + R_0)} \frac{F(\rho_0)}{R_0\sqrt{\rho_0}} \sin\theta_0 \\ & \cdot \sum_{\vec{K}_o} \sum_{\vec{K}_i} P^o_{\vec{K}_o} P^i_{\vec{K}_i} \frac{\vec{K}_o \cdot \vec{K}_s}{K_s^{3/2}} e^{jK_s\rho_0} \Delta\rho Sa[\frac{\Delta\rho}{2}\{K_s - k_0(1 + \sin\theta_0)\}],\end{aligned} \tag{1.19}$$

where $\rho_s = \frac{ct}{2} - \frac{c\tau_0}{4}$ is defined as the apparent surface range, $\Delta\rho_s = \frac{c\tau_0}{2}$ is the apparent range resolution, $Sa(\cdots)$ is the sampling function with the usual form of $\sin(\cdots)/(\cdots)$, ρ_0 represents the range between the radar and the center point of the scattering patch on the ocean surface, R_0 is the range of the skywave from the radar to the center point of this scattering patch, and $\Delta\rho$ is the range resolution of the patch.

Equation (1.19) is an estimate of the electric field intensity at the receiving antenna for a single transmitted pulse of a time pulsed radar. In the case of a Doppler radar, a time series of such pulses is transmitted and the return is recorded. This record is then analyzed to extract useful information regarding the time variation in the targets being interrogated. Here, in order to incorporate the required temporal variability of the sea surface profile ε and the ionosphere reflection coefficient R_i, (1.16) and (1.17) need to be modified by

including the time variable t as

$$\varepsilon(x_1, y_1, t) = \sum_{\vec{K}_o, \omega_o} P^o_{\vec{K}_o, \omega_o} e^{j(\vec{K}_o \cdot \vec{\rho} + \omega_o t)},$$

$$R_i(x_1, y_1, t) = \sum_{\vec{K}_i, \omega_i} P^i_{\vec{K}_i, \omega_i} e^{j(\vec{K}_i \cdot \vec{\rho} + \omega_i t)}.$$

The frequencies ω_o of the ocean waves and ω_i of the ionospheric irregularities are assumed to be small, so that time variations during the collection time for a single pulse may be considered to be negligible. Thus, only pulse to pulse variations are considered.

The received power spectral density (PSD) is taken to be the Fourier transform of the autocorrelation function of the time-varying received electric field and is derived as [41]

$$\begin{aligned} P_{i1}(\omega_d) =& \frac{A_r}{2\eta_0} \frac{(k_0^2 \eta_0 \Delta l |I_0|)^2}{(2\pi)^2} \frac{|F(\rho_0)|^2}{R_0^2 \rho_0} \sin^2\theta_0 (\Delta\rho)^2 \int_{\vec{K_o}} \int_{\vec{K_i}} \int_{\vec{\omega}_o} \int_{\vec{\omega}_i} \\ & \cdot \left(\frac{\vec{K}_o \cdot \vec{K}_s}{K_s^{3/2}} \right)^2 S_o(\vec{K}_o, \omega_o) S_i(\vec{K}_i, \omega_i) \delta[\omega_d - (\omega_o + \omega_i)] \\ & \cdot Sa^2 \left[\frac{\Delta\rho}{2} \{K_s - k_0(1 + \sin\theta_0)\} \right] d\vec{K}_o d\vec{K}_i d\omega_o d\omega_i. \end{aligned} \tag{1.20}$$

where A_r is the receiving antenna effective area, ω_d is the observed "Doppler" frequency, and the ensemble average of the random Fourier coefficients may be written as

$$\langle P^o_{\vec{K}_o, \omega_o} P^i_{\vec{K}_i, \omega_i} (P^o_{\vec{K}_o, \omega_o})^* (P^i_{\vec{K}_i, \omega_i})^* \rangle = \quad S_o(\vec{K}_o, \omega_o) S_i(\vec{K}_i, \omega_i) d\vec{K}_o d\vec{K}_i d\omega_o d\omega_i,$$

and where $*$ represents complex conjugation, and $S_o(\vec{K}_o, \omega_o)$ and $S_i(\vec{K}_i, \omega_i)$ are the spectral densities of the ocean surface and the ionosphere, respectively. This PSD equation contains an integration over all spatial wavenumbers and temporal frequencies for both the ocean wave spectrum and the spectral representation of the ionospheric reflection coefficient.

In the case of the ocean surface, the linear dispersion relation between the frequency ω_o

and wavenumber K_o of individual gravity wave components is written as

$$\omega_o = \sqrt{gK_o \tanh K_o d}, \tag{1.21}$$

where g is the usual acceleration due to gravity, and d is the water depth. Recalling that the phase speed of the wave is $\frac{\omega_o}{K_o}$, Eq. (1.21) indicates that waves with longer wavelengths ($\lambda_o = 2\pi/K_o$) will travel at higher speeds. When the water is sufficiently deep, (typically, in oceanographical measurements, when $d \geq \lambda_o/4$ [50]) so that $\tanh(Kd) \approx 1$, a "deep water" approximation to the dispersion relationship may be given as

$$\omega_o = \sqrt{gK_o}. \tag{1.22}$$

The deep water approximation is often valid for HF radar operation and this equation will be employed throughout the remainder of this work. Then, the spectral density incorporating the "linear" dispersion relation for first-order gravity waves is typically cast as

$$S_o(\vec{K}_o, \omega_o) = \frac{1}{2} \sum_{m=\pm 1} S_o(m\vec{K}_o)\delta(\omega_o + m\sqrt{gK_o}), \tag{1.23}$$

where $m = \pm 1$ corresponds to wind driven ocean waves moving parallel or anti-parallel to the radar look direction. Typically, the directional ocean spectrum $S_o(\vec{K}_o)$ may be expressed as the product of a non-directional spectrum, $S_o(K_o)$ and a normalized directional factor, $D(\theta_{\vec{K}_o})$ as

$$S_o(\vec{K}_o) = S_o(K_o)D(\theta_{\vec{K}_o}), \tag{1.24}$$

where $D(\theta_{\vec{K}_o})$ is normalized [51] as

$$\int_0^{2\pi} D(\theta_{\vec{K}_o}) d\theta_{\vec{K}_o} = 1.$$

The Pierson-Moskowitz (PM) non-directional spectrum [52] is selected to represent the ocean wave spectrum for a fully developed sea as

$$S_o(K_o) = \frac{0.0081}{2K_o^4} e^{-0.74(\frac{g}{K_o U^2})^2}, \tag{1.25}$$

where U is the speed of the surface wind measured at 19.5 m above the ocean surface. $D(\theta_{\vec{K}_o})$ is chosen to be a cardioid directional distribution for the directional ocean wave height spectrum of a wind driven sea [53] as

$$D(\theta_{\vec{K}_o}) = \frac{4}{3\pi} \cos^4 \left(\frac{\theta_{\vec{K}_o} - \theta_{\vec{U}}}{2} \right), \tag{1.26}$$

where $\theta_{\vec{U}}$ is the dominant direction of the surface wind. Thus, the spectral density of ocean surface waves becomes

$$S_o(m\vec{K}_o) = \frac{0.0081}{2K_o^4} e^{-0.74(\frac{g}{K_o U^2})^2} \cdot \left[\frac{4}{3\pi} \cos^4 \left(\frac{\theta_{\vec{K}_o} + \frac{(1-m)\pi}{2} - \theta_{\vec{U}}}{2} \right) \right], \tag{1.27}$$

In the case of the ionosphere, it is assumed in [41] that the ionosphere reflecting layer has only a constant horizontal velocity. Thus the spectrum $S_i(\vec{K}_i)$ is non-directional. Then, the spectral density for the ionospheric reflection coefficient $S_i(K)$ has been assumed to be generally representable by a uniform or exponential distribution model in [41], but these models may not adequately describe the behaviour of the ionosphere. Thus, the spectrum of the ionospheric reflection coefficient needs to be further investigated.

1.3 The Scope of the Thesis

In this thesis, theoretical models of the ionospheric clutter are established based on the foundations of the mixed-path propagation theory developed by Walsh [40]. The thesis is organized as follows:

In Chapter 2, the physical influences of the ionospheric electron density on HF radar Doppler spectra are taken into account in the ionospheric reflection coefficient (IRC) model. The relationship between the IRC and the electron density irregularities within the ionosphere layers is derived based on an layered ionospheric model [11].

In Chapter 3, by considering the reflection from the ionosphere and second-order scattering on the ocean surface, the received electric field involving mixed-path propagation for a monostatic radar configuration is derived from Walsh's mixed-path propagation theory. In this case, the reflected signals from the ionosphere may be scattered back to the receiver by one second-order ocean wave (hydrodynamic effect) or two first-order ocean waves (electromagnetic effect) [54]. Then, the field integrals are taken to the time domain, with the source field being that of a vertically polarized pulsed dipole antenna. Subsequently, the second-order received power spectral density model is developed by assuming the ocean surface and the ionosphere are stochastic processes.

In Chapter 4, the derived ionospheric clutter model for a pulsed radar source is further investigated for the case of vertical propagation for a monostatic configuration and for mixed-path propagation when using a bistatic configuration.

In Chapter 5, a theoretical model of the mixed-path propagation is developed by involving a frequency-modulated continuous wave (FMCW) radar source.

In order to investigate the power density spectrum of this ionospheric clutter and its relative power density to that of the average first-order ocean clutter peak, the normalized ionospheric clutter power density is simulated. Numerical simulation results are provided to demonstrate the performance of the ionospheric clutter under a variety of ionospheric conditions and sea states.

Chapter 6 summarizes the fundamental conclusions reached from the work presented in the previous four chapters of this thesis. Based on the questions generated by the present analysis, several suggestions for future research are also provided.

The research described in this thesis has been published in five refereed scholarly journal papers as listed below.

1. J. Walsh, E. W. Gill, W. Huang, and S. Chen, "On the Development of a High Frequency Radar Cross Section for Mixed Path Ionosphere-ocean Propagation", *IEEE Trans. Antennas Propag.*, vol. 63, no. 6, pp. 2655-2664, 2015.

   This paper provides an overview of Walsh's mixed-path propagation method (Section 1.2.3) and numerical simulations (Section 2.4).

2. S. Chen, E. W. Gill, and W. Huang, "A High Frequency Surface Wave Radar Ionospheric Clutter Model for Mixed-Path Propagation with Second-Order Sea Scattering," *IEEE Trans. Antennas Propag.*, 2016. (in press, DOI: 10.1109/TAP.2016.2618538)

   This paper provides the analysis of the mixed-path propagation with second-order sea scattering (Chapter 3).

3. S. Chen, W. Huang, and E. W. Gill, "A Vertical Reflection Ionospheric Clutter Model for HF Radar Used in Coastal Remote Sensing," *IEEE Antennas Wireless Propag. Lett.*, vol. 14, pp. 1689-1693, 2015.

   This paper provides the analysis of the vertical ionospheric clutter (Section 4.2).

4. S. Chen, W. Huang, and E. W. Gill, "First-Order Bistatic High Frequency Radar Power for Mixed-path Ionosphere-Ocean Propagation," *IEEE Geosci. Remote Sens.*

Lett., 2016. (in press, DOI: 10.1109/LGRS.2016.2618855)

This paper provides the analysis of the mixed-path propagation for bistatic radar configuration (Section 4.3).

5. S. Chen, E. W. Gill, and W. Huang, "A First-Order HF Radar Cross Section Model for Mixed-Path Ionosphere-Ocean Propagation with an FMCW Source," *IEEE J. Oceanic Eng.*, vol. 41, no. 4, pp. 982-992, 2016.

   This paper provides the analysis of the mixed-path propagation with FMCW radar source (Chapter 5).

Chapter 2

A Model for the Ionospheric Reflection Coefficient

2.1 Introduction

The ionospheric reflection coefficient (IRC) is used to describe the ionospheric effects on the propagation of a radio wave, which is the electric field strength ratio of the reflected wave to that of the incident wave. It is fundamentally related to ionospheric electron density irregularities [55]. For each ionospheric layer, there is a quiescent ionospheric electron density with random spatial irregularities. These irregularities may lead to the shifting and spreading of the clutter signal in the range and Doppler domains [56]. Radar signals backscattered from these irregularities can be very intense and may be considered to vary randomly with surface observation positions. Efforts to mitigate the influence of these signals require knowledge of the probability distribution for the IRC, which is a function of

the electron density irregularities, and investigation of the Doppler shift and spread that the ionospheric clutter introduces in the radar echoes. The spectral density for the IRC $S_i(\vec{K}_i, \omega_i)$ has been previously assumed to be representable by a uniform or exponential distribution model [40,41], but these may not adequately describe the behaviour of the ionosphere properly [57]. The spectral density of the IRC is basically related to the irregularities of the electron density. Thus, this parameter should be determined based on the practical ionospheric irregularity model rather than by assuming a simple uniform or exponential distribution. In order to make the ionospheric clutter model more physically meaningful, this spectral density should be determined from the properties of the ionosphere itself.

In this Chapter, the propagation of the HF radio waves within the ionosphere is investigated. Then, the IRC expression is modified from that used by Walsh [41] to be related to the ionospheric electron density irregularities. Finally, a typical $in\text{-}situ$ distribution for the electron density is incorporated into the derived spectral density function of the IRC.

2.2 The Propagation of Radio Waves within Ionosphere

The ionosphere contains high densities of free electrons and ions. Thus, it can affect the properties of electromagnetic waves that are propagated within or through it. The spatial-temporal phase spectrum of signals reflected from the bottom of the ionosphere in the presence of ionospheric irregularities is investigated through a geometric optics approach. A dispersion relation for the HFSWR pulse as it propagates in the ionosphere is given in [58] as

$$n^2 = \frac{c^2 k^2}{\omega^2} = 1 - \frac{\omega_p^2}{\omega^2}, \tag{2.1}$$

where n is the refractive index, c is the speed of light, ω is the radar frequency, k is its wave number, and ω_p is the electron plasma frequency, defined as

$$\omega_p^2 = \frac{e^2 N_e}{\epsilon_0 m}, \tag{2.2}$$

where e is the charge of an electron, ϵ_0 is the permittivity of free space, m is the mass of an electron, and N_e is the electron density.

The ionosphere will be considered to be a layer-stratified plasma of sub-layers as illustrated in Figure 2.1. The electron density of each sub-layer increases with altitude and the refractive index decreases. When the radio waves propagate in the ionosphere, their direction and velocity are changed according to the Snell's law. The trajectories of the radio waves are refracted away from the normal for upward propagation from slice to slice as shown in Figure 2.1. When the angle of refraction is $90°$, the ray will start to be completely

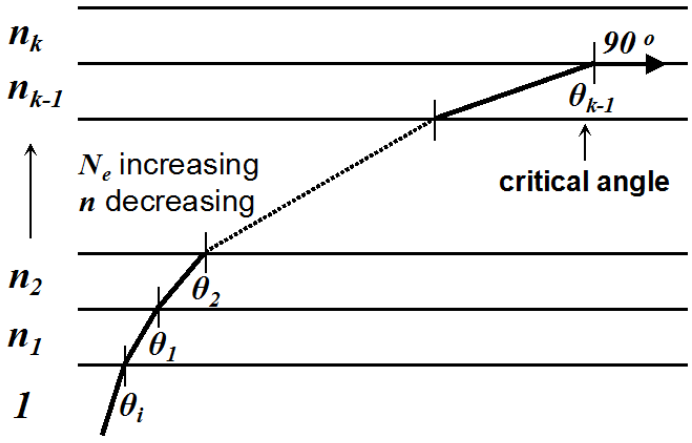

Figure 2.1: Refraction of a radio wave in the ionosphere.

internally reflected back to the earth by the boundary, the angle of incidence then being the

critical angle. Applying Snell's law to the geometry in Figure 2.1 gives

$$\frac{\sin\theta_i}{\sin 90^\circ} = \frac{n_k}{1}. \tag{2.3}$$

Eq. (2.3) indicates that the ray will be reflected back to the earth at the stratum whose refractive index numerically equals the sine of the incidence angle at the point of entrance to the ionosphere, i.e. $n_k = \sin\theta_i$. Now the electron density N_e is assumed to be continuously changing and linearly related to the altitude z, and independent of the horizontal coordinate. As shown in Figure 1.2 (d), the measured electron density profile is a parabola-shape curve for the F-layer from 290 to 500 km. However, from the same figure it may be observed that for radio wave frequencies under approximately 5 MHz, it makes sense to simplify the relationship between the electron density and the height as being linear from the bottom of the F-layer to approximately 350 km. For higher radio wave frequencies, it would be better to apply more realistic electron density profiles, such as a parabola-linear composite model or the international reference ionosphere [10]. Then the refractive index may be written in the form [36]

$$n^2(\omega, z) = 1 - \cos^2\theta_i \frac{z}{z_0}, \tag{2.4}$$

where, for our purposes, $z = 0$ is at the bottom of the F-region ionosphere, which is approximately 200 km above the ground, and $z = z_0$, the height where total reflection occurs, is determined by the radio frequency. The total reflection effects may be accounted for by an integral over a volume of refractive index fluctuations [59].

2.3 Derivation for the Spectral Density of the IRC

2.3.1 Representation of the IRC

For the case of the ionospheric clutter, the electric field of an HFSWR signal reflected by the ionosphere to the ocean surface is considered. The free space radiated far electric field at a point $P(r, \theta, \phi)$ from an elementary dipole source located at the origin is given in Eq. (1.9). In Cartesian coordinates, the total phase accrued by the signal from the radar to the point $P(x, y, z)$ (i.e. $P(r, \theta, \phi)$) may be written as

$$-kr = -k(\rho_1 \sin\theta + z\cos\theta), \tag{2.5}$$

where $\rho_1 = x\cos\phi + y\sin\phi$ is the projection of R_1 onto the X-Y plane (see Figure 1.5). When the radio wave passes through the m_{th} layer of the ionosphere with a thickness z_m, the change in its phase is given by

$$-k_m(\rho_{1m}\sin\theta_m + z_m\cos\theta_m) = -k(\rho_m\sin\theta_i + n_m z_m\cos\theta_m), \tag{2.6}$$

where, within the m_{th} layer, k_m is the radio wavenumber, ρ_{1m} is the path change in the X-Y plane, θ_m is the transmission angle, and n_m is the refractive index of the layer.

The paths of the radio wave travelling up to the ionosphere and being reflected to the ground are assumed to be symmetric (see Figure 1.5). Then the total phase change from the radar to the ocean surface point in Figure 1.5 is

$$\begin{aligned}\phi_i =& -k(\rho\sin\theta_i + 2\int_0^{z_0} n(\omega, z)\cos\theta_m dz) \\ =& -k(\rho\sin\theta_i + 2\int_0^{z_0}\sqrt{n(\omega,z)^2 - \sin^2\theta_i}dz),\end{aligned} \tag{2.7}$$

where z_0 is the height of the reflection point. The integral in (2.7) expresses that a change of phase is cumulative for a wave passing through a slowly varying medium. Thus, the electric field at the surface point is

$$E_i = jC_0 \sin\theta_i \frac{e^{-jk(\sin\theta_i \rho + 2\int_0^{z_0} \sqrt{n(\omega,z)^2 - \sin^2\theta_i} dz)}}{4\pi R} \hat{\theta}. \tag{2.8}$$

Comparing Eq. (2.8) with Eq. (1.12), the reflection coefficient is given as [60]

$$R_i(\omega, \vec{\rho}) = e^{jk(H\cos\theta_i - 2\int_0^{z_0} \sqrt{n(\omega,z)^2 - \sin^2\theta_i} dz)}. \tag{2.9}$$

This indicates that the IRC is the electric field ratio of the reflected wave to the incident wave and depends on both position and radio frequency. Here, the radar transmitted signal is considered to have a dominant frequency ω_0.

Furthermore, the radio waves may suffer from ionospheric absorption while propagating within the ionosphere. During this process, part of the radio wave energy may be transformed into heat and electromagnetic noise by electron collisions with neutral molecules and ionized particles. The amplitude of the electric field decays exponentially with the absorption loss, and this is accounted for by

$$R_{ia} = e^{\int -\kappa_a dz}, \tag{2.10}$$

where κ_a is the attenuation per unit distance. In the absence of the Earth's magnetic field, κ_a in decibels per kilometer is given in [10] as

$$\kappa_a = 4.6 \times 10^{-2} \frac{N_e \nu}{\mu(\omega^2 + \nu^2)}, \tag{2.11}$$

where ν is the collision frequency and μ is the magnetic permeability. The absorption of HF waves occurring in the D layer where μ is approximately unity is usually denoted

as nondeviative absorption, while deviative absorption occurs where marked ray bending takes place, i.e., the absorption during reflections from the E and F layers. The absorption may be measured by ionospheric sounding techniques [10].

After taking this factor into account as the real part of the IRC, R_i may be rewritten in the form

$$R_i(\vec{\rho}) = R_{ia} e^{j\Phi(\vec{\rho})}. \tag{2.12}$$

Here we define the phase error function Φ as

$$\Phi(\vec{\rho}) = k_0 H \cos\theta_i - 2k_0 \int_0^{z_0} \sqrt{n(z)^2 - \sin^2\theta_i} dz.$$

This parameter represents deviations of the total phase due to the existence of the ionosphere. It is fundamentally changed with the regular and stochastic variations of the electron density. The regular variations are associated with seasonal and diurnal dependencies and are considered as the average electron density background depending on geophysical conditions [61]. The stochastic fluctuations are significantly more varied and arise due to the simultaneous effects of a number of random factors: atmospheric gas turbulence, sporadic sun activity, various kinds of plasma instability, etc [62]. A combination of these stochastic sources generates a wide spatial spectrum of ionospheric irregularities.

2.3.2 Relationship between the IRC and ionospheric irregularities

When the influence of collisions and the Earth's magnetic field can be neglected, Φ may be taken as a zero mean real random variable. In order to investigate the statistic of properties of the IRC, the spatial autocorrelation function corresponding to Eq. (2.12) is calculated as

$$\mathcal{R}_{R_i}(\vec{r}) = \langle R_i(\vec{\rho}+\vec{r}) R_i^*(\vec{\rho}) \rangle = \langle e^{j[\Phi(\vec{\rho}+\vec{r}) - \Phi(\vec{\rho})]} \rangle. \tag{2.13}$$

The relationship of this function to the phase error function $\mathcal{R}_\Phi(\vec{r})$ is given in [40] as

$$\mathcal{R}_{R_i}(\vec{r}) = e^{[\mathcal{R}_\Phi(\vec{r}) - \langle\Phi^2\rangle]}, \tag{2.14}$$

where $\langle\Phi^2\rangle$ is the mean square of the phase error function $\mathcal{R}_\Phi(0)$. Thus, the perturbation of the phase error function accounts for the variation of the IRC. Here we consider only the first order perturbation, i.e. $\mathcal{R}_{\Phi_1}(\vec{r}) \approx \mathcal{R}_\Phi(\vec{r}) - \langle\Phi^2\rangle$.

Then, the autocorrelation of the IRC may be expanded in an infinite series as

$$\mathcal{R}_{R_i}(\vec{r}) = (1 + \mathcal{R}_{\Phi_1}(\vec{r}) + \frac{1}{2!}\mathcal{R}^2_{\Phi_1}(\vec{r}) + \cdots). \tag{2.15}$$

Taking the spatial Fourier transform of Eq. (2.15) gives the spectral density of the IRC as

$$S_i(\vec{K_i}) = \frac{\delta(K_i)}{2\pi K_i} + S_{\Phi_1}(\vec{K_i}) + \frac{1}{2!}S_{\Phi_1}(\vec{K_i}) * S_{\Phi_1}(\vec{K_i}) + \cdots, \tag{2.16}$$

where $*$ denotes two dimensional wave-number convolution. This equation is useful in providing a connection between the spectral density function of the IRC and the phase error function Φ which is physically meaningful.

In order to determine S_i, the derivation of S_Φ is considered firstly. The phase variation may be caused by small-scale ionospheric irregularities or large-scale travelling ionospheric disturbances (TIDs). Small-scale irregularities (from hundreds of metres to kilometres in size) of the ionospheric plasma may increase the optical thickness for radio wave scattering, and a single radar signal will be observed to undergo interactions with multiple irregularities. This multiple scattering results in a corresponding redistribution of the spatial and temporal properties of the radio waves [63]. The ionospheric electron density with small-scale irregularities is described by

$$N_e = N_{e0}(z) + N_{e1}(\vec{r}), \tag{2.17}$$

where $N_{e0}(z)$ is the zero-order ionospheric electron density profile, $N_{e1}(\vec{r})$ is the first-order irregularity, and $\vec{r} = (x, y, z)$ is the three dimensional coordinate of the ray trajectory. By Fermat's principle, the ray follows a trajectory of minimum phase, which means that perturbations to the ray trajectory are second-order in density perturbation [64]. Thus, a first-order Taylor series perturbation to Φ would be evaluated along the zero-order ray trajectory and be given by

$$\Phi_1 = 2k_0 \int_0^{z_0'} N_{e1}(\vec{r}, t) \cdot \frac{\partial \sqrt{n(z)^2 - \sin^2 \theta_i}}{\partial N_e} dz. \tag{2.18}$$

In practical terms, the radar wavelength goes to infinity at the turning point and the concept of phase is no longer meaningful. A more rigorous full-wave analysis of fluctuations near the turning point shows the phase contribution near the turning point to be minor [65]. Using that conclusion, we ignore the phase contribution near the turning point by cropping the path integration a short distance (on the order of a wavelength) below the turning point at a height of z_0'. Here the first-order phase error function is equivalent to the wavenumber of the IRC. From Eq. (2.1) and Eq. (2.2), Eq. (2.18) may be rewritten in the form

$$\Phi_1 = 2k_0 \int_0^{z_0'} N_{e1}(\vec{r}) \cdot \frac{\partial \sqrt{\cos^2 \theta_i - \frac{e^2 N_e}{\epsilon_0 m \omega_0^2}}}{\partial N_e} dz = -\frac{2 r_e \lambda_0}{\cos \theta_i} \int_0^{z_0'} \frac{N_{e1}(\vec{r})}{\sqrt{1 - \frac{z}{z_0}}} dz, \tag{2.19}$$

where $r_e = e^2/(4\pi\epsilon_0 m c^2)$ is the classical electron radius and $\lambda_0 = 2\pi/k_0$.

For HFSWR applications, we are interested in the autocorrelation of the phase error function as a function of the horizontal plane position, and this may be written as

$$\begin{aligned} \mathcal{R}_{\Phi_1}(x', y') &= \langle \Phi_1(x + x', y + y') \Phi_1^*(x, y) \rangle \\ &\approx \frac{4 z_0 r_e^2 \lambda_0^2}{\cos^2 \theta_i} \log \frac{z_0}{z_0 - z_0'} \int_{-\infty}^{\infty} \mathcal{R}_{N_{e1}}(x', y', z') dz', \end{aligned} \tag{2.20}$$

where $\mathcal{R}_{N_{e1}}$ refers to the autocorrelation of the electron density fluctuations. Then, the spectral density of the first-order phase error function may be calculated by Fourier transformation of both sides. Finally, the relationship between the spectral density of Φ_1 (i.e. S_{Φ_1}) and the electron density may be obtained as

$$\begin{aligned} S_{\Phi_1}(\kappa_x, \kappa_y) &= \int\int \mathcal{R}_{\Phi_1}(x', y', \tau) e^{-j\kappa_x x' - j\kappa_y y'} dx' dy' \\ &= \frac{4 z_0 r_e^2 \lambda_0^2}{\cos^2 \theta_i} \log \frac{z_0}{z_0 - z_0'} S_{N_{e1}}(\kappa_x, \kappa_y, \kappa_z)|_{\kappa_z = 0}, \end{aligned} \tag{2.21}$$

where κ is the wavenumber of the electron density irregularities, and κ_x, κ_y and κ_z are its Cartesian coordinate components. Research on ionosphere modelling suggests that the spectral density $S_{N_{e1}}$ of the electron density irregularities follows a power law model, which means the $S_{N_{e1}}$ changes with the power of κ. $In\text{-}situ$ measurements show the power is around 4 [66].

A generally used spectral density of the electron density irregularities which are infinitely elongated along the magnetic field is in the form [57]

$$S_{N_{e1}}(\vec{\kappa}) = \frac{8\pi^3 \kappa_0 \langle N_{e1}^2 \rangle \delta(\kappa_\parallel)}{(\kappa_0^2 + \kappa_\perp^2)^{3/2}}, \tag{2.22}$$

where $\kappa_0 \approx 10^{-4}\text{m}^{-1}$ is the "outer" scale size parameter, which corresponds to the largest scale size for which the eddies may be considered to be isotropic, $\kappa_\perp$ is the magnitude of the component of κ that is perpendicular to the Earth's magnetic field, $\kappa_\parallel$ is the magnitude of the component of κ along the field, and $\langle N_{e1}^2 \rangle$ is the variance of the electron density fluctuations at the reflection height.

For present purposes, it is reasonable to assume that the irregularities move without changing their shapes and may be adequately described by a frozen irregularity structure that convects with the background ionosphere, which is known as the Taylor hypothesis

[62]. Thus, the temporal variations of the ionospheric irregularities are considered to be entirely due to the plasma drifting of the ionospheric layers, which give,

$$S_i(\vec{K}_i, \omega_i) = S_i(\vec{K}_i)\delta(\omega_i + \vec{K}_i \cdot \vec{v}_h + 2k_0 v_v \cos\theta_i), \tag{2.23}$$

where v_h is the horizontal ionospheric plasma drift velocity, and v_v is the vertical ionospheric plasma drift velocity.

The ionospheric plasma is often structured into large-scale wavelike fluctuations of electron density, i.e., TIDs. These may introduce variations of the reflection surface height and the plasma drift velocity. TIDs can be tens to thousands of kilometres across, travel at speeds of hundreds of meter per second, and have typical wave periods from tens of minutes to more than an hour. Many observations show that the occurrence of TIDs is commonly associated with the action of an average regular structure of the atmosphere, the acoustic gravity waves (AGWs) [67]. TIDs may cause distortion of the ionospheric reflection surface during extended temporal measurement periods and induce apparent variations of the angles of arrival and Doppler frequency shift on the ionospheric wave propagation. The TIDs information may be obtained from the time-frequency distributions (TFD) of the ionospheric echoes [68].

For simplicity, the horizontal wavelike TID may be considered as a large-scale plane wave with wave vector k_T and frequency ω_T corresponding to those of the original AGW. Variations in electron densities caused by TIDs may change the reflection height of the radio waves from the ionosphere. This height may be represented as

$$H(\vec{\rho}, t) = H_0[1 + h(\vec{\rho}, t)] = H_0[1 + \delta_h \cos(\vec{k}_T \cdot \vec{\rho} - \omega_T t)], \tag{2.24}$$

where H_0 is the mean height, δ_h is the relative surface height variation, and $\vec{\rho} = (x, y)$ is a

two dimensional coordinate on the ray trajectory. The time-dependent height in Eq. (2.24) will result in additional Doppler shifts in radar spectrum, which are independent of the shifts induced by the plasma drift. Since the periods of TIDs are much longer than the collection time for one range-Doppler spectrum, only the vertical velocity of the reflection surface is taken into account. The effects of the TID phase φ is examined by the time-frequency distributions. Thus, the vertical velocity in Eq. (2.22) is expressed as

$$v_v = \frac{dH}{dt} = H_0 \omega_T \delta_h \sin \varphi. \tag{2.25}$$

Now, the spectral density for the IRC may be determined by Eq. (2.16), Eq. (2.21), Eq. (2.22) and Eq. (2.25). This spectral density may be affected by the spectral density of the small-scale electron density irregularities and the Doppler shift introduced by the large-scale TIDs.

2.4 Simulation and Analysis

In the case of the ocean surface, the integration over the temporal frequencies ω_{mn} and ω_{pq} may be performed by the respective linear dispersion relationships between them and the ocean wavenumbers $\vec{K}_{mn}$ and $\vec{K}_{pq}$ for deep water, as given in Eq. (1.23). Then, the autocorrelation function associated with the sea surface profile with respect to the time lag τ is given by,

$$\begin{aligned} \langle \varepsilon(t+\tau)\varepsilon^*(t) \rangle =& \int_{\vec{K}_o} \int_{\omega_o} S_o(\vec{K}_o, \omega_o) e^{j\omega_o \tau} d\vec{K}_o d\omega_o \\ =& \frac{1}{2} \sum_{m=\pm 1} \int_{\vec{K}_o} S_o(m\vec{K}_o) e^{-jm\sqrt{gK_o}\tau} d\vec{K}_o. \end{aligned} \tag{2.26}$$

The relationship between the temporal frequency of the ionospheric irregularities ω_i and its wavenumber $\vec{K}_i$ is deduced by applying the Taylor hypothesis as given in Eq. (2.23). Thus, the autocorrelation function of the IRC becomes

$$\begin{aligned}\langle R_i(t+\tau)R_i^*(t)\rangle &= \int_{\vec{K}_i}\int_{\omega_i} S_i(\vec{K}_i,\omega_i)e^{j\omega_i\tau}d\vec{K}_i d\omega_i \\ &= \int_{\vec{K}_i} K_i S_i(K_i)e^{-j(\vec{K}_i\cdot\vec{v}_h+2k_0v_v\cos\theta_i)\tau}d\vec{K}_i.\end{aligned} \tag{2.27}$$

Then, the ionosphere clutter power spectral density (PSD) of the mixed-path propagation for a monostatically configured pulsed radar in Eq. (1.20) becomes

$$\begin{aligned}P_{i1}(\omega_d) =& \frac{A_r}{2\eta_0}\frac{(k_0^2\eta_0\triangle l|I_0|)^2}{(2\pi)^2}\frac{|F(\rho_0)|^2}{R_0^2\rho_0}\sin^2\theta_0(\triangle\rho)^2\int_{\vec{K}_o}\int_{\vec{K}_i}\left(\frac{\vec{K}_o\cdot\vec{K}_s}{K_s^{3/2}}\right)^2 \\ &\cdot\sum_{m=\pm1} S_o(m\vec{K}_o)S_i(K_i)\delta(\omega_d+m\sqrt{gK_o}+\vec{K}_i\cdot\vec{v}_h+2k_0v_v\cos\theta_i) \\ &\cdot Sa^2\left[\frac{\triangle\rho}{2}\{K_s-k_0(1+\sin\theta_0)\}\right]d\vec{K}_o d\vec{K}_i.\end{aligned} \tag{2.28}$$

The integral in this equation is evaluated in detail in Appendix A. Then, the ionospheric clutter power density in the direction ϕ_s may be written in the form of a standard radar range equation as

$$P_{i1}(\omega_d,\phi_s) = \frac{\lambda_0^2P_tG_tG_r}{(4\pi)^3}\frac{|F(\rho_0)|^2R_{ia}^2A_i}{R_0^2\rho_0^2}\cdot\left[2^5\pi^2k_0^2\frac{1}{\sqrt{g}}\Psi(\omega_d,\phi_s)\right], \tag{2.29}$$

where $P_t = \frac{|I_0|^2\eta_0k_0^2(\Delta l)^2}{12\pi}$ is the total free space transmitted power of an elementary dipole transmitting antenna, $G_t = \frac{3}{2}\sin^2\theta_0$ is the free space gain of the transmitting antenna in the direction θ_0, $G_r = \frac{4\pi A_r}{\lambda_0^2}$ is the free space gain of the receiving antenna, R_{ia} accounts for ionospheric attenuation as mentioned in Section 2.3.1, $A_i = \rho_0\Delta\rho\Delta\phi_s$ is the area of ocean surface scattering patch for ionospheric clutter, and $\Psi(\omega_d,\phi_s)$ involves a single numerical integration over K_i, which is defined in Appendix A.

The ionospheric clutter power density will be compared with the average peak power density obtained from the first-order scatter of the ocean surface at the same apparent range. Since the first-order ocean clutter is, of course, the dominant radar return from the ocean surface, this comparison will give an indication of the importance of $P(\omega_d)$ in the overall radar clutter. Thus, the average peak power density of the first-order ocean clutter in the ϕ_s direction is given as

$$P_{o1}(\phi_s) = \frac{\lambda_0^2 P_t G_t G_r}{(4\pi)^3} \frac{|F(\rho_0)|^4 A_o}{\rho_s^4} \cdot \frac{1}{2} \cdot 2^5 k_0^4 \pi \left[S_o(2k_0, \phi_s) + S_o(2k_0, \phi_s + \pi) \right], \quad (2.30)$$

where $\rho_s = (R_0 + \rho_0)/2$ referring to Figure 1.5 is the apparent surface range of the first-order ocean clutter and A_o is the area of ocean surface scattering patch for first-order ocean clutter. Moreover, the actual peak value and bandwidth are system dependent. Thus, it should be noted that any loss terms which are not common in (2.29) and (2.30) must be included in the comparisons. For example, the propagation distance over the ocean surface for the ionosphere clutter is the range ρ_0 and is a one-way loss term. On the other hand, for the ocean first-order clutter, the propagation distance is the apparent range ρ_s and is a two-way loss term.

The normalized ionospheric clutter PSD function is defined as the ratio of P_{i1} and P_{o1} and simulated by applying the derived spectral density model of the IRC and the Pierson-Moskowitz (PM) model of the ocean surface.

Radio waves of different frequencies may be reflected by the ionosphere at different heights. The operating frequency range for which the derived clutter model is applicable is determined by both the maximum detection range of HFSWR and the maximum reflection height of the ionosphere. For HFSWR, the maximum detection range decreases with in-

creasing operation frequency due to increasing surface propagation losses (e.g., about 400 km for 5 MHz and 200 km for 10 MHz). On the other hand, for mixed-path ionospheric clutter, the reflection height of the ionosphere increases with increasing operation frequency (e.g., about 300 km for 5 MHz and 500 km for 10 MHz). Thus, it is appropriate to consider the ionospheric clutter only when the total path length of the mixed-path propagation is smaller than the maximum detection range of the HFSWR. For this reason, the model is applicable to the lower end of the HF band (roughly, 3 to 8 MHz). In Fig 1.2, the ionograms measured at nighttime from Cape Race (Newfoundland) show that the F-layer is at 310 km for radio wave frequency of 4.1 MHz and experimental results indicate that this military-grade HF radar sensed oblique ionospheric clutter at a range of about 325 km. Thus, the simulation here is conducted for F-layer clutter at a height of 310 km with a 4.1-MHz pulse radar. In order to provide a balance between detection range and range resolution, the radar pulsed width is chosen to be 50 μs. The apparent range is set to be 325 km, which means the ionospheric clutter is reflected from the ionosphere at the near-vertical direction.

The radar look direction for the monostatic radar is 0° and the surface wind speed over the scattering patch is chosen as 10 m/s while its direction is perpendicular to the radar look direction. The ionospheric plasma drift velocity is an important ionospheric parameter to be considered. The drift velocity changes with latitude and is affected by the solar fluxes [69]. In March 1989, the vertical, northward and eastward drift velocity components of the F-layer at Millstone Hill, United States (mid-latitude) were measured using an incoherent scatter radar and a Digisonde [70]. The vertical velocities are usually in a range from 0 to 20 m/s and the horizontal velocities vary from 0 to 150 m/s. Here, the simulation addresses speeds within such a range. Another important ionospheric parameter is the spatial

wavenumber bandwidth K_{if} of the electron density irregularities. It is shown in Eq. (2.29) that the power density model contains an integral over the wavenumber of the ionospheric irregularities K_i from 0 to K_{if}. For small-scale irregularities, the $in\text{-}situ$ measurements indicate that the contributions from irregularities with wavelengths longer than 1 km are more significant [71]. Thus, the minimum spatial irregularity wavelength λ_{iMin} is chosen to be 1 km and $K_f = 2\pi/\lambda_{iMin}$.

Using the typical values of these main parameters as listed in Table 2.1, a series of numerical simulations will be conducted for varying ionospheric conditions and sea states.

Table 2.1: Main parameters for simulations of mixed-path ionospheric clutter.

radar operating frequency (f_0)	4.1 MHz
radar pulse length (τ_0)	50 μs
radar look direction (ϕ)	0°
ionosphere height ($H/2$)	310 km
apparent range ($(\rho + R)/2$)	325 km
typical ionosphere horizontal speed (v_h)	100 m/s
ionosphere horizontal direction (θ_{ih})	90°
typical ionosphere vertical speed (v_v)	0
typical minimum irregularity wavelength (λ_{iMin})	1 km
wind speed (U)	10 m/s
wind direction (θ)	0°

Firstly, Figure 2.2 illustrates the changes in the normalized Doppler spectrum of the ionospheric clutter with varying horizontal ionospheric velocity magnitudes when the ionospheric plasma drift direction is perpendicular to the radar look direction and the surface wind direction. It is observed that the Doppler bandwidth of the ionospheric clutter is broadened and the intensity of the peaks decreases with increasing ionospheric speed. For lower velocities, the dominant first-order peaks for mixed-path propagation are similar to the Bragg peaks of the first-order sea clutter. A possible reason for this is that the wavelengths of the electron density irregularities in the ionosphere are much longer than the wavelengths of the ocean waves and the radio waves, which makes the reflection of the radio waves on the still ionosphere similar to a specular reflection. However, higher ionospheric velocities may cause significant Doppler spread of the dominant peaks in the spectra. When the horizontal velocity varies from 0 to 150 m/s, the bandwidth of the ionospheric clutter changes from 0 to 0.6 Hz and the power density of the peaks decreases roughly from 53 to 45 dB. The jagged shape for the 150 m/s spectrum may be due to a low resolution used for the numerical simulations. The average normalized power density is greater than 40 dB in all cases, indicating that the first-order normalized ionospheric clutter power density exceeds that of the first-order ocean clutter peak more than 40 dB. This is reasonable as the radio waves involved in the mixed-path propagation travel a much shorter distance over the ocean surface and thus suffer much less surface attenuation than first-order ocean clutter from the same apparent range. In reality, this value may vary with ionospheric absorption, attenuation imposed by the surface, the relative ranges of mixed-path and surface propagation, and the size of the ocean surface scattering patch.

Subsequently, the dependence of the simulated first-order received normalized power

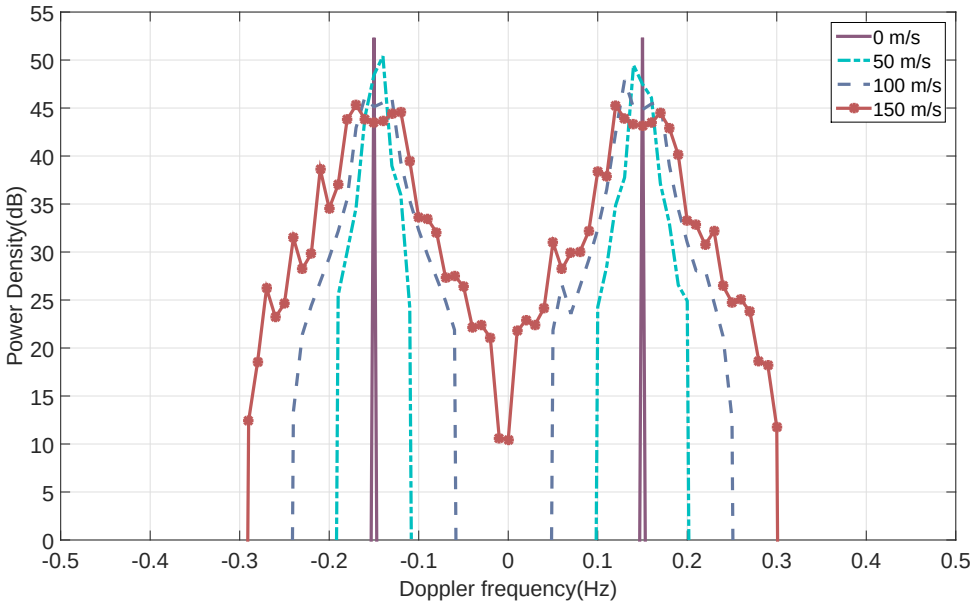

Figure 2.2: Normalized ionospheric clutter PSD for pulsed radar with different horizontal ionospheric plasma drift velocities.

density on vertical ionospheric plasma drift velocities is shown in Figure 2.3. This figure shows that the ionosphere vertical motion only results in a Doppler shift in the ionospheric clutter spectrum without causing further broadening. The bandwidth of each spectrum remains the same for different vertical velocities and the peak power density is also approximately 45 dB. This shifted peak due to the vertical motion of the ionosphere may overlap the Bragg peaks of the ocean clutter. It should be noted that the vertical ionospheric fluctuations due to large-scale TIDs are not considered in these simulations and the vertical velocity of the mean reflecting ionosphere layer is assumed to be constant.

Next, with the horizontal ionospheric plasma drift velocity set as 100 m/s, Figure 2.4 illustrates the variation in the ionospheric clutter normalized PSD with variation in the minimum ionospheric electron density irregularity wavelengths from 500 m to 2 km. This

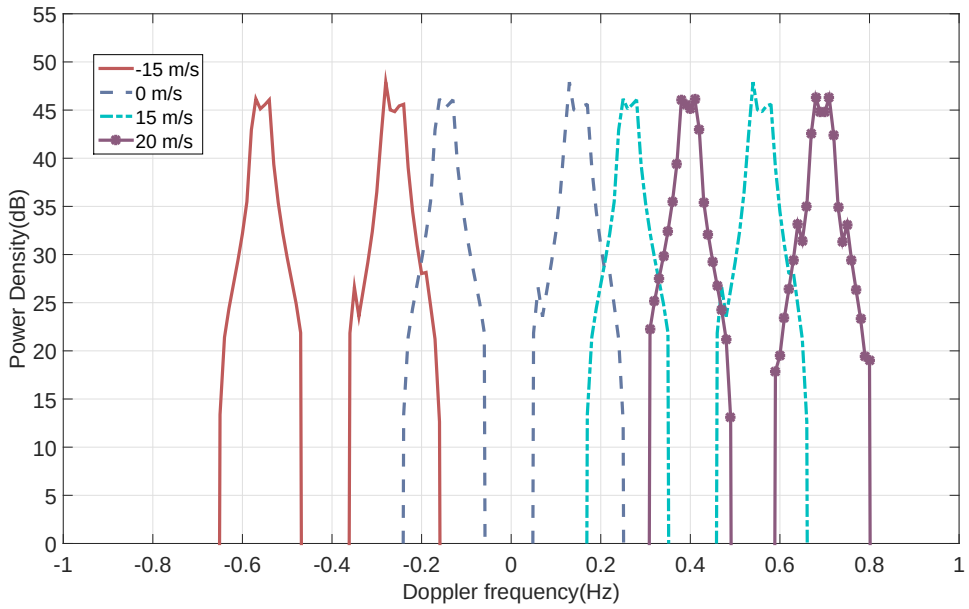

Figure 2.3: Normalized ionospheric clutter PSD for pulsed radar with different vertical ionospheric plasma drift velocities.

figure indicates that the Doppler bandwidth of the ionospheric clutter increases with the wavenumber bandwidth K_f of the IRC. The positions and intensities of the first-order dominant peaks remain the same. Again, the power density ratio of this clutter to the first-order ocean clutter averages around 40 dB.

By setting the surface wind speed as 10 m/s and keeping the other radar parameters and ionospheric conditions unchanged, the simulation results for different wind directions are shown in Figure 2.5. When the wind direction is the same as the radar look direction and the horizontal ionospheric plasma drift direction, the normalized power density achieves its maximum value for negative Doppler frequency, and is the minimum for positive Doppler frequency. This indicates that most of the backscattered energy comes from ocean waves travelling away from the radar, which are generated by the surface winds blowing away.

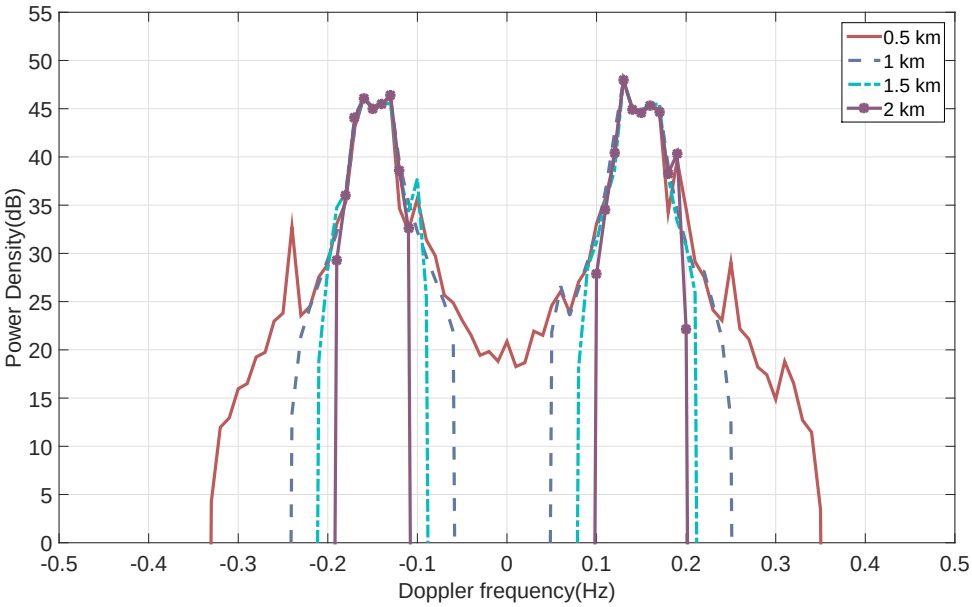

Figure 2.4: Normalized ionospheric clutter PSD for pulsed radar with different minimum ionospheric irregularity wavelengths.

Increasing the angle between the wind direction and the look direction results in increasing normalized power density for positive Doppler frequency. The peak values change with wind direction, while the bandwidths remain the same. As is to be expected, this appears to indicate that the first-order mixed-path received PSD contains information regarding the surface wind direction at the scattering patch of the sea surface. The results depicted here differ from the Doppler spectra generated from real HF radar data since the latter contain both the first and higher order continuum sea clutter and ionospheric clutter at the same apparent range,while these simulations illustrate only the first-order ionospheric clutter normalized to the average peak power density of the first-order ocean clutter.

Finally, the influence of TIDs on the Doppler spectrum is investigated via the time-

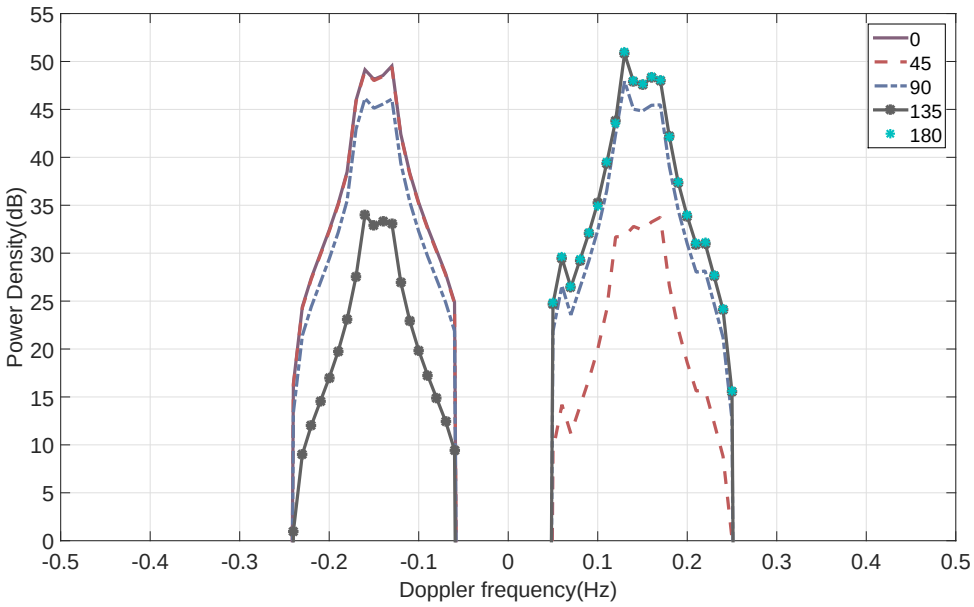

Figure 2.5: Normalized ionospheric clutter PSD for pulsed radar with different surface wind directions.

frequency distributions of the first-order normalized ionospheric clutter PSD [68]. It is assumed that the TID travels horizontally at a speed of 150 m/s with a period of 45 min. The relative reflector surface height variation δ_h is 10%. As shown in Figure 2.6, the speed of the TIDs may introduce roughly 0.3 Hz Doppler shifts into the normalized power density spectra. With the apparent range fixed to 350 km, the variations of the height cause the distortion of the ionospheric reflector and cause the angle of arrival to change periodically. Accordingly, for higher phase speeds of the TID, the bandwidth of the normalized power density is broadened.

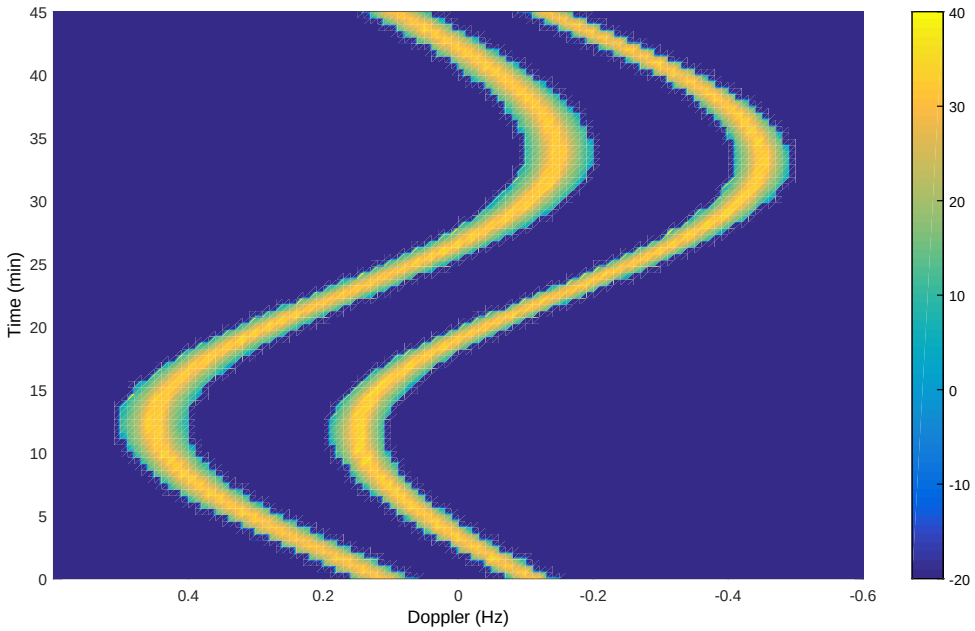

Figure 2.6: Time-frequency distributions of the first-order normalized ionospheric clutter PSD.

2.5 General Chapter Summary

This chapter has been devoted to the modification of the IRC model from that appearing in [41]. The relationship between the ionospheric spectral density of the IRC and the electron density irregularities is derived. This new IRC model includes various ionospheric parameters such as horizontal and vertical ionospheric plasma drift velocities and spatial wavelength of the electron density irregularities, which may better reflect the conditions of the ionosphere. This model may then be incorporated into the ionospheric clutter models for the mixed-path and vertical propagation cases in the following Chapters.

Chapter 3

The HF Radar Power Density Model for the Mixed-Path Propagation Involving Second-Order Sea Scattering With a Pulsed Radar Source

3.1 Introduction

The mixed-path propagation includes two scattering processes: ionospheric reflection and ocean surface scattering. At this stage, the ionospheric reflection may be considered as a first-order scatter from the ionospheric irregularities with a statistical ionospheric reflection coefficient, while the ocean surface scattering involves the first-order and higher-order scattering with ocean surface waves. The measured Doppler spectrum of the ionosphere-

ocean clutter consists of dominant broadened peaks due to the first-order scattering of the ionospheric-reflected radio waves from the ocean. These peaks are always surrounded by continua due to higher-order sea scattering involving ocean waves of many directions and wavelengths.

This chapter represents a continuation of the development of the power spectral density model (PSD) for the mixed-path propagation. The analysis is extended to include contribution due to second-order sea scattering. In this case, the reflected signals from the ionosphere may be scattered back to the receivers by one second-order ocean wave (hydrodynamic effect) or two first-order ocean waves (electromagnetic effect) [54]. First, the general form of the received electric field is investigated by considering the ionospheric reflection and the second-order sea scattering, which involves both electromagnetic and hydrodynamic contributions. Then, this field is inversely Fourier transformed to the time domain, and a pulsed source is incorporated. Subsequently, the second-order received PSD model is developed by assuming that the ionospheric reflection coefficient and the ocean surface can be described as Fourier series whose coefficients are random variables. In order to investigate the power density of the mixed-path propagation and its relative intensity to that of the surface propagation under a variety of ionospheric conditions and sea states, a normalized PSD is simulated [72, 73].

3.2 The Mixed-Path Second-Order Field Equation for Electromagnetic and Hydrodynamic Effects

The geometry of the mixed-path propagation involving second-order sea scattering is shown in Figure 3.1. The X-Y plane represents the mean ocean level and the ionosphere is at a height of $H/2$. The transmitting and receiving antennas are located at the origin. Assuming the ionosphere to be a reflecting plane, the image of the radar source is at a height of H. The transmitted signal may travel upwards to the ionosphere and then be reflected to the sea surface. It may be scattered back to the receiving antennas by one second-order ocean wave (hydrodynamic scattering) at a surface point $(x_1, y_1, 0)$ or two first-order ocean waves (electromagnetic scattering) at surface points $(x_1, y_1, 0)$ and $(x_2, y_2, 0)$.

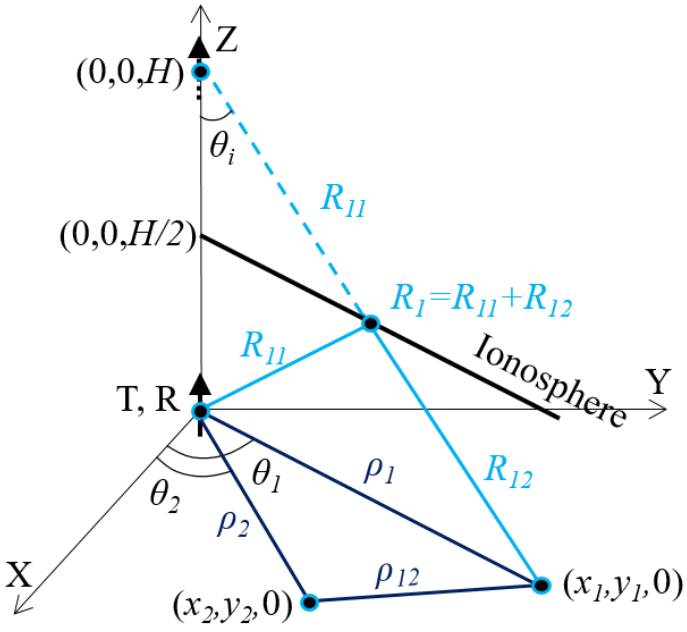

Figure 3.1: Geometry of the mixed-path propagation with second-order sea scattering.

3.2.1 General mixed-path second-order field equation

The derivation of the second-order ocean scattering begins from the rough surface scattering equation for ionosphere-ocean interaction, which is given in Eq. (1.6) as [40]

$$\begin{aligned} &E_{0n}^{+} - \nabla\varepsilon \cdot \nabla(E_{0n}^{+}) \overset{xy}{*} F(\rho)\frac{e^{-jk\rho}}{2\pi\rho} \\ =&E_{szs} - \nabla\varepsilon \cdot 2 \lim_{z\to 0^{+}} \frac{\partial}{\partial z}(\vec{E}_s) \overset{xy}{*} F(\rho)\frac{e^{-jk\rho}}{2\pi\rho}, \end{aligned} \tag{3.1}$$

or, in operator form,

$$E_{0n}^{+} - \mathcal{T}_1(E_{0n}^{+}) = E_{szs},$$

where $\mathcal{T}_1(\cdot)$ is referred to as

$$\nabla\varepsilon \cdot [\nabla(\cdot) - 2 \lim_{z\to 0^{+}} \frac{\partial}{\partial z}(E_s)] \overset{xy}{*} F(\rho)\frac{e^{-jk\rho}}{2\pi\rho}.$$

By successive approximation (Neumann Series), the solution to the second-order of E_{0n}^{+} in Eq. (3.1) may be given as

$$\begin{aligned} E_{0n}^{+} &\approx E_{szs} + \mathcal{T}_1(E_{szs}) + \mathcal{T}_2(E_{szs}) \\ &= (E_{0n}^{+})_0 + (E_{0n}^{+})_1 + (E_{0n}^{+})_2, \end{aligned} \tag{3.2}$$

where $(E_{0n}^{+})_0$ is the expression for propagation over a smooth plane surface and the remaining terms represent scattering due to surface roughness. The first-order solution of the received electric field for mixed-path propagation in Eq. (3.2) may be written as

$$\begin{aligned} (E_{0n}^{+})_1 =&\nabla\varepsilon \cdot [\nabla(E_{szs}) - 2 \lim_{z\to 0^{+}} \frac{\partial}{\partial z}(E_s)] \overset{xy}{*} F(\rho)\frac{e^{-jk\rho}}{2\pi\rho} \\ \sim& - kC_0 \left\{ \left[(\nabla\varepsilon \cdot \hat{\rho}) R_i \sin\theta_i \frac{e^{-jkR_1}}{2\pi R_1} \right] \right. \\ &\left. \overset{xy}{*} F(\rho)\frac{e^{-jk\rho}}{2\pi\rho} \right\}. \end{aligned} \tag{3.3}$$

This first-order electric field for the mixed-path propagation has been investigated by Walsh and briefly reviewed in Section 1.2.3.

The third term in Eq. (3.2), i.e. the second-order solution, may be written in a form similar to that of the first-order as

$$\begin{aligned}(E_{0n}^{+})_2 =&\nabla\varepsilon\cdot\nabla_{xy}[(E_{0n}^{+})_1] \overset{xy}{*} F(\rho)\frac{e^{-jk\rho}}{2\pi\rho}\\ =&-kC_0\{\nabla\varepsilon\cdot\nabla_{xy}[(\nabla\varepsilon\cdot\hat{\rho})R_i\sin\theta_i\frac{e^{-jkR_1}}{2\pi R_1}\\ &\overset{xy}{*} F(\rho)\frac{e^{-jk\rho}}{2\pi\rho}] \overset{xy}{*} F(\rho)\frac{e^{-jk\rho}}{2\pi\rho}\}.\end{aligned} \tag{3.4}$$

Based on the convolution property for functions

$$\nabla_{xy}[f_1(x,y) * f_2(x,y)] = f_1(x,y) * \nabla_{xy}[f_2(x,y)],$$

and the fact that, to a good approximation [54],

$$\nabla_{xy}\left[F(\rho)\frac{e^{-jk\rho}}{2\pi\rho}\right] \approx -jkF(\rho)\frac{e^{-jk\rho}}{2\pi\rho}\hat{\rho},$$

Eq. (3.4) becomes

$$\begin{aligned}(E_{0n}^{+})_2 =&\frac{jk^2C_0}{(2\pi)^3}\left\{\left[(\nabla\varepsilon\cdot\hat{\rho})R_i\sin\theta_i\frac{e^{-jkR_1}}{R_1}\right]_1\right.\\ &\left.\overset{xy}{*}\left[(\nabla\varepsilon\cdot\hat{\rho})F(\rho)\frac{e^{-jk\rho}}{\rho}\right]_2 \overset{xy}{*}\left[F(\rho)\frac{e^{-jk\rho}}{\rho}\right]_3\right\},\end{aligned} \tag{3.5}$$

where $[\cdots]_1$ accounts for propagation from transmitter to the ionosphere, reflected to the ocean surface and scattering at $(x_1, y_1, 0)$, and $[\cdots]_2$ and $[\cdots]_3$ account for propagation from $(x_1, y_1, 0)$ to the point of reception along ρ_{12} and ρ_2 with scattering at $(x_2, y_2, 0)$.

The ocean surface profile ε is assumed to be a stochastic process. The variation of the ionospheric reflection coefficient R_i is fundamentally caused by the random fluctuations of the electron density within the ionospheric layers. When the influence of ionospheric

absorption and the Earth's magnetic field can be neglected, it may also be taken as a zero mean real random variable, as discussed in Chapter 2. Then, these two parameters will be represented, respectively, by general spatial Fourier forms with random Fourier coefficients $P^o_{\vec{K}_o}$ and $P^i_{\vec{K}_i}$ corresponding to the wavenumber components of the ocean waves and the ionospheric irregularities. At this stage, the dependencies of $P^o_{\vec{K}_o}$ on various sea states and $P^i_{\vec{K}_i}$ on various ionospheric conditions are not explicitly considered. This discussion occurs in Section 3.4 following specification of particular representations of the spectral densities of the sea surface profile and the IRC. Also, during one pulse case, the sea surface and the ionospheric electron density may be considered as fixed as was discussed in Section 1.2.3.

Substituting the Fourier forms into Eq. (3.5) gives

$$\begin{aligned}(\nabla\varepsilon\cdot\hat{\rho})_1 &= \nabla[\varepsilon(x_1,y_1)]\cdot\hat{\rho}_1 \\ &= j\sum_{\vec{K}_{mn}} P^o_{\vec{K}_{mn}} e^{j\vec{K}_{mn}\cdot\vec{\rho}_1} K_{mn}\cos(\theta_{mn}-\theta_1)\end{aligned}$$

and

$$\begin{aligned}(\nabla\varepsilon\cdot\hat{\rho})_2 &= \nabla[\varepsilon(x_2,y_2)]\cdot\hat{\rho_{12}} \\ &= j\sum_{\vec{K}_{pq}} P^o_{\vec{K}_{pq}} e^{j\vec{K}_{pq}\cdot\vec{\rho}_2} K_{pq}\cos(\theta_{pq}-\theta_{12}),\end{aligned}$$

where $\vec{K}_{mn}$ and $\vec{K}_{pq}$ are the two first-order wavenumber components of the ocean waves, θ_{mn} and θ_{pq} are directions of these waves, and θ_{12} is the direction of $\vec{\rho_{12}}$. Then, Eq. (3.5)

may be written in an integral form as

$$
\begin{aligned}
(E_{0n}^{+})_2 = & -\frac{jk^2C_0}{(2\pi)^3}\sum_{\vec{K}_{mn}}\sum_{\vec{K}_i}\sum_{\vec{K}_{pq}} P_{\vec{K}_{mn}} P_{\vec{K}_i} P_{\vec{K}_{pq}} \\
& \int_{A_1}\int_{A_2} K_{mn}\cos(\theta_{mn}-\theta_1) K_{pq}\cos(\theta_{pq}-\theta_{12}) \\
& \cdot e^{j\vec{K}_{mn}\cdot\vec{\rho}_1} e^{j\vec{K}_i\cdot\vec{\rho}_1} e^{j\vec{K}_{pq}\cdot\vec{\rho}_2}\sin\theta_i \frac{e^{-jkR_1}}{R_1} \\
& \cdot F(\rho_{12})F(\rho_2)\frac{e^{-jk\rho_{12}}}{\rho_{12}}\cdot\frac{e^{-jk\rho_2}}{\rho_2} dA_2 dA_1,
\end{aligned}
\tag{3.6}
$$

where $dA_1 = dx_1 dy_1$ and $dA_2 = dx_2 dy_2$ are differential vector areas at the points (x_1, y_1) and (x_2, y_2) on the scattering surface. The double integral in Eq. (3.6) is defined as

$$
\begin{aligned}
I = & \int_{A_1}\sin\theta_i \frac{e^{-jkR_1}}{R_1} e^{j\vec{K}_{mn}\cdot\vec{\rho}_1} e^{j\vec{K}_i\cdot\vec{\rho}_1} K_{mn}\cos(\theta_{mn}-\theta_1) \\
& K_{pq}\int_{A_2}\cos(\theta_{pq}-\theta_{12}) e^{j\vec{K}_{pq}\cdot\vec{\rho}_2} F(\rho_{12})F(\rho_2) \\
& \cdot\frac{e^{-jk(\rho_{12}+\rho_2)}}{\rho_{12}\rho_2} dA_2 dA_1.
\end{aligned}
\tag{3.7}
$$

The A_2-integral with respect to the second scattering point (x_2, y_2) is firstly examined as

$$
\begin{aligned}
I_{A_2} = & \int_{A_2}\cos(\theta_{pq}-\theta_{12}) e^{j\vec{K}_{pq}\cdot\vec{\rho}_2} F(\rho_{12})F(\rho_2) \\
& \cdot\frac{e^{-jk(\rho_{12}+\rho_2)}}{\rho_{12}\rho_2} dA_2.
\end{aligned}
\tag{3.8}
$$

For a given sampling time, the total range of $\rho_{12} + \rho_2$ is fixed. Thus, as depicted in Figure 3.2, the locus of second scattering point (x_2, y_2) on the ocean surface is an ellipse and its foci are $(0, 0)$ and (x_1, y_1). Similar to the first-order case, it is convenient to change to elliptic coordinates in order to seek a stationary phase approximation of I_{A_2}. Referencing Figure 3.2, this is accomplished by: rotating the coordinate axis by θ_1, shifting the origin halfway along ρ_1, and introducing elliptic coordinates μ and δ to express (x_2, y_2). Then, we

have

$$\begin{cases} x_2 = \rho_1/2[(1+\cosh\mu\cos\delta)\cos\theta_1 - \sinh\mu\sin\delta\sin\theta_1], \\ y_2 = \rho_1/2[(1+\cosh\mu\cos\delta)\sin\theta_1 + \sinh\mu\sin\delta\cos\theta_1]. \end{cases} \tag{3.9}$$

From the geometry relationships between the distance vectors and their defining coordinates appearing in Figure 3.2, it may be shown that

$$\begin{cases} \rho_2 = \sqrt{x_2^2 + y_2^2} = \frac{\rho_1}{2}(\cosh\mu + \cos\delta), \\ \rho_{12} = \sqrt{(x_2 - x_1)^2 + (y_2 - y_1)^2} = \frac{\rho_1}{2}(\cosh\mu - \cos\delta). \end{cases} \tag{3.10}$$

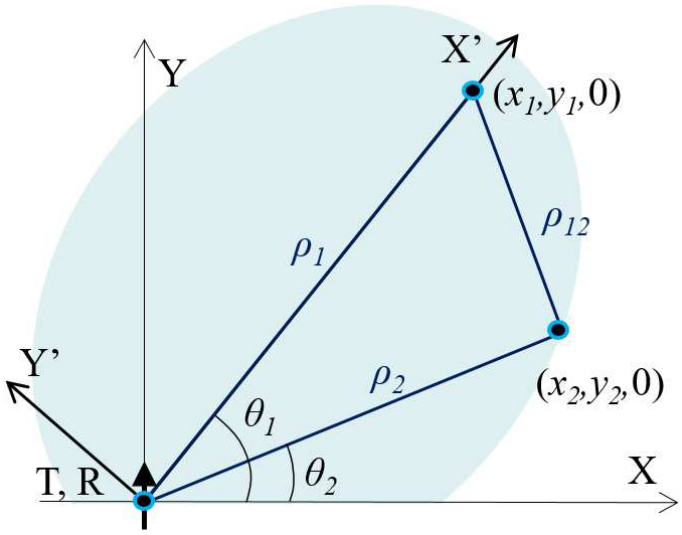

Figure 3.2: Elliptic locus of the second scattering point in the X-Y plane.

The Jacobian of the transformation gives that $dx_2dy_2 = \rho_{12}\rho_2 d\mu d\delta$. Thus, Eq. (3.8) reduces to

$$\begin{aligned} I_{A_2} = \int_\mu \int_\delta & \cos(\theta_{pq} - \theta_{12}) F(\rho_{12}) F(\rho_2) \\ & \cdot e^{j\Phi_{23}(\mu,\delta)} d\mu d\delta, \end{aligned} \tag{3.11}$$

where

$$\begin{aligned}\Phi_{23} =&\vec{\rho}_2 \cdot \vec{K}_{pq} - k(\rho_{12} + \rho_2) \\ =&\rho_1/2\{K_{pq}[(1 + \cosh\mu\cos\delta)\cos(\theta_{pq} - \theta_1) \\ &+ \sinh\mu\sin\delta\sin(\theta_{pq} - \theta_1)] - 2k\cosh\mu\}.\end{aligned}$$

K_{pq} is a typical wavenumber associated with ocean gravity waves, which is of order approximately 10^1 to 10^{-2} m^{-1} [50]. Then, the scattering range ρ_1 may likely be several kilometres. Therefore, $\rho_1 K_{pq}/2$ in the phase term of Φ_{23} may be taken to be a large parameter. Thus, the significant contributions to I_{A_2} may be determined via a modification of a two-dimensional stationary phase method. According to this theory, the stationary points of the integral in Eq. (3.11) are the solutions to the equations

$$\frac{\partial\Phi_{23}(\mu,\delta)}{\partial\mu} = 0, \quad \frac{\partial\Phi_{23}(\mu,\delta)}{\partial\delta} = 0.$$

The stationary points may be shown to be

$$\begin{cases} \mu = 0, \text{ and } \delta = 0, \\ \mu = 0, \text{ and } \delta = \pm\pi, \\ \tanh\mu = \frac{\sqrt{K_{pq}^2 - 4k^2\cos^2(\theta_{pq}-\theta_1)}}{2k\sin(\theta_{pq}-\theta_1)}, \\ \text{and } \tan\delta = \frac{\sqrt{K_{pq}^2 - 4k^2\cos^2(\theta_{pq}-\theta_1)}}{2k\cos(\theta_{pq}-\theta_1)}. \end{cases}$$

These points may be seen to represent the following physical situations: 1) Based on Eq. (3.10) and Figure 3.2, $(\mu, \delta) \equiv (0, 0)$ indicates that $\rho_2 = \rho_1$ and $\rho_{12} = 0$, which means a double scatter near (x_1, y_1). This phenomenon is referred to as "patch scatter" when applied to a pulsed radar. 2) $(\mu, \delta) \equiv (0, \pm\pi)$ gives that $\rho_{12} = \rho_1$ and $\rho_2 = 0$, indicating that the second scatter occurs near the receiving antenna. 3) The scatter for the third case occurs

elsewhere than at the remote patch or the receiver and is referred to as “off-patch” scatter. It has been discussed elsewhere [53] that patch scatter provides the largest contribution to the received field when the transmitter and receiver are narrow beam in nature. Only this case is considered in this chapter.

3.2.2 Patch scatter field equation

Referring to Figure 3.1, for the patch scatter condition, the A_2-integral in Eq. (3.8) may also be written in polar coordinates, in which case, $dA_2 = \rho_{12} d\rho_{12} d\theta_{12}$. Since $\rho_{12} \ll \rho_1$ and ρ_2, $\rho_2 \approx \rho_1 - \hat{\rho}_1 \cdot \vec{\rho}_{12}$. Using $\vec{\rho}_2 = \vec{\rho}_1 - \vec{\rho}_{12}$ and $\rho_1 \approx \rho_2$, I_{A_2} becomes

$$\begin{aligned} I_{A_2} =& F(\rho_1) \frac{e^{-jk\rho_1}}{\rho_1} e^{j\vec{K}_{pq}\cdot\vec{\rho}_1} \int_{\rho_{12}} \int_{\theta_{12}} \cos(\theta_{pq} - \theta_{12}) F(\rho_{12}) \\ & \cdot e^{-jk\rho_{12}} e^{j\vec{\rho}_{12}\cdot(k\hat{\rho}_1 - \vec{K}_{pq})} d\theta_{12} d\rho_{12}. \end{aligned} \tag{3.12}$$

Defining $\vec{K}_T = k\hat{\rho}_1 - \vec{K}_{pq}$ and rewriting

$$\begin{aligned} &\cos(\theta_{pq} - \theta_{12}) = \cos[(\theta_{pq} - \theta_T) + (\theta_T - \theta_{12})] \\ &= \cos(\theta_{pq} - \theta_T)\cos(\theta_T - \theta_{12}) - \sin(\theta_{pq} - \theta_T)\sin(\theta_T - \theta_{12}), \end{aligned}$$

the sine function dependency in the θ_{12}-integral will vanish. Then, the θ_{12}-integral becomes (see, for example, [74]),

$$\int_0^{2\pi} \cos(\theta_T - \theta_{12}) e^{j\rho_{12} K_T \cos(\theta_T - \theta_{12})} = 2\pi j J_1(\rho K_T),$$

where J_1 the first-order Bessel function. I_{A_2} reduces to

$$\begin{aligned} I_{A_2} =& 2\pi j \cos(\theta_T - \theta_{pq}) F(\rho_1) \frac{e^{-jk\rho_1}}{\rho_1} e^{j\vec{K}_{pq}\cdot\vec{\rho}_1} \\ & \int_{\rho_{12}} F(\rho_{12}) e^{-jk\rho_{12}} J_1(\rho_{12} K_T) d\rho_{12}. \end{aligned} \tag{3.13}$$

Symbolizing the ρ_{12}-integral as $G(K_T)$, substituting the simplified A_2-integral into the double integral in Eq. (3.7) and transforming the A_1-integral from Cartesian to polar coordinates at the first scattering point (x_1, y_1), Eq. (3.7) may be written as

$$\begin{aligned} I =& 2\pi j \int_{\rho_1} \sin\theta_i F(\rho_1) \frac{e^{-jk(R_1+\rho_1)}}{R_1} \int_{\theta_1} K_{mn}\cos(\theta_{mn}-\theta_1) \\ & K_{pq}\cos(\theta_T-\theta_{pq}) e^{j\vec{K}_s\cdot\vec{\rho}_1} G(K_T) d\rho_1 d\theta_1, \end{aligned} \tag{3.14}$$

where $\vec{K}_s = \vec{K}_{mn} + \vec{K}_i + \vec{K}_{pq}$. The integral with respect to θ_1 may be evaluated asymptotically by the stationary phase technique. The stationary point for θ_1 satisfies the condition that

$$\frac{d}{d\theta_1}[\hat{\rho}_1 \cdot \vec{K}_s] = 0,$$

which implies that $\hat{\rho}_1$ is parallel to the vector sum $\vec{K}_s$, and the θ_1-integral may be approximated as

$$I_{\theta_1} = \sqrt{2\pi}\frac{(\vec{K}_{mn}\cdot\hat{K}_s)(\vec{K}_{pq}\cdot\hat{K}_T)G(K_T)}{R_1\sqrt{\rho_1 K_s}} e^{jK_s\rho_1} e^{-j\pi/4}. \tag{3.15}$$

Thus, the inner integral in Eq. (3.6) reduces to

$$\begin{aligned} I =& (2\pi)^{3/2} j \int_{\rho_1} \sin\theta_i F(\rho_1) \frac{e^{-jk(R_1+\rho_1)}}{R_1} \\ & \cdot \frac{(\vec{K}_{mn}\cdot\hat{K}_s)(\vec{K}_{pq}\cdot\hat{K}_T)G(K_T)}{R_1\sqrt{\rho_1 K_s}} e^{jK_s\rho_1} e^{-j\pi/4} d\rho_1. \end{aligned} \tag{3.16}$$

The simplification of the double integral to a single integral over ρ_1 allows the field in Eq. (3.6) to be written as

$$\begin{aligned} (E_{0n}^{+})_2 =& -\frac{jk^2 C_0}{(2\pi)^{3/2}} e^{-j\pi/4} \sum_{\vec{K}_{mn}} \sum_{\vec{K}_i} \sum_{\vec{K}_{pq}} P_{\vec{K}_{mn}} P_{\vec{K}_i} P_{\vec{K}_{pq}} \\ & \int_{\rho_1} jF(\rho_1)\sin\theta_i \frac{(\vec{K}_{mn}\cdot\hat{K}_s)(\vec{K}_{pq}\cdot\hat{K}_T)G(K_T)}{R_1\sqrt{\rho_1 K_s}} \\ & \cdot e^{jK_s\rho_1} e^{-jk(R_1+\rho_1)} d\rho_1. \end{aligned} \tag{3.17}$$

3.2.3 Received electric field equation for pulsed radar

At this stage, the form of the radar source current $I(\omega)$ contained in C_0 is unspecified. Now, the second-order fields for mixed-path propagation are modified by the imposition of a pulsed source excitation. In order to incorporate this time-domain current, the electric field may be inversely Fourier transformed to the time-domain as

$$\begin{aligned}(E_{0n}^{+})_2(t) =& \frac{-je^{-j\pi/4}}{(2\pi)^{3/2}} \sum_{\vec{K}_{mn}} \sum_{\vec{K}_i} \sum_{\vec{K}_{pq}} P^o_{\vec{K}_{mn}} P^i_{\vec{K}_i} P^o_{\vec{K}_{pq}} \\ & \int_{\rho_1} jF(\rho_1) \sin\theta_i \frac{(\vec{K}_{mn} \cdot \hat{K}_s)(\vec{K}_{pq} \cdot \hat{K}_T) G(K_T)}{R_1 \sqrt{\rho_1 K_s}} e^{jK_s\rho_1} \\ & \cdot \mathcal{F}_t^{-1}\left[kC_0 \cdot e^{-jk(R_1+\rho_1)}\right] d\rho_1,\end{aligned} \tag{3.18}$$

where the inverse Fourier transforms are further written by substituting the time-domain expression of a pulsed radar source given in Eq. (1.18) as

$$\begin{aligned}\mathcal{F}_t^{-1}\left[kC_0 \cdot e^{-jk(R_1+\rho_1)}\right] &= k_0^2 \eta_0 \Delta l I_0 e^{j\omega_0(t-\frac{R_1+\rho_1}{c})} \\ &\cdot \left[h(t-\frac{R_1+\rho_1}{c}) - h(t-\frac{R_1+\rho_1}{c}-\tau_0)\right].\end{aligned}$$

The apparent range that corresponds to the received signal at time t is determined from the Heaviside function

$$[h(t-\frac{R_1+\rho_1}{c}) - h(t-\frac{R_1+\rho_1}{c}-\tau_0)]$$

and thus satisfies the inequality

$$ct - c\tau_0 < R_1 + \rho_1 < ct.$$

Recalling that $R_1 = \sqrt{\rho_1^2 + h^2}$ (see Figure3.1), and defining the apparent range as $\rho_s = \frac{ct}{2} - \frac{c\tau_0}{4}$ and the apparent range resolution as $\Delta\rho_s = \frac{c\tau_0}{2}$, the integral limits of ρ_1 are

given as

$$\rho_{1min} = \rho_s - \frac{\Delta\rho_s}{2} - \frac{h^2}{4(\rho_s - \frac{\Delta\rho_s}{2})},$$
$$\rho_{1max} = \rho_s + \frac{\Delta\rho_s}{2} - \frac{h^2}{4(\rho_s + \frac{\Delta\rho_s}{2})}.$$

In order to carry out the ρ_1-integral in Eq. (3.18), the integration interval center point ρ_0 and the interval length $\Delta\rho$ are defined as

$$\rho_0 = \frac{(\rho_{1min} + \rho_{1max})}{2} = \rho_s \left\{ 1 - \frac{h^2}{4[\rho_s^2 - (\Delta\rho_s/2)^2]} \right\}, \tag{3.19}$$

and

$$\Delta\rho = \frac{(\rho_{1max} + \rho_{1min})}{2} = \Delta\rho_s \left\{ 1 + \frac{h^2}{4[\rho_s^2 - (\Delta\rho_s/2)^2]} \right\}. \tag{3.20}$$

Then, the integration variable is changed from ρ_1 to ρ', where $\rho' = \rho_1 - \rho_0$. Adopting the following approximation

$$R_1 = \sqrt{(\rho' + \rho_0)^2 + h^2} \sim R_0 \sqrt{1 + \frac{2\rho'\rho_0}{R_0^2}} \sim R_0 + \sin\theta_i \rho',$$

the ρ_1-integrals in Eq. (3.18) may be cast as

$$\begin{aligned} I_{\rho_1} \sim & e^{jK_s\rho_0} e^{j2k_0(\rho_s + \Delta\rho_s/2)} e^{-jk_0(\rho_0 + R_0)} \frac{F(\rho_0)\sin\theta_i}{R_0\sqrt{\rho_0}} \\ & \cdot \int_{-\frac{\Delta\rho}{2}}^{\frac{\Delta\rho}{2}} e^{j[K_s - k_0(1+\sin\theta_i)]\rho'} d\rho' \\ = & e^{jK_s\rho_0} e^{j2k_0(\rho_s + \Delta\rho_s/2)} e^{-jk_0(\rho_0 + R_0)} \frac{F(\rho_0)\sin\theta_i}{R_0\sqrt{\rho_0}} \\ & \cdot \Delta\rho Sa\left\{ \frac{\Delta\rho}{2}[K_s - k_0(1+\sin\theta_i)] \right\}. \end{aligned} \tag{3.21}$$

By invoking the properties of the Bessel function as in [54], $G(K_T)$, defined in association with Eq. (3.13), may be written as

$$\begin{aligned} G(K_T) &= -\frac{1}{K_T} \int_{\rho_{12}} F(\rho_{12}) e^{-jk\rho_{12}} \cdot \frac{d}{d\rho_{12}} [J_0(\rho_{12}K_T)] d\rho_{12} \\ &\sim \frac{1}{K_T} \left\{ 1 - jk \int_{\rho_{12}} F(\rho_{12}) e^{-jk\rho_{12}} J_0(\rho_{12}K_T) d\rho_{12} \right\}. \end{aligned} \tag{3.22}$$

Evaluating the Sommerfeld-type integral as

$$\int_{\rho_{12}} F(\rho_{12}) e^{-jk\rho_{12}} J_0(\rho_{12} K_T) d\rho_{12} = \frac{1}{\sqrt{K_T^2 - k^2} + jk\Delta}$$

with Δ being the surface impedance, $G(K_T)$ becomes

$$G(K_T) \sim \frac{1}{K_T} \left[1 - j \frac{k_0(1+\Delta)}{\sqrt{K_T^2 - k_0^2} + jk_0\Delta} \right], \tag{3.23}$$

where K_T may be further expressed in terms of $\vec{K}_{mn}$, $\vec{K}_{pq}$ and $\vec{K}_i$ as

$$K_T = \sqrt{k_0^2 - \frac{2(\vec{K}_{mn} + \vec{K}_i) \cdot \vec{K}_{pq} + (1 - \sin\theta_i) K_{pq}^2}{1 + \sin\theta_i}}. \tag{3.24}$$

Then, the electric field becomes

$$\begin{aligned} {}_E(E_{0n}^+)_2(t) = & - \frac{jk_0^2 \eta_0 \Delta l I_0}{(2\pi)^{3/2}} e^{-j\pi/4} e^{j2k_0(\rho_s + \Delta\rho_s/2)} \\ & \cdot e^{-jk_0(\rho_0 + R_0)} \sum_{\vec{K}_{mn}} \sum_{\vec{K}_i} \sum_{\vec{K}_{pq}} P^o_{\vec{K}_{mn}} P^i_{\vec{K}_i} P^o_{\vec{K}_{pq}} \\ & \cdot \frac{{}_E\Gamma_p F(\rho_1) \sin\theta_i}{R_1 \sqrt{\rho_1}} \frac{(\vec{K}_{mn} + \vec{K}_{pq}) \cdot \hat{K}_s}{\sqrt{K_s}} e^{jK_s\rho_0} \\ & \cdot \Delta\rho Sa \left\{ \frac{\Delta\rho}{2} \left[K_s - k_0(1 + \sin\theta_i) \right] \right\}, \end{aligned} \tag{3.25}$$

where ${}_E\Gamma_P$ is defined as the electromagnetic coupling coefficient for mixed-path patch scatter and may be written as

$$\begin{aligned} {}_E\Gamma_P = & k_0 \left\{ \frac{(\vec{K}_{mn} \cdot \hat{K}_s)(\vec{K}_{pq} \cdot \hat{K}_T)}{\sqrt{K_T^2 - k_0^2} + jk_0\Delta} \right\} \\ & \cdot \left\{ \frac{j\sqrt{K_T^2 - k_0^2} + k_0}{(\vec{K}_{mn} + \vec{K}_{pq}) \cdot \hat{K}_s K_T} \right\}. \end{aligned} \tag{3.26}$$

This parameter involves the ionospheric reflection coefficient and the interaction of the transmitted radio wave vector $\vec{k}$ with the surface wave vectors $\vec{K}_{mn}$ and $\vec{K}_{pq}$.

Another portion of the second-order field arises from single scatters by second-order ocean waves, which are generated by the hydrodynamic coupling of two first-order ocean waves. Noting that the ocean surface profile ε in Eq. (1.16) is actually the sum of all orders of surface displacement, it may be modified to second-order as [75]

$$\begin{aligned}\varepsilon(x,y) =_1 \varepsilon(x,y) +_2 \varepsilon(x,y) = \sum_{\vec{K}_o} {}_1P^o_{\vec{K}_o} e^{j\vec{K}_o\cdot\vec{\rho}} \\ + \sum_{\vec{K}_{mn}}\sum_{\vec{K}_{pq}} {}_H\Gamma_P \, {}_1P^o_{\vec{K}_{mn}} \, {}_1P^o_{\vec{K}_{pq}} e^{j\vec{K}_{mn}\cdot\vec{\rho}} e^{j\vec{K}_{pq}\cdot\vec{\rho}},\end{aligned} \tag{3.27}$$

where $\vec{K}_{mn} + \vec{K}_{pq} = \vec{K}_o$, and ${}_H\Gamma_P$ is the hydrodynamic coupling coefficient. This equation emphasizes that the wavenumber K_o of the second-order gravity wave arises from the sum of the wavenumbers of the two first-order components. However, it should be noted that $\vec{K}_o$ does not follow the linear dispersion relationship (i.e. $\omega \neq \sqrt{gk}$). The factor ${}_H\Gamma_P$ accounts for the manner in which the first-order waves couple to give the second-order wave. For the deep water, this parameter is given as [76]

$$\begin{aligned}{}_H\Gamma_P =& \frac{1}{2}\left\{ K_{mn} + K_{pq} - \frac{g}{\omega_1\omega_2}(K_{mn}K_{pq} - \vec{K}_{mn}\cdot\vec{K}_{pq}) \right. \\ & \left. \cdot \left[\frac{gK_o + (\omega_1+\omega_2)^2}{gK_o - (\omega_1+\omega_2)^2}\right]\right\}.\end{aligned} \tag{3.28}$$

The hydrodynamic contribution to the second-order electric field ${}_H(E^+_{0n})_2(t)$ may be obtained by replacing the first-order ocean wave spectrum with the second-order ocean wave spectrum in Eq. (1.19) for the first-order electric field for mixed-path propagation.

Thus, the total second-order electric field for mixed-path propagation arising due to

scattering occurring remotely from both the transmitter and receiver may be written as

$$\begin{aligned}(E_{0n}^{+})_2(\rho_s) =& {}_E(E_{0n}^{+})_2(t) + {}_H\,(E_{0n}^{+})_2(t) \\ =& -\frac{jk_0^2\eta_0\Delta l I_0}{(2\pi)^{3/2}} e^{-j\pi/4} e^{j2k_0(\rho_s+\Delta\rho_s/2)]} \\ & \cdot e^{-jk_0(\rho_0+R_0)} \sum_{\vec{K}_{mn}} \sum_{\vec{K}_i} \sum_{\vec{K}_{pq}} P^o_{\vec{K}_{mn}} P^i_{\vec{K}_i} P^o_{\vec{K}_{pq}} \\ & \cdot \frac{\Gamma_P F(\rho_0)\sin\theta_i}{R_0\sqrt{\rho_0}} \frac{\vec{K}_o\cdot\hat{K}_s}{\sqrt{K_s}} e^{jK_s\rho_0}\Delta\rho \\ & \cdot Sa\left\{\frac{\Delta\rho}{2}\left[K_s - k_0(1+\sin\theta_i)\right]\right\},\end{aligned} \tag{3.29}$$

where $\Gamma_P = {}_H\Gamma_P + {}_E\Gamma_P$ and the time variable is changed to the corresponding apparent range ρ_s. This second-order equation may be directly comparable with the first-order result Eq. (1.19), which describes the backscattered field due to a single scatter. Apart from the fact that two ocean waves ($\vec{K}_{mn}$ and $\vec{K}_{pq}$) are involved in the scatter, as is evidenced by the presence of $\vec{K}_s$ and Γ_P, it is observed that first- and second-order electric field equations have very similar mathematical forms. The sampling function remaining in Eq. (3.29) has its maximum at $K_s = k_0(1+\sin\theta_i)$ and $\vec{K}_s$ is parallel to the radar look direction over the ocean surface.

3.3 Derivation of the Received Power Spectral Density

It has been mentioned in Section 3.2 that even though the ocean and ionosphere surfaces have a temporal variation, the time necessary for significant changes in the surfaces are much greater than that required for a single electromagnetic scattering. For this reason, the surfaces are considered to be "fixed" during a single measurement. Then, as time progresses, a train of radar pulses are transmitted to carry out a series of measurements. As

there will be a change in the profile of the ocean surface and the height of the ionospheric reflection from one measurement to the next, the time variable t will account for the generation of a time series from which to produce a Doppler spectrum for the appropriate statistical analysis of the received electric field. Thus, the frequencies of the ocean waves ω_o and the ionospheric irregularities ω_i are introduced into the Fourier representations of ε and R_i to indicate the time-varying properties of the ocean surface and the IRC. The corresponding second-order received field may then be written as

$$(E_{0n}^{+})_2(\rho_s,t) = (E_{0n}^{+})_2(\rho_s)e^{j(\omega_{mn}+\omega_o+\omega_{pq})t}. \tag{3.30}$$

During the time series measurement, it is assumed that ε and R_i may be considered to represent stationary, homogeneous and independent random processes. Thus, the autocorrelation of the received electric field may be introduced as

$$\begin{aligned}
\mathcal{R}_{i2}(\tau) =& \frac{A_r}{2\eta_0}\langle (E_{0n}^{+})_2(t+\tau)(E_{0n}^{+})_2^{*}(t)\rangle \\
=& \frac{A_r}{2\eta_0}\frac{(k_0^2\eta_0\Delta l I_0)^2}{(2\pi)^2}\frac{\mid F(\rho_1)\mid^2 \sin\theta_i^2}{R_1^2\rho_1}(\Delta\rho)^2 \\
& \int_{\vec{K}_{mn}}\int_{\vec{K}_i}\int_{\vec{K}_{pq}}\int_{\omega_{mn}}\int_{\omega_i}\int_{\omega_{pq}} \Gamma_P^2\left(\frac{\vec{K}_o\cdot\hat{K}_s}{\sqrt{K_s}}\right)^2 \\
& S_o(\vec{K}_{mn},\omega_{mn})S_i(\vec{K}_i,\omega_i)S_o(\vec{K}_{pq},\omega_{pq}) \\
& \cdot e^{j(\omega_{mn}+\omega_i+\omega_{pq})}Sa^2\left\{\frac{\Delta\rho}{2}\left[K_s - k_0(1+\sin\theta_i)\right]\right\} \\
& d\vec{K}_{mn}d\vec{K}_i d\vec{K}_{pq}d\omega_{mn}d\omega_i d\omega_{pq}.
\end{aligned} \tag{3.31}$$

Here, $*$ represents complex conjugation and the ensemble average of the Fourier coefficients may be written as

$$\begin{aligned}
&\langle P^{o}_{\vec{K}_{mn},\omega_{mn}} P^{i}_{\vec{K}_i,\omega_i} P^{o}_{\vec{K}_{pq},\omega_{pq}} (P^{o}_{\vec{K}_{mn},\omega_{mn}})^{*} (P^{i}_{\vec{K}_i,\omega_i})^{*} (P^{o}_{\vec{K}_{pq},\omega_{pq}})^{*}\rangle \\
&= S_o(\vec{K}_{mn},\omega_{mn})S_i(\vec{K}_i,\omega_i)S_o(\vec{K}_{pq},\omega_{pq})d\vec{K}_{mn}d\vec{K}_i d\vec{K}_{pq}d\omega_{mn}d\omega_i d\omega_{pq}.
\end{aligned}$$

The Fourier transform of $\mathcal{R}_{i2}(\tau)$ with respect to the lag time τ gives the second-order received PSD as

$$\begin{aligned} P_{i2}(\omega_d) =& \mathcal{F}\left[\mathcal{R}_{i2}(\tau)\right] \\ =& \frac{A_r}{2\eta_0}\frac{(k_0^2\eta_0\Delta l I_0)^2}{(2\pi)^2}\frac{\mid F(\rho_1)\mid^2 \sin\theta_i^2}{R_1^2\rho_1}(\Delta\rho)^2 \\ & \int_{\vec{K}_{mn}}\int_{\vec{K}_i}\int_{\vec{K}_{pq}}\int_{\omega_{mn}}\int_{\omega_i}\int_{\omega_{pq}} \Gamma_P^2\left(\frac{\vec{K}_o\cdot\hat{K}_s}{\sqrt{K_s}}\right)^2 \\ & \delta[\omega_d-(\omega_{mn}+\omega_i+\omega_{pq})]S_o(\vec{K}_{mn},\omega_{mn})S_i(\vec{K}_i,\omega_i) \\ & \cdot S_o(\vec{K}_{pq},\omega_{pq})Sa^2\left\{\frac{\Delta\rho}{2}\left[K_s-k_0(1+\sin\theta_i)\right]\right\} \\ & d\vec{K}_{mn}d\vec{K}_i d\vec{K}_{pq}d\omega_{mn}d\omega_i d\omega_{pq}. \end{aligned} \tag{3.32}$$

where ω_d is the observed "Doppler" frequency.

3.4 Simulation and Analysis

In order to carry out the simulations of the second-order received power density for the mixed-path propagation, by applying the transformations in Appendix B the received PSD in Eq. (3.32) is reduced to

$$\begin{aligned} P_{i2}(\omega_d) =& \frac{A_r}{2\eta_0}\frac{(k_0^2\eta_0\Delta l I_0)^2}{2\pi}\frac{\mid F(\rho_1)\mid^2 \sin\theta_i^2\Delta\rho}{R_1^2\rho_1} \\ & \int_{\phi_{mn}}\int_{K_i}\int_{\phi_i}\int_{\phi_s} 2Y^*\Gamma_P^2\left(\vec{K}_o\cdot\hat{K}_s\right)^2 \\ & \sum_{m_1=\pm1}\sum_{m_2=\pm1} S_o(m_1\vec{K}_{mn})S_i(K_i)S_o(m_2\vec{K}_{pq}) \\ & \cdot\mid\frac{\partial Y}{\partial D_p}\mid_{\theta_{mn},Y^*} d\phi_s d\phi_i dK_i d\phi_{mn}. \end{aligned} \tag{3.33}$$

where, as defined in Appendix B, $Y=\sqrt{K_{mn}}$, $D_p(Y,\phi_{mn})=-m_1\sqrt{gK_{mn}}-m_2\sqrt{gK_{pq}}$, and Y^* is the value of Y to make $D_p(Y^*,\theta_{mn})=\omega_o$ with $\omega_o=\omega_d+\vec{K}_i\cdot\vec{v}_h+2k_0v_v\cos\theta_i$.

For narrow beam HF radar, the look direction ϕ_s is specified and the simulation will be carried out over the ϕ_i-, K_i- and ϕ_{mn}-integrals.

The resulting power density of the second-order mixed-path propagation is investigated numerically and a series of simulations are conducted under a variety of ionospheric conditions and sea states. The PSD of the second-order ionospheric clutter for mixed-path propagation is also normalized by the average peak power density of the first-order ocean clutter for the same apparent range as

$$P_n = \frac{P_{i2}}{P_{o1}}. \tag{3.34}$$

The parameters, such as radar operating frequency, radar pulsed width, the height of ionospheric reflection, wind velocity and ionospheric motions, all affect the exact shape of the simulated normalized power density. Typical values of these main parameters involved in the simulation remain the same as listed in Table 2.1.

The normalized second-order PSD of the mixed-path propagation for different horizontal and vertical ionospheric velocities are shown in Figure 3.3 and Figure 3.4, respectively. It can be observed from Figure 3.3 that the general shape of the second-order Doppler spectra remains unchanged when the horizontal ionospheric velocity increases from 0 to 150 m/s, and so does the average power density. The Doppler bandwidths are around 1.5 Hz and the average PSD is roughly 5 dB. However, a small variation in power density at the regions around the Bragg frequencies (here ± 0.15 Hz) can be seen. This may be due to the fact that increases in the horizontal ionospheric velocities may broaden the Doppler bandwidth. As shown in Figure 3.4, the ionosphere vertical motion only results in a Doppler shift in the ionospheric clutter spectrum without causing any Doppler broadening. Specif-

ically, as is to be expected, the upwards ionosphere motion introduces a negative Doppler shift while the downwards motion introduces a positive one. The magnitude of the Doppler shift also depends on the radar operating frequency and the incidence angle of the radio waves at the ionosphere layers. The shape and average power density remain the same for different vertical velocities.

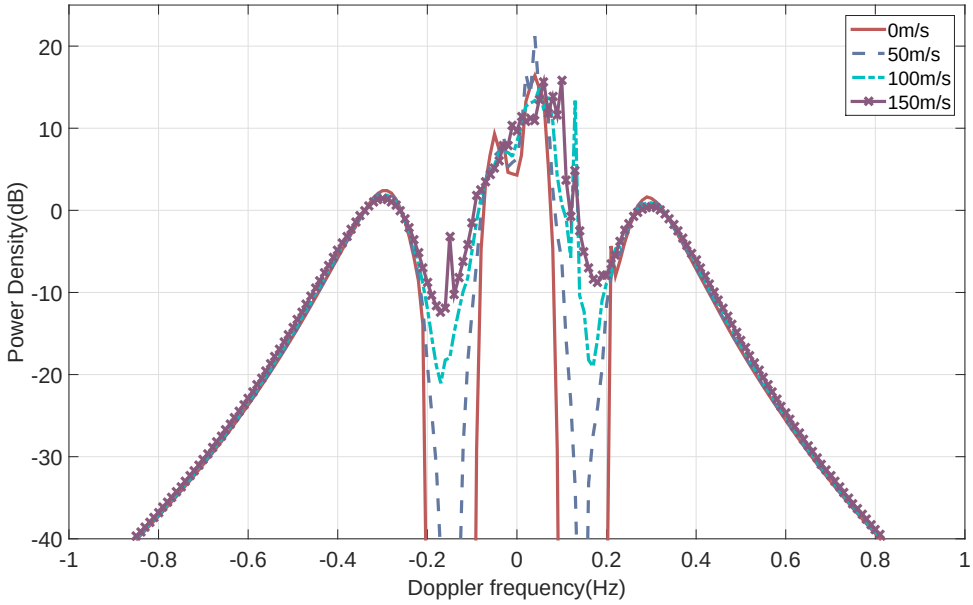

Figure 3.3: Normalized second-order PSD of the ionospheric clutter with different horizontal ionospheric velocities.

The second-order power density may also be influenced by sea surface wind near the scattering patch. As shown in Figure 3.5, when the angle between the surface wind and the radar look direction increases from 0 to $180°$, normalized PSD for the positive Doppler frequency increases and while that for the negative side decreases. The positions of the peaks and the bandwidths are slightly affected by the wind direction. It appears that the

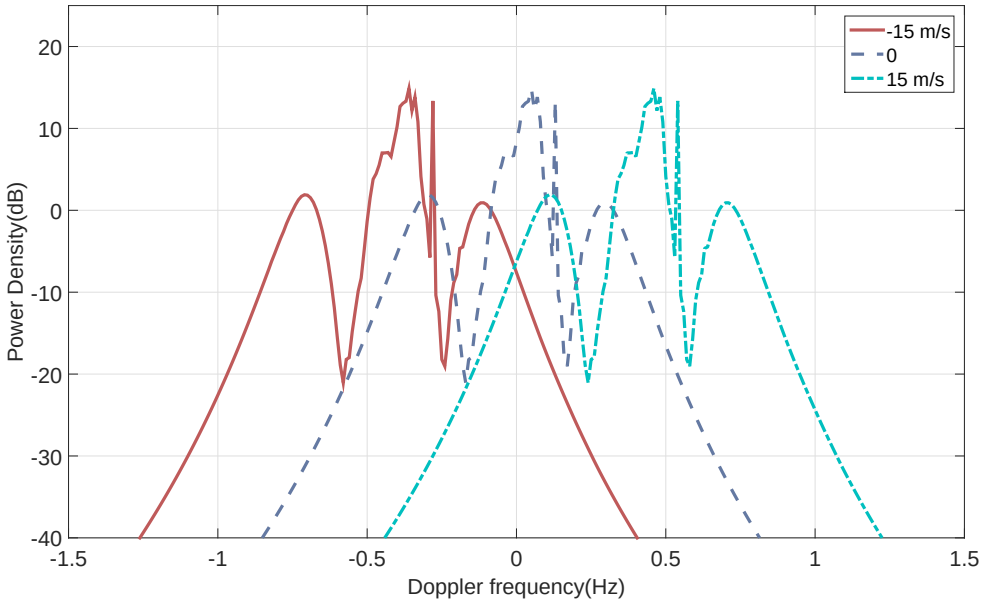

Figure 3.4: Normalized second-order PSD of the ionospheric clutter with different vertical ionospheric velocities.

bandwidth is maximum when the wind direction is perpendicular to the radar look direction. The normalized PSD is also simulated for different wind speeds (see Figure 3.6). It is observed that the average power density increases from -20 to 15 dB and the bandwidth narrows from 2 to 1.6 Hz with increasing wind speeds from 5 to 15 m/s. This may be explained by the fact that at higher wind speeds, the relatively longer wind waves that produce the scatter carry a significant amount of the spectral energy. This indicates that higher sea states may enhance the second-order radar backscatter for mixed-path propagation.

Finally, the simulated first- and second-order received PSD of the mixed-path propagation is compared with the spectrum of field data in Figure 1.3 (b), which was collected at Cape Race, Newfoundland on January 6, 2002 at 20:00 UTC. The radar frequency was 4.1 MHz and the pulsed width of the radar source was 50 μs. The apparent range was 368.8 km

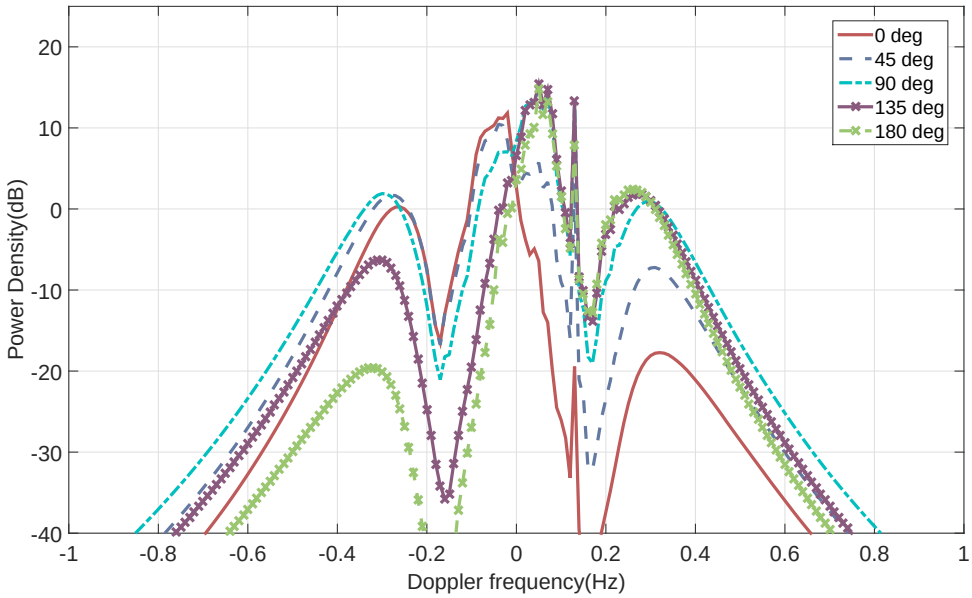

Figure 3.5: Normalized second-order PSD of the ionospheric clutter with different wind directions.

and the azimuth angle is 2°. The real spectrum involves contributions from both the mixed-path propagation and the sea surface propagation. However, for an apparent range over 300 km, the power density of the latter is much lower than that of the former. According to the actual radar configurations, the radar frequency is set to 4.1 MHz and its pulsed width is 50 μs. Other parameters, such as wind velocity, ionospheric motions and attenuation factors, are adjusted to fit the shape of the simulated power density to that of the real power density spectrum. As shown in Figure 3.7, the receding and approaching Bragg peaks due to sea surface propagation are roughly at ± 0.2 Hz, and the two dominant peaks caused by the first-order mixed-path propagation are roughly at -0.4 Hz and -0.08 Hz, respectively. In both cases, the power density of the left peak is higher than that of the right. This indicates that the surface wind was blowing away from the radar. Thus, the direction of the surface

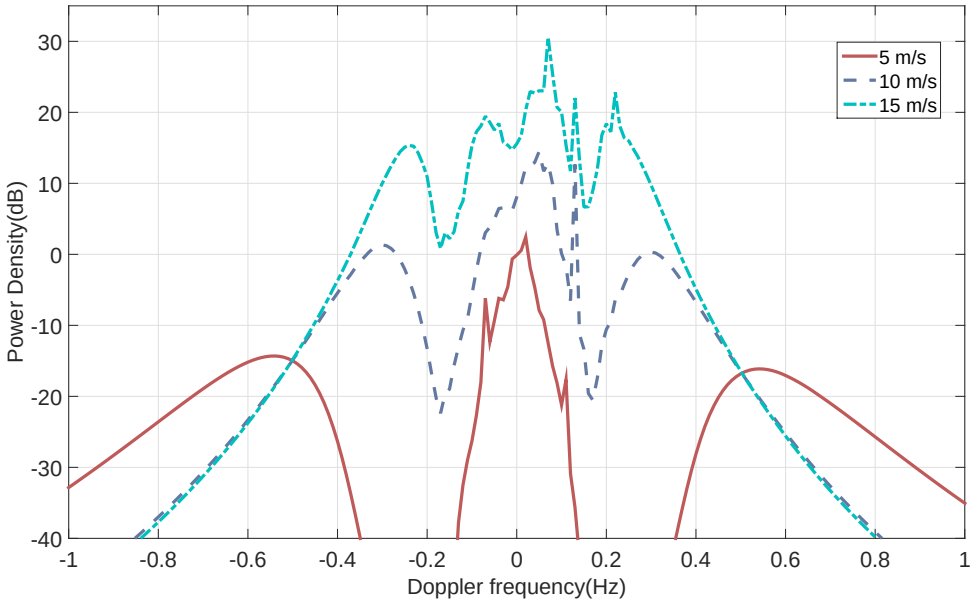

Figure 3.6: Normalized second-order PSD of the ionospheric clutter with different wind velocities.

wind is set to $60°$. Furthermore, it can be observed that the positions of the Bragg peaks for surface wave propagation are symmetric about zero Doppler. This indicates the radial component of the ocean current to be small at the scattering patch. On the other hand, for mixed-path propagation, the second-order PSD appears as the continuum around the first-order dominant peaks. The average power density and the bandwidth are determined by the surface wind speed, which is set to 5 m/s. The mixed-path spectra are shown to have a Doppler shift of 0.16 Hz due to the upward vertical motion of the ionosphere. Based on the theoretical analysis, the corresponding vertical speed is 7.5 m/s. It should be noted that the high power density in some portions of the spectrum for the field data is beyond that accounted for by the model, which may be due to higher order contributions and noise. Using the particular set of parameters listed, the simulated spectrum closely resembles that

obtained from the field experiment.

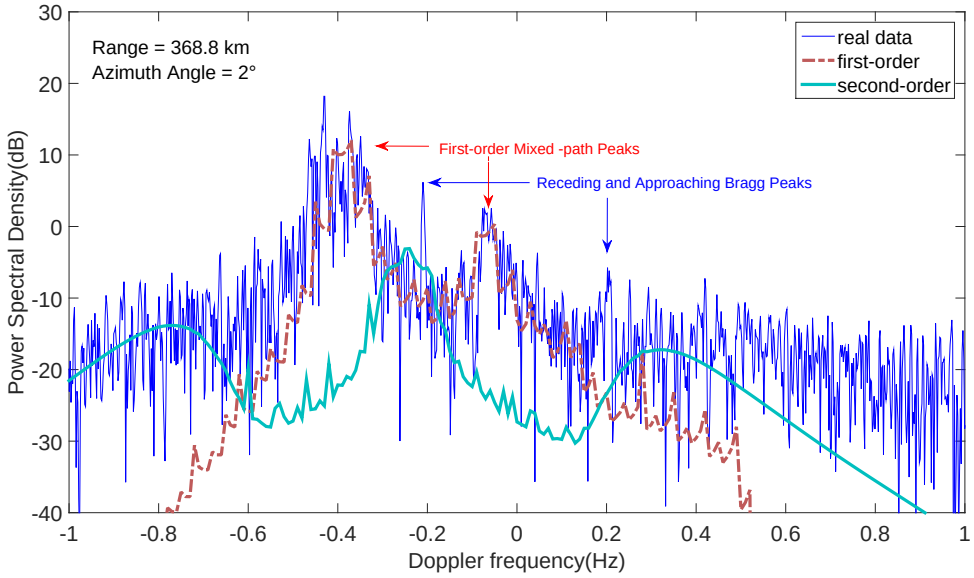

Figure 3.7: Comparison of the simulated PSD and the real spectrum for the mixed-path propagation.

3.5 General Chapter Summary

This chapter has been devoted to the derivation of an ionospheric clutter model for mixed-path propagation with second-order sea scattering. The received electric field was firstly presented, with the ionospheric reflection coefficient and the profile of the ocean surface expressed by a random Fourier form. Then the received power spectral density (PSD) was developed. This model includes the ionospheric reflection, which incorporates a physically meaningful model of the ionospheric reflection coefficient introduced in Chapter 2, as well as the second-order sea scattering, which involves both electromagnetic and hydrodynamic

contributions.

In order to validate the model, the proposed normalized PSD was simulated. A variety of parameters affecting the power density were examined. These included ionospheric horizontal and vertical motions, and surface wind velocities. Simulation results show that different ionospheric conditions and sea states may affect the amplitudes, bandwidths and Doppler shifts of the second-order ionospheric clutter power density. These observations are consistent with field tests.

Chapter 4

Further Analysis of the Ionospheric Clutter Model Incorporating a Pulsed Radar Source

4.1 Introduction

In this Chapter, two special cases for the ionospheric clutter model with a pulsed radar source will be further investigated. One is the case of vertical reflection for monostatic radar. The particular mode analyzed is that associated with a radar signal traveling from the transmitting antenna vertically upwards to the ionosphere being reflected back to the receiving antenna. The electric field and power spectral density (PSD) for the radar return via a single ionospheric reflection are presented by assuming the source to be a continuously excited elementary vertical dipole, and a typical $in\text{-}situ$ spectral density for the

electron density irregularities is incorporated into the derived PSD model. Simulations of the normalized power, which is the power density ratio of the vertical ionospheric clutter to the average first-order ocean clutter peak, for different ionospheric characteristics are then presented. Condensed versions of this analysis appear in [77] and [78].

The second case considered is the first-order mixed-path ionosphere clutter model for the bistatic HF radar [79]. For radar operation in a marine environment, the directional information of the ocean surface characteristics may be obtained by employing the configuration of a single transmitter and two widely separated receivers (one possibly at the transmit location) - the so-called bistatic mode - instead of using two full radar systems. Thus, an understanding of the ionospheric clutter for bistatic HF radar operation will be essential to improving the accuracy and efficiency of this more economical configuration. Based on previous monostatic work, the first-order received electric field for the bistatic configuration is derived by considering the scattering processes on both the ionosphere and the ocean surface. Then, the first-order received PSD model is developed by incorporating a vertically polarized pulsed dipole antenna. Simulations are conducted for varying parameters associated with the bistatic configuration and environmental conditions and a comparison is made with results from a monostatic configuration.

4.2 Ionospheric Clutter Model for the Case of the Vertical Propagation

4.2.1 Derivation for the power spectral density of the vertical ionospheric clutter

As shown in Figure 4.1(a), the ionosphere is assumed to be a reflecting plane at a height $z = H/2$, and thus the primary vertical dipole source at $z = 0$ will have an elevated image source at $z = H$. Ideally, there is no radiation in the vertical direction. However, due to practical limitations imposed by the transmitting antennas and the ground conductivity, a portion of the radio waves may be radiated vertically upwards to the ionosphere. Here, it is assumed that the antenna pattern of the elementary dipole has an angle derivation $\delta\theta$ from the ideal case as shown in Figure 4.1(b). From image theory, the electric field for the vertical ionospheric clutter at the receiving antenna may be written as

$$E_R = jC_0 \sin(\delta\theta) R_{iA} \frac{e^{-jkH}}{4\pi H}, \tag{4.1}$$

where R_{iA} is the average ionosphere reflection coefficient (IRC), which may be written as

$$R_{iA} = \frac{\int\int_S R_i(x,y)dS}{S},$$

where R_i is the IRC at horizontal position(x, y) of the ionospheric scattering point, and the size, S, of the ionospheric scattering patch depends on the beam width of the vertically transmitted signal and the height of the ionosphere [77, 78]. It is assumed that the incident electric field within this patch is uniform.

The received electric field may then be written as

$$E_V = jC_0 \sin(\delta\theta)\frac{e^{-jkH}}{4\pi H}\frac{\int\int_S R_i(x,y)dS}{S}. \tag{4.2}$$

$R_i(x,\ y)$ may be considered as a random process that can be represented by a general Fourier form as

$$R_i(x,y) = \sum_{\vec{K}_i} P_{\vec{K}_i} e^{j\vec{K}_i\cdot\vec{\rho}_i}, \tag{4.3}$$

where $\vec{\rho_i}$ is the horizontal displacement of the radio waves propagating in the ionosphere and its magnitude is the diameter of scattering area size. The value of ρ_i changes from 0 to $\Delta\rho_i$ (several kilometres) - see Figure 4.1(a). The wavenumber $\vec{K_i}$ of the ionosphere irregularity is usually smaller than 10^{-3} m^{-1}. The angle between $\vec{\rho_i}$ and $\vec{K_i}$ is defined as φ. The size of the scattering patch becomes $S = \pi(\Delta\rho_i)^2$.

Inserting Eq. (4.3) into Eq. (4.2) leads to

$$E_V = \frac{jC_0 \sin(\delta\theta)e^{-jkH}}{4\pi^2 H\Delta\rho_i^2}\int_{\rho_i}\int_{\varphi}\sum_{\vec{K}_i} P_{\vec{K}_i} e^{jK_i\rho_i\cos\varphi}\rho_i d\varphi d\rho_i. \tag{4.4}$$

The result of the integral with respect to φ is a zero-order Bessel function

$$\int_{\varphi} e^{jK_i\rho_i\cos\varphi}d\varphi = 2J_0(K_i\rho_i) = 2\sum_{n=0}^{\infty}(-1)^n\frac{(K_i\rho_i/2)^{2n}}{(n!)^2}. \tag{4.5}$$

Thus, Eq. (4.4) reduces to

$$E_V = \frac{jC_0 \sin(\delta\theta)e^{-jkH}}{2\pi^2 H\Delta\rho_i^2}\sum_{\vec{K}_i} P_{\vec{K}_i}\int_0^{\Delta\rho_i} J_0(K_i\rho_i)\rho_i d\rho_i. \tag{4.6}$$

Next, in order to specify the radar current in Eq. (4.6), a dipole antenna that transmits a signal with pulse width of τ_0 and frequency ω_0 is introduced. In order to incorporate the

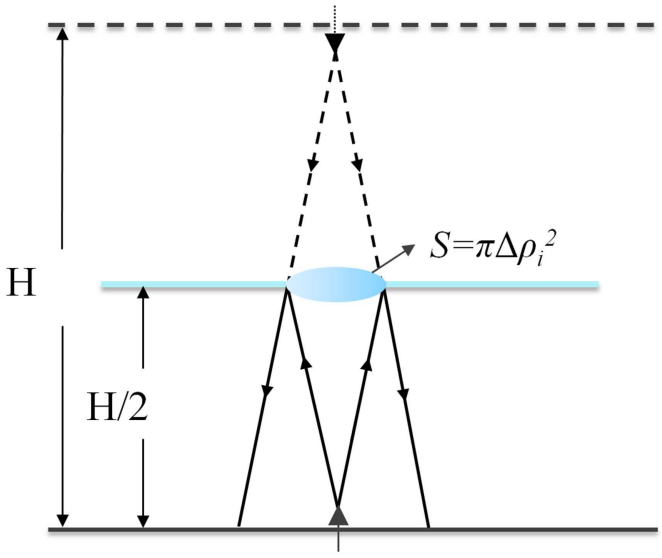

(a)

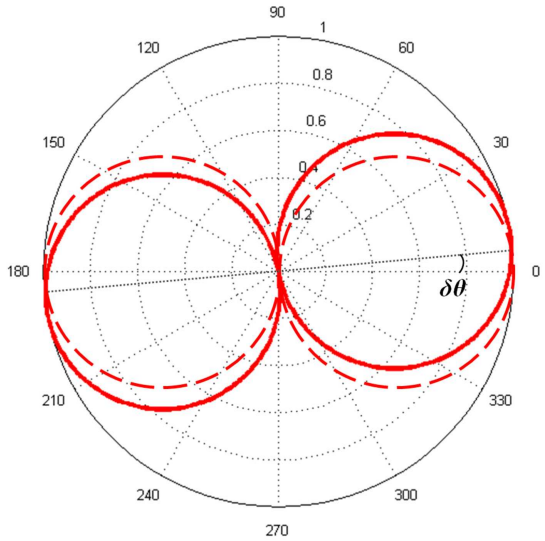

(b)

Figure 4.1: (a) Geometry of the vertical ionospheric clutter and (b) antenna pattern for a vertical dipole.

time-domain pulsed current, Eq. (4.6) is inversely Fourier transformed as

$$\begin{aligned} E_V(t) =& \frac{\sin(\delta\theta)}{2\pi^2 H \Delta\rho_i^2} \left[\mathcal{F}_t^{-1}(jC_0) \overset{t}{*} \delta(t - \frac{H}{c}) \right] \\ & \cdot \sum_{\vec{K}_i} P_{\vec{K}_i} \int_0^{\Delta\rho_i} J_0(K_i\rho_i)\rho_i d\rho_i, \end{aligned} \tag{4.7}$$

where

$$\mathcal{F}_t^{-1}(jC_0) = \tfrac{\eta_0 \Delta l}{c} \cdot \tfrac{di(t)}{dt}$$

$$\approx jk_0\eta_0\Delta l I_0 e^{j\omega_0 t} \left[h(t) - h(t - \tau_0) \right].$$

It should be noted that the leading and trailing edge impulse terms have been ignored in calculating the derivative of $i(t)$. Therefore, Eq. (4.7) becomes

$$\begin{aligned} E_V(t) =& \frac{jk_0\eta_0\Delta l I_0 \sin(\delta\theta)}{2\pi^2 H \Delta\rho_i^2} \left[h(t - \frac{H}{c}) - h(t - \frac{H}{c} - \tau_0) \right] \\ & \cdot e^{j\omega_0(t - \frac{H}{c})} \sum_{\vec{K}_i} P_{\vec{K}_i} \int_0^{\Delta\rho_i} J_0(K_i\rho_i)\rho_i d\rho_i. \end{aligned} \tag{4.8}$$

Here, the ionosphere reflection height that corresponds to the received signal at time t is determined by the range of the Heaviside function $\left[h(t - \frac{H}{c}) - h(t - \frac{H}{c} - \tau_0)\right]$. The mean height H and height resolution ΔH are defined as

$$H_a = \tfrac{ct}{2} - \tfrac{c\tau_0}{4} \quad \text{and } \Delta H_a = \tfrac{c\tau_0}{2},$$

respectively. Thus, for a single transmitted pulse, the received electric field at the height of $(2H_a \pm \Delta H_a)$ may be derived as

$$\begin{aligned} E_V(H_a) =& \frac{jk_0\eta_0\Delta l I_0 \sin(\delta\theta)}{4\pi^2 H_a \Delta\rho_i^2} e^{jk_0(2H_a + \Delta H_a)} \\ & \cdot \sum_{\vec{K}_i} P_{\vec{K}_i} \int_0^{\Delta\rho_i} J_0(K_i\rho_i)\rho_i d\rho_i. \end{aligned} \tag{4.9}$$

The instantaneous average received power density for vertical ionospheric clutter during a pulse is taken to be

$$P_v = \frac{A_r}{2\eta_0}|E_V(H_a)|^2, \tag{4.10}$$

For successive pulses, the Doppler effect of the vertical return is recorded and contains information about the time variation of the ionosphere. The R_i representation is modified by introducing the time variable term $e^{j\Omega t}$ and the autocorrelation of a time series of pulse returns is calculated as

$$R_v(\tau) = \frac{A_r}{2\eta_0}\langle E_V(t+\tau)E_V^*(t)\rangle. \tag{4.11}$$

The evaluation of Eq. (4.11) involves

$$\langle P_{\vec{K}_i,\Omega}, P^*_{\vec{K}_i,\Omega}\rangle = S_{R_i}(\vec{K}_i,\Omega)d\vec{K}_i d\Omega. \tag{4.12}$$

where $S_{R_i}(\vec{K}_i,\Omega)$ is the spectral density of the IRC for the wavenumber $\vec{K}_i$ of the ionospheric irregularities which have frequency Ω.

Then, the autocorrelation of the electric field received from a vertical trajectory above a location (0,0) on the ground may be given as

$$\begin{aligned} R_v(\tau) =& \frac{\eta_0 k_0^2 \Delta l^2 I_0^2 A_r \sin^2(\delta\theta)}{32\pi^4 H_a^2 \Delta\rho_i^4} \int_{\vec{K}_i}\int_{\Omega} S_{R_i}(\vec{K}_i,\Omega) \\ & \cdot \mid \int_0^{\Delta\rho_i} J_0(K_i\rho_i)\rho_i d\rho_i \mid^2 e^{j\Omega\tau} d\vec{K}_i d\Omega. \end{aligned} \tag{4.13}$$

The Fourier transform of Eq. (4.13) with respect to τ gives the vertical received power density of the pulsed radar as

$$\begin{aligned} P_v(\omega_d) = \mathcal{F}[R_v(\tau)] = & \frac{\eta_0 k_0^2 \Delta l^2 I_0^2 A_r \sin^2(\delta\theta)}{32\pi^4 H_a^2 \Delta\rho_i^4} \int_{\vec{K}_i}\int_{\Omega} \\ & S_{R_i}(\vec{K}_i,\Omega) \mid \int_0^{\Delta\rho_i} J_0(K_i\rho_i)\rho_i d\rho_i \mid^2 \delta(\omega_d-\Omega) d\vec{K}_i d\Omega, \end{aligned} \tag{4.14}$$

where ω_d is the observed "Doppler" frequency. The expression of the spectral density for the IRC is specified in Chapter 2.

With the aid of the delta functions, the received power density function in (4.14) reduces to

$$P_v(\omega_d) = \frac{k_0^3 \eta_0 \Delta l^2 I_0^2 A_r \sin^2(\delta\theta)}{32\pi^4 H_a^2 \Delta\rho_i^4} \mid \int_0^{\Delta\rho_i} J_0(\omega_d \rho_i / v_h) \rho_i d\rho_i \mid^2 \cdot (1 + \frac{4 z_0 r_e^2 \lambda_0^2}{k_0} \log \frac{z_0}{z_0 - z_0'} \cdot \frac{8\pi^3 \kappa_0 \langle N_{e1}^2 \rangle}{(\kappa_0^2 + (\omega_d / v_h)^2)^{3/2}} + \cdots). \tag{4.15}$$

4.2.2 Simulation and analysis

The power spectral density of the vertical ionospheric clutter is also investigated by its relative intensity to the average first-order ocean clutter peak power density. The main parameters involved in the simulation are listed in Table 4.1.

Table 4.1: Main parameters for simulations of vertical ionospheric clutter.

radar operating frequency (f_0)	4.1 MHz
radar pulse length (τ_0)	50 μs
ionosphere height ($H/2$)	300 km
patch radius ($\Delta\rho_i$)	2.5 km
typical horizontal ionospheric plasma drift velocity (v_h)	100 m/s
typical vertical ionospheric plasma drift velocity (v_v)	0

The received normalized PSD of the vertical ionospheric clutter for three horizontal ionospheric plasma drift velocities is shown in Figure 4.2. It is observed that the shapes

of the power density are similar to an impulse but with oscillations. The oscillations may be caused by the integral over the phase of the IRC which involves the zero-order Bessel function as given in Eq. (4.6). Furthermore, the ionospheric clutter Doppler bandwidth increases from 0.2 to 0.8 Hz as the ionospheric horizontal velocity changes from 50 to 150 m/s. Moreover, if there is no vertical velocity, the Doppler frequency of the clutter peak is zero. The normalized power density of the peak remains the same with varying horizontal ionospheric velocities and exceeds that of the average first-order ocean clutter peak by about 45 dB.

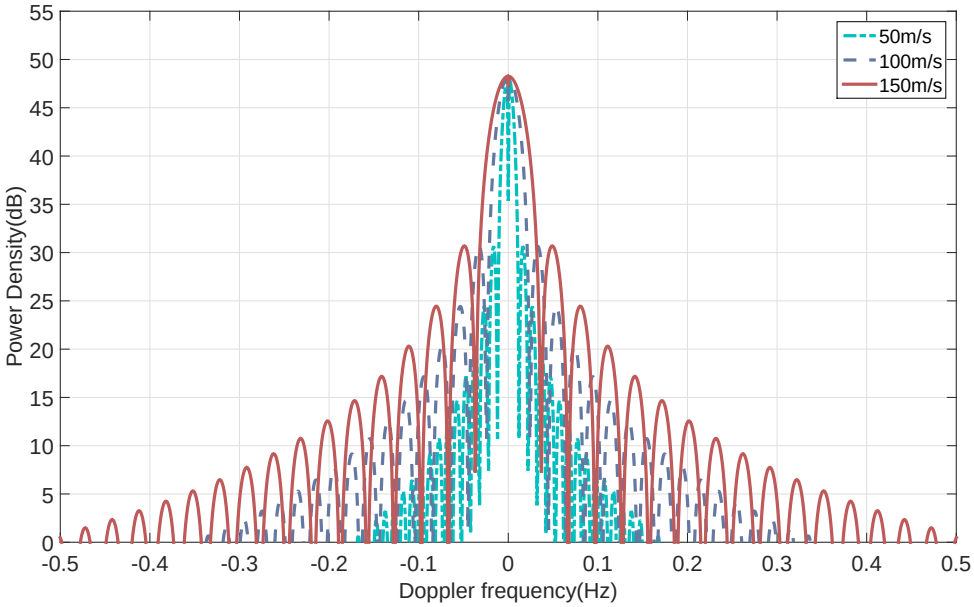

Figure 4.2: Normalized vertical ionospheric clutter PSD with different horizontal ionospheric plasma drift velocities.

Next, with the horizontal ionospheric plasma drift velocity set as 100 m/s, Figure 4.3 illustrates the normalized ionospheric clutter PSD when the vertical ionospheric velocity

v_v varies from -15 m/s to 15 m/s. This figure indicates that the Doppler frequency of the clutter peaks directly responds to the ionospheric vertical motions. The negative velocity represents the ionosphere traveling upwards and away from the radar station, which introduces a negative Doppler shift, and vice versa. The band width of each spectrum and the intensity for the peak remain the same for different v_v.

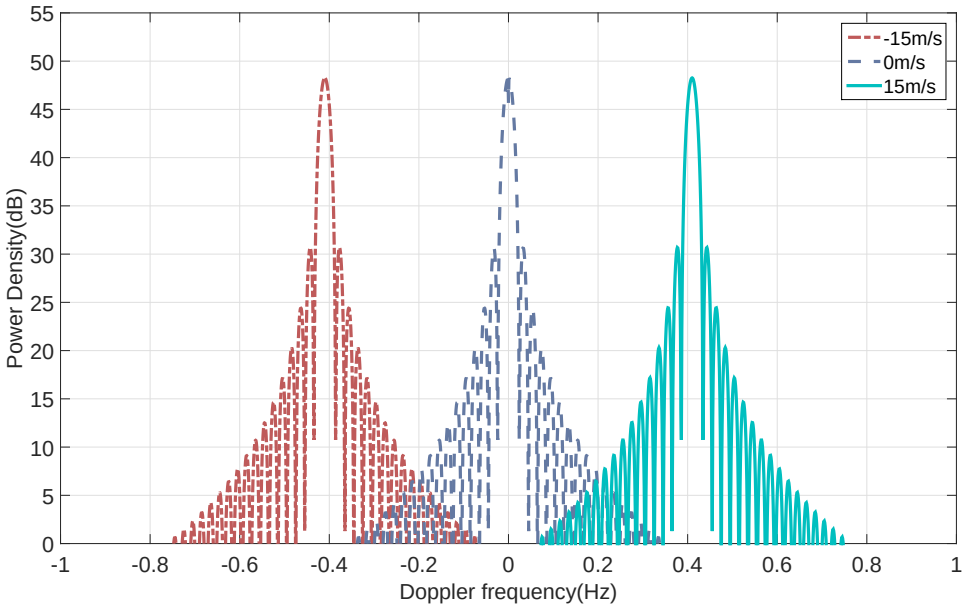

Figure 4.3: Normalized vertical ionospheric clutter PSD with different vertical ionospheric plasma drift velocities.

Then, the normalized ionospheric clutter PSD may be investigated for different radar operating frequencies reflected at the same height and for different reflection heights with the same operating frequency. Theoretically, a higher radar frequency corresponds to a higher electron density being required for total reflection, and the latter occurs at a greater height. This frequency is commonly referred to as the critical frequency at a given height.

The level of the electron density may change regularly with the intensity of sunlight and the corresponding virtual height of reflection can be obtained from an ionogram for a particular transmitted frequency. Two cases depicting critical frequencies associated with the E- and F-layers (150 km and 300 km, respectively) appear in Figure 4.4. At one point time with lower ionospheric electron density, the critical frequencies for E- and F-layers are 3.1 MHz and 4.1 MHz, respectively, and they become 4.1 MHz and 13 MHz at a different time at which the ionosphere has a higher electron density. It is observed that, for the same virtual height, the power density of the vertical ionospheric clutter with higher operating frequencies have higher peak values and broader bandwidths. On the other hand, for the same operating frequency of 4.1 MHz, the normalized peak power density of the F-layer reflection is higher than that for the E-layer, and the former bandwidth is broader than the latter. It is noted that, in practice, this value also depends on ionospheric absorption.

Finally, the simulated first-order received PSD of the vertical ionospheric clutter is compared with the spectrum of field data in Figure 1.3 (a), which was collected at Cape Race, Newfoundland on January 6, 2002 at 20:00 UTC. The radar frequency was 4.1 MHz and the pulsed width of the radar source was 50 μs. The apparent range was 230.8 km and the azimuth angle is 2.5°. The real spectrum involves contributions from both the vertical ionospheric propagation and the sea surface propagation. For vertical ionospheric propagation, the ionospheric motion and attenuation factors of the simulated spectrum are adjusted to fit the shape of the real power density spectrum. As shown in Figure 4.5, the dominant peak at "-0.31 Hz" is the first-order peak due to vertical reflection from the overhead ionosphere. The Doppler shift may be caused by the upwards ionospheric vertical motion with a speed of 12 m/s. The horizontal ionospheric drift velocity is determined to be 125 m/s in this case,

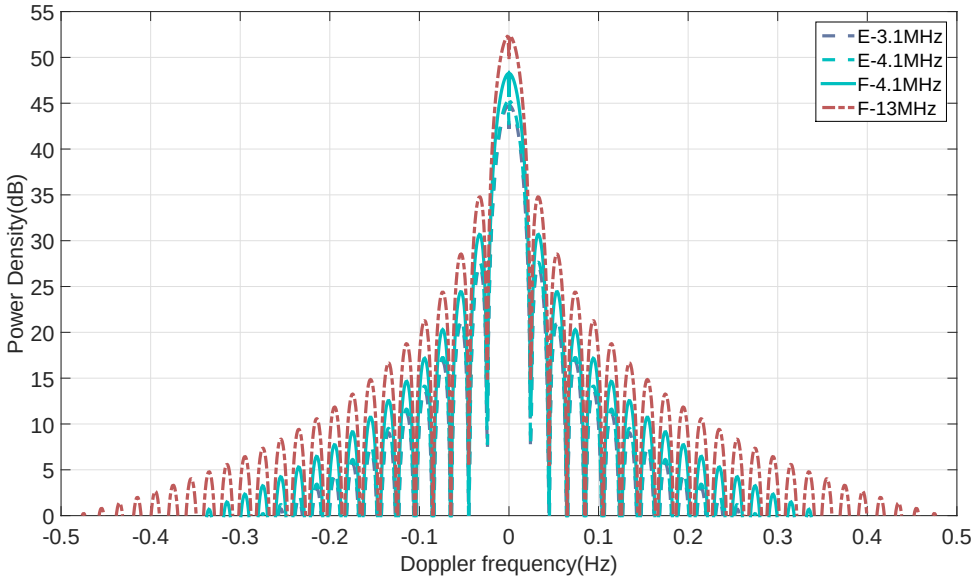

Figure 4.4: Normalized vertical ionospheric clutter PSD with different radar frequencies for reflections at 150 km (E layer) and 300 km (F layer).

which determines the bandwidth of the peak. The broadening of the first-order peak in the real spectrum may be due to the superposition of the sea clutter power.

4.3 The First-Order HF Radar Power Density Model for the Case of Mixed-Path Propagation with Bistatic Radar Configuration

4.3.1 Mixed-path geometry for bistatic HF radar

The geometry of the mixed-path propagation for the bistatic radar is shown in Figure 4.5. The X-Y plane indicates the mean sea level. The primary source transmitting antenna is

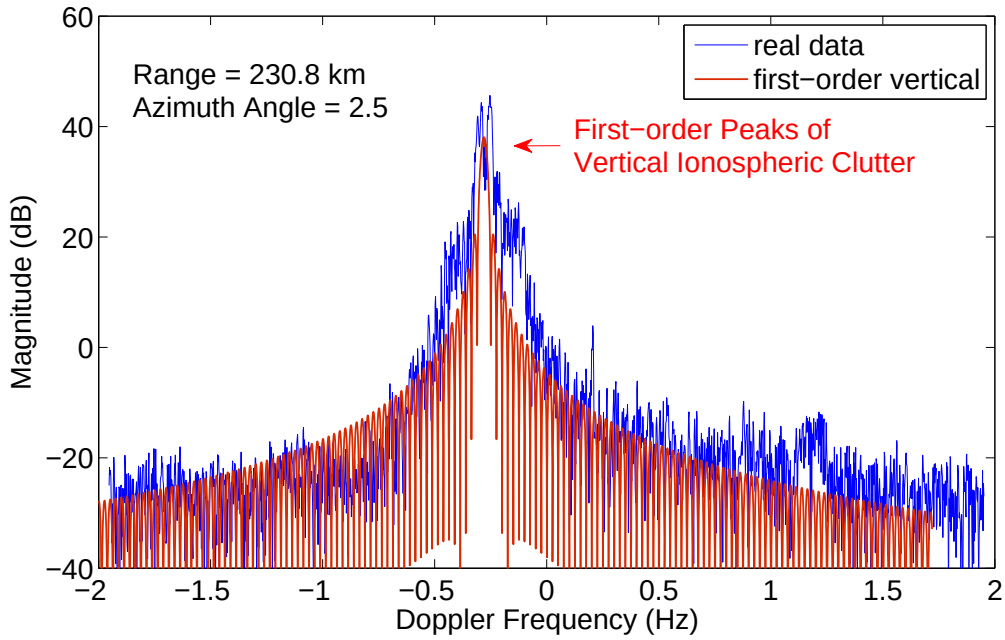

Figure 4.5: Comparison of the simulated PSD and the real spectrum for the vertical ionospheric clutter.

again taken to be a vertical dipole at the origin $(0, 0, 0^+)$ and the receiving antenna is at a distance ρ from the transmitter. As before, assuming the ionosphere to be a reflecting plane at a height of $H/2$, the image of the radar source is at a height of H. Note that θ_i is the reflection angle, R_1 is the range of free space propagation, ρ_1 is the projection of R_1 onto the X-Y plane, and ρ_2 is the range of surface propagation.

4.3.2 Derivation of the received electric field and power spectral density

The development of the mixed-path ionospheric clutter model for the bistatic HF radar incorporating a general vertical dipole source begins from the electric field equation found in

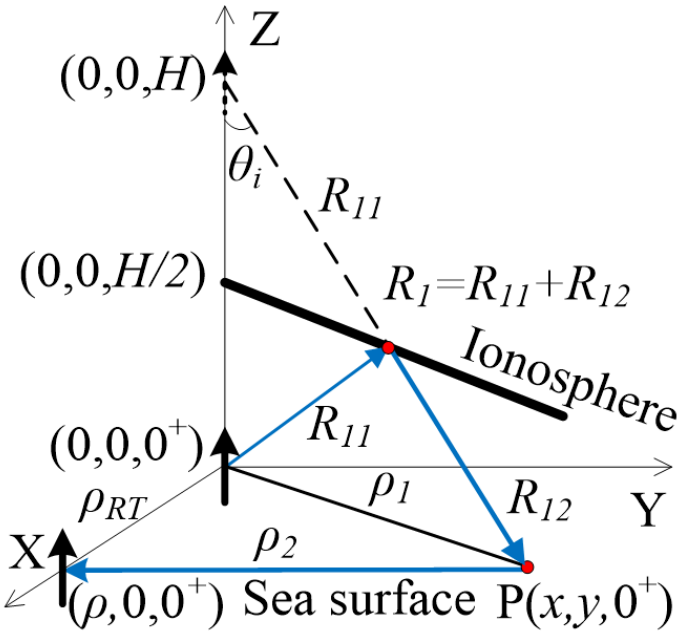

Figure 4.6: Geometry of the mixed-path propagation for the bistatic radar.

Eq. (1.13) [41]. According to previous investigations for HFSWR mixed-path propagation, the first-order radar received electric field equation may be represented as a convolution of the free-space propagation, in which the radiated electric field interacts with the rough surfaces of the ionosphere and the ocean, and the sea surface propagation with Sommerfeld attenuation.

Referring to Figure 4.5, the electric field at the receiving antenna $(\rho, 0, 0^+)$ when a single scatter occurs at a point $(x, y, 0^+)$ is given as

$$(E_{0n}^+)_1 \sim -kC_0[(\bigtriangledown\varepsilon \cdot \hat{\rho})R_i \sin\theta_i \frac{e^{-jkR_1}}{2\pi R_1}] * F(\rho_2)\frac{e^{-jk\rho_2}}{2\pi\rho_2}. \tag{4.16}$$

Substituting the general Fourier forms of the ocean surface profile and the IRC found in

equations (1.16) and (1.17), respectively, Eq. (4.16) may be written in integral form as

$$(E_{0n}^{+})_{1bi}(\rho_{RT},0) = -\,j\frac{kC_0}{(2\pi)^2}\sum_{\vec{K}_o}\sum_{\vec{K}_i} P_{\vec{K}_o}^{o} P_{\vec{K}_i}^{i} K_o \int\int_S \sin[\theta_i(\rho_1)] \\ (\hat{K_o}\cdot\hat{\rho}_1)F(\rho_2)\cdot\frac{e^{-jk(R_1+\rho_2)}}{R_1\rho_2} e^{j(\vec{K}_o+\vec{K}_i)\cdot\vec{\rho}_1} dxdy. \tag{4.17}$$

For a given transmitting time, the apparent range $2R_a = R_1 + \rho_2$ is fixed. Thus, the locus of the scattering points on the ocean surface may be obtained by the intersection of the X-Y plane and an ellipsoid, of which the foci are $(0, 0, H)$ and $(\rho_{RT}, 0, 0)$ and the major axis is $2R_a$. Based on the property of the ellipsoid that its intersection with a plane is always an ellipse, the locus of scattering points $(x,\ y)$ on the ocean surface may be derived from the geometric relationships

$$\begin{cases} x^2 + y^2 = R_1^2 - H^2, \\ (\rho - x)^2 + y^2 = \rho_2^2. \end{cases} \tag{4.18}$$

This locus may be determined and rewritten in the form

$$\frac{(x-x_0)^2}{(q\cosh\mu)^2} + \frac{y^2}{(q\sinh\mu)^2} = 1, \tag{4.19}$$

where

$$x_0 = \frac{\rho(4R_a^2 + H^2 - \rho^2)}{2(4R_a^2 - \rho^2)}, \qquad q = \frac{\rho(4R_a^2 - H^2)}{2(4R_a^2 - \rho^2)}, \\ q\cosh\mu = \frac{R_a(4R_a^2 - H^2 - \rho^2)}{4R_a^2 - \rho^2}, \quad q\sinh\mu = \frac{4R_a^2 - H^2 - \rho^2}{2\sqrt{(4R_a^2 - \rho^2)}}.$$

The positions of the two foci are $F_1 = (\frac{\rho H^2}{4R_a^2 - \rho^2}, 0)$ and $F_2 = (\rho, 0)$, and the range between F_1 and the scattering point is noted as ρ_1', as illustrated in Figure 4.6. Thus, x and y may be represented by the elliptic coordinates μ and δ as

$$x = q\cosh\mu\cos\delta + x_0, \\ y = q\sinh\mu\sin\delta. \tag{4.20}$$

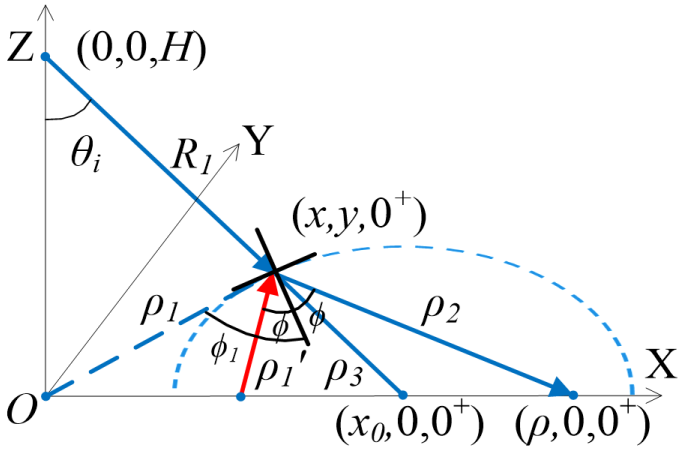

Figure 4.7: Locus of the scattering points on the ocean surface.

The x and y variables of the integrations in Eq. (4.17) are transformed to μ and δ, and the Jacobian of the transformation is $q^2(\cosh^2\mu - \cos^2\delta)$. Thus,

$$dxdy = q^2(\cosh^2\mu - \cos^2\delta)d\mu d\delta = \rho_1'\rho_2 d\mu d\delta.$$

Then, Eq. (4.17) becomes

$$\begin{aligned}(E_{0n}^{+})_{1bi} = &- j\frac{kC_0}{(2\pi)^2}\sum_{\vec{K}_o}\sum_{\vec{K}_i} P_{\vec{K}_o}^{o} P_{\vec{K}_i}^{i} K_o \int_{\mu} e^{-jk(R_1+\rho_2)} \\ &\int_{\delta} \sin^2[\theta_i(\rho_1)]\cos(\theta_O - \theta_1)F(\rho_2)e^{j\vec{K}_s\cdot\vec{\rho}_1}d\delta d\mu.\end{aligned} \tag{4.21}$$

The term $\left(\vec{K}_s \cdot \vec{\rho}_1\right)$ in the exponential of Eq. (4.21) is expanded with the aid of the elliptic coordinates in Eq. (4.20) as

$$\begin{aligned}\vec{K}_s \cdot \vec{\rho}_1 &= \rho_1 K_s \cos(\theta_s - \theta_1) \\ &= \rho_1 K_s(\cos\theta_s\cos\theta_1 + \sin\theta_s\sin\theta_1) \\ &= K_s[\cos\theta_s(q\cosh\mu\cos\delta + x_0) + \sin\theta_s q\sinh\mu\sin\delta] \\ &= K_s q(\cos\theta_s\cosh\mu\cos\delta + \sin\theta_s\sinh\mu\sin\delta) + \vec{x}_0\cdot\vec{K}_s.\end{aligned}$$

This leads to

$$(E_{0n}^{+})_{1bi} = -\,j\frac{kC_0}{(2\pi)^2}\sum_{\vec{K}_o}\sum_{\vec{K}_i} P^{o}_{\vec{K}_o} P^{i}_{\vec{K}_i} K_o \int_{\mu} e^{j\vec{x}_0\cdot\vec{K}_s} e^{-jk(R_1+\rho_2)} I_\delta d\mu, \tag{4.22}$$

where the δ-integral is written as

$$\begin{aligned} I_\delta = \int_\delta \frac{\rho_1'}{R_1}\sin[\theta_i(\rho_1)]\cos(\theta_O-\theta_1)F(\rho_2) \\ \cdot\, e^{jK_sq(\cos\theta_s\cosh\mu\cos\delta+\sin\theta_s\sinh\mu\sin\delta)}d\delta. \end{aligned} \tag{4.23}$$

This integral may be written in the form of

$$I_\delta = \int_\delta G(\delta)e^{jZ\Phi(\delta)}d\delta,$$

where $G(\delta) = \dfrac{\rho_1'}{R_1}\sin[\theta_i(\rho_1)]\cos(\theta_O-\theta_1)F(\rho_2)$, $Z = K_sq$, and $\Phi(\delta) = \cos\theta_s\cosh\mu\cos\delta + \sin\theta_s\sinh\mu\sin\delta$. When Z is a large real number and $G(\delta)$ varies much more slowly than $\Phi(\delta)$, the stationary phase technique may be applied to solve this integral. For bistatic operation, K_sq (i.e., Z) in the phase item of Eq. (4.23), may be shown to be on the order of thousands, is a large parameter, and the attenuation function $F(\rho_2)$ is a slowly varying quantity, especially for ocean surface with high conductivity [53]. Under these conditions, the δ-integral may be evaluated asymptotically by the stationary phase technique, the details of which are presented in Appendix C. The stationary phase point is solved as $\tan\delta = \tanh\mu\tan\theta_s$. It is straightforward to show that $\vec{K}_s$ is normal to the scattering ellipse at the stationary scattering point, and the angle between the foci of the ellipse as viewed from the scattering point is bisected by the ellipse normal at that point. Each portion of this bisection is seen in Figure 4.6 as angle ϕ, hereafter referred to as the bistatic angle. Furthermore, the angle between $\vec{\rho}_1$ and $\vec{K}_s$ is defined as ϕ_1 and the angle between the transmitter and receiver is defined as $\phi_b = \phi_1 + \phi$ for mixed-path propagation. Based on

the stationary phase theory technique in Appendix C, the δ-integral may be approximated as

$$I_\delta \approx \sqrt{2\pi}\frac{\rho_1'}{R_1}\sin[\theta_i(\rho_1)]\cos(\theta_O-\theta_1)F(\rho_2)\cdot\frac{e^{j\vec{\rho}_3\cdot\vec{K}_s}e^{-j\frac{\pi}{4}}}{\sqrt{\rho_s K_s\cos\phi}}, \tag{4.24}$$

where $\rho_s = \frac{\rho_1'+\rho_2}{2} = q\cosh\mu$, $\vec{\rho}_3$ is the vector from (x,y) to $(x_0,0)$ (as shown in Figure 4.6), ρ_1' can be written based on simple geometry as a function of the angle ϕ, as

$$\rho_1' = \rho_s + \frac{\sqrt{q^2-\sin^2\phi\rho_s^2}}{\cos\phi},$$

and $R_1 = 2R_a - 2\rho_s + \rho_1'$.

Substituting the solved I_δ into Eq. (4.22), it is seen that the first-order electric field may now be expressed as a single integral over μ. The integral variable is then changed to ρ_s with

$$d\rho_s = q\sinh\mu d\mu = q\sqrt{\cosh^2\mu-1}d\mu = \sqrt{\rho_s^2-q^2}d\mu.$$

Thus, Eq. (4.22) becomes

$$\begin{aligned}(E_{0n}^+)_{1bi} = &-j\frac{kC_0}{(2\pi)^2}\sum_{\vec{K}_o}\sum_{\vec{K}_i}P_{\vec{K}_o}^o P_{\vec{K}_i}^i K_o\int_{\rho_s}e^{j\vec{x}_0\cdot\vec{K}_s}e^{-jk(R_1+\rho_2)}\\ &\cdot\sqrt{2\pi}\frac{\rho_1'\sin[\theta_i(\rho_1)]\cos(\theta_O-\theta_1)F(\rho_2)}{R_1\sqrt{K_s\rho_s\cos\phi(\rho_s^2-q^2)}}e^{j\vec{\rho}_3\cdot\vec{K}_s}e^{-j\pi/4}d\rho_s.\end{aligned} \tag{4.25}$$

Following the procedure discussed in previous work [41], the ρ_s-integral may be further examined by incorporating a pulsed source current contained in C_0. Eq. (4.25) is first inversely Fourier transformed to the time-domain and the frequency-dependence terms kC_0 and $e^{-jk(R_1+\rho_2)}$ in Eq. (4.25) are similarly treated to give

$$\begin{aligned}\mathcal{F}^{-1}\left[kC_0\cdot e^{-jk(R_1+\rho_2)}\right] = &k_0^2\eta_0\Delta l I_0 e^{j\omega_0(t-\frac{R_1+\rho_2}{c})}\\ &\cdot\left[h(t-\frac{R_1+\rho_2}{c})-h(t-\frac{R_1+\rho_2}{c}-\tau_0)\right].\end{aligned} \tag{4.26}$$

The apparent range that corresponds to the received signal at time t is limited to the interval $ct - c\tau_0 < R_1 + \rho_2 < ct$. The range R_a and range resolution ΔR_a are defined in association with t as

$$R_{a0} = \frac{ct}{2} - \frac{c\tau_0}{4} \quad \text{and} \quad \Delta R_a = \frac{c\tau_0}{2}.$$

Accordingly, the surface range ρ_s and surface range resolution $\Delta\rho_s$ are defined as

$$\rho_{s0} = R_{a0}\left(\frac{4R_{a0}^2 - H^2 - \rho^2}{4R_{a0}^2 - \rho^2}\right) \quad \text{and} \quad \Delta\rho_s = \Delta R_a\left(\frac{4R_{a0}^2 - H^2 - \rho^2}{4R_{a0}^2 - \rho^2}\right),$$

respectively. Thus, the upper and lower limits of the ρ_s-integral may be written as $\rho_{s0} \pm \Delta\rho_s/2$ and Eq. (4.25) becomes

$$\begin{aligned}(E_{0n}^{+})_{1bi} = &- j\frac{k_0^2\eta_0\Delta l I_0}{(2\pi)^{3/2}} e^{j2k_0(R_{a0}+\Delta R_a/2)} e^{-j\pi/4} \sum_{\vec{K}_o}\sum_{\vec{K}_i} P_{\vec{K}_o}^{o} P_{\vec{K}_i}^{i} K_o \cos(\theta_O - \theta_1) \\ &\cdot \int_{\rho_{s0}-\frac{\Delta\rho_s}{2}}^{\rho_{s0}+\frac{\Delta\rho_s}{2}} \frac{\rho_1' \sin[\theta_i(\rho_1)] F(\rho_2)}{R_1\sqrt{K_s\rho_s\cos\phi(\rho_s^2 - q^2)}} e^{j\vec{\rho}_1\cdot\vec{K}_s} e^{-j2k_0R_a} d\rho_s,\end{aligned} \tag{4.27}$$

where it may be noted that $\vec{\rho}_1 = \vec{x}_0 + \vec{\rho}_3$.

An asymptotic form of this equation will be investigated to express the received electric field from a particular scattering patch on the ocean surface with the condition that $\rho_{s0} \gg \Delta\rho_s$. The phase term $(\vec{\rho}_1 \cdot \vec{K}_s - 2k_0R_a)$ is examined first. According to the ellipse geometry shown in Figure 4.7, ϕ and ϕ_1 are related to θ_s as

$$\begin{aligned}\cos\phi &= \sqrt{1 - \left(\frac{q}{\rho_s}\right)^2 \sin^2\theta_s}, \\ \cos\phi_1 &= \sqrt{1 - \left(\frac{x_N}{\rho_1}\right)^2 \sin^2\theta_s}.\end{aligned} \tag{4.28}$$

Defining $\rho_s' = \rho_s - \rho_{s0}$, the corresponding variation of ρ_1 is given as

$$\rho_1' = \rho_1 - \rho_{10} \approx \rho_s' \cos\phi_1.$$

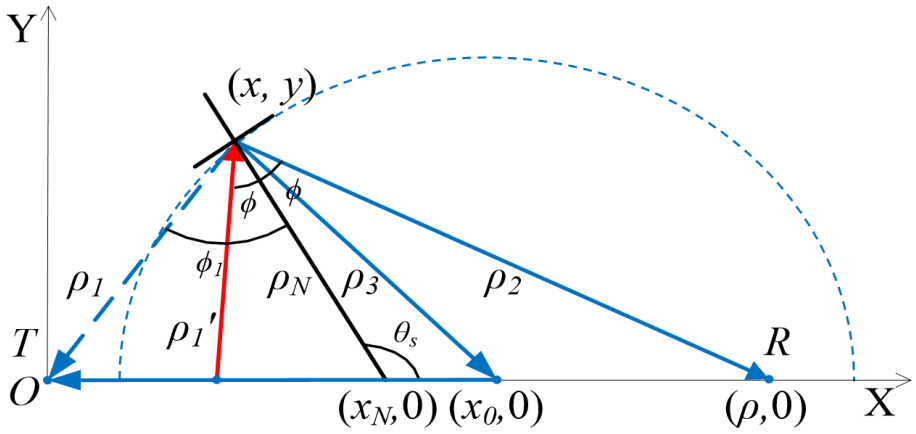

Figure 4.8: Ellipse geometry on X-Y plane.

Applying a binomial expansion, the first phase term may be written as

$$\begin{aligned}\vec{\rho}_1 \cdot \vec{K}_s =& \rho_1 K_s \cos\phi_1 \\ =& K_s \sqrt{(\rho_{10}+\rho_1')^2 - x_N^2 \sin^2\theta_s} \\ \approx& K_s \sqrt{\rho_{10}^2 - x_N^2 \sin^2\theta_s} + \frac{K_s}{\cos\phi_{10}}\rho_1' \\ \approx& K_s \rho_{10}\cos\phi_{10} + K_s \rho_s',\end{aligned} \tag{4.29}$$

where $\cos\phi_{10} = \sqrt{1-\left(\frac{x_N}{\rho_{10}}\right)^2 \sin^2\theta_s}$. With $R_a' = R_a - R_{a0} = \frac{R_1'+\rho_2'}{2}$, $R_1' = \rho_s' \cos\phi_{10}\sin\theta_i$, and $\rho_2' \approx \rho_s' \cos\phi_0$, the second phase term becomes

$$2k_0 R_a = 2k_0 R_a + k_0(\cos\phi_{10}\sin\theta_i + \cos\phi_0)\rho_s', \tag{4.30}$$

where $\cos\phi_0 = \sqrt{1-\left(\frac{q}{\rho_{s0}}\right)^2 \sin^2\theta_s}$.

Substituting Eq. (4.29) and (4.30) and changing the integral variable from ρ_s to ρ_s' in

Eq. (4.27), the electric field becomes

$$
\begin{aligned}
(E_{0n}^{+})_{1bi} = & -j\frac{k_0^2\eta_0\Delta l I_0}{(2\pi)^{3/2}}e^{j2k_0(R_{a0}+\Delta R_a/2)}e^{-j\pi/4}\sum_{\vec{K}_o}\sum_{\vec{K}_i}P^o_{\vec{K}_o}P^i_{\vec{K}_i} \\
& \cdot K_o\cos(\theta_O-\theta_1)\frac{\rho'_{10}\sin[\theta_i(\rho_{10})]F(\rho_{20})}{R_{10}\sqrt{K_s\rho_{s0}\cos\phi(\rho_{s0}^2-q_0^2)}} \\
& \cdot e^{jK_s\rho_{10}\cos\phi_{10}-2k_0R_{a0}}\int_{-\frac{\Delta\rho_s}{2}}^{\frac{\Delta\rho_s}{2}}e^{j\rho'_s[K_s-k_0(\sin\theta_i\cos\phi_{10}+\cos\phi_0)]}d\rho'_s.
\end{aligned}
\tag{4.31}
$$

The remaining ρ'_s-integral can be easily solved as

$$
\begin{aligned}
& \int_{-\frac{\Delta\rho_s}{2}}^{\frac{\Delta\rho_s}{2}}e^{j\rho'_s[K_s-k_0(\sin\theta_i\cos\phi_{10}+\cos\phi_0)]}d\rho'_s \\
=& \Delta\rho_s Sa\left\{\frac{\Delta\rho_s}{2}\left[K_s-k_0(\sin\theta_i\cos\phi_{10}+\cos\phi_0)\right]\right\}.
\end{aligned}
$$

Finally, the electric field of the mixed-path ionospheric clutter for the bistatic case becomes

$$
\begin{aligned}
(E_{0n}^{+})_{1bi} = & -j\frac{k_0^2\eta_0\Delta l I_0}{(2\pi)^{3/2}}e^{j2k_0(R_{a0}+\Delta R_a/2)}e^{-j\pi/4}\sum_{\vec{K}_o}\sum_{\vec{K}_i}P^o_{\vec{K}_o}P^i_{\vec{K}_i}K_o\cos(\theta_O-\theta_1) \\
& \cdot\frac{\rho'_{10}\sin[\theta_i(\rho_{10})]F(\rho_{20})}{R_{10}\sqrt{K_s\rho_{s0}\cos\phi(\rho_{s0}^2-q_0^2)}}e^{jK_s\rho_{10}\cos\phi_{10}-2k_0R_{a0}} \\
& \cdot\Delta\rho_s Sa\left\{\frac{\Delta\rho_s}{2}\left[K_s-k_0(\sin\theta_i\cos\phi_{10}+\cos\phi_0)\right]\right\}.
\end{aligned}
\tag{4.32}
$$

The sampling function in Eq. (4.32) has its principle maximum at

$$
K_s = k_0(\sin\theta_i\cos\phi_{10}+\cos\phi_0), \tag{4.33}
$$

for which condition the received electric field achieves its maximum value. This conclusion may also be drawn from the Bragg scattering analysis. The Bragg condition dictates that the energy scattered off the one wave is precisely in phase with that scattered from a successive wave, and this resonance amplifies the signal at the receiver. In the first-order case, the

difference in the travelling path of the scattered signals is a whole wavelength [80]. As shown in Figure 4.8, the total effect produced by the scattering of the radio waves from the ionospheric irregularities and the ocean waves may be considered as a scattering from the vector sum $\vec{K}_s = \vec{K}_i + \vec{K}_o$, recalling that $\vec{K}_i$ and $\vec{K}_o$ are the wavenumber of the ionospheric irregularities and the ocean waves, respectively. The path differences of R_1 and ρ_2 are denoted as $\Delta\lambda_1$ and $\Delta\lambda_2$, and the angles ϕ_1 and ϕ are defined in Figure 4.6. The Bragg scattering condition is given as

$$\begin{aligned}\lambda_0 &= \Delta\lambda_1 + \Delta\lambda_2 \\ &= \lambda_s \cos\phi_1 \sin\theta_i + \lambda_s \cos\phi,\end{aligned}$$

which is equivalent to Eq. (4.33).

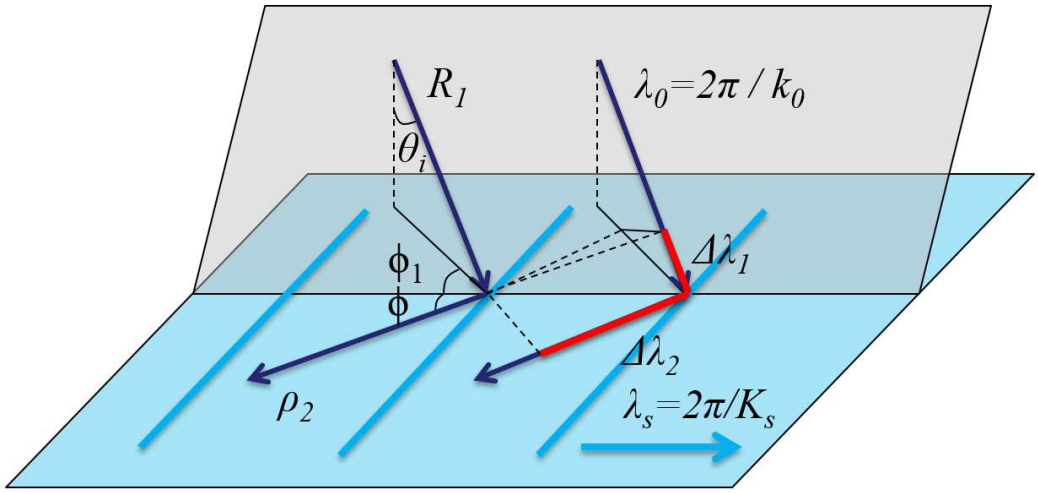

Figure 4.9: Illustration of the Bragg scattering of mixed-path propagation for bistatic case.

It is now assumed that data from successive pulses are collected. In this case, the ocean and ionosphere surfaces may be considered to have slow time variations. Thus, their representations are modified to the spatial and temporal Fourier transforms. The received

first-order PSD may be obtained by the Fourier transform of the field autocorrelation as

$$\begin{aligned}
P_{1bi}(\omega_d) =& \mathcal{F}\left[\frac{A_r}{2\eta_0}\langle E_{1bi}(t+\tau)E^*_{ibi}(t)\rangle\right] \\
=& \frac{A_r}{2\eta_0}\frac{(k_0^2\eta_0\Delta l I_0)^2}{(2\pi)^2}\frac{\rho_{10}'^2\sin^2(\theta_i)F(\rho_{20})^2(\Delta\rho_s)^2}{R_{10}^2\rho_{s0}\cos\phi(\rho_{s0}^2-q_0^2)} \\
& \cdot \int_{\vec{K}_o}\int_{\vec{K}_i}\int_{\omega_o}\int_{\omega_i}\frac{K_o^2}{K_s}\cos^2(\theta_o-\theta_1) \\
& \cdot Sa^2\left\{\frac{\Delta\rho_s}{2}\left[K_s - k_0(\sin\theta_i\cos\phi_{10}+\cos\phi_0)\right]\right\} \\
& \cdot S_o(\vec{K}_o,\omega_o)S_i(\vec{K}_i,\omega_i)\delta[\omega-(\omega_o+\omega_i)]d\vec{K}_o d\vec{K}_i d\omega_o d\omega_i.
\end{aligned} \tag{4.34}$$

4.3.3 Simulation and analysis

Here, numerical simulations will be conducted to investigate the PSD of the mixed-path ionospheric clutter for the bistatic configuration. The specific models of the ocean surface and the ionospheric irregularities are incorporated into the received power density equation, and the integral is evaluated following similar steps discussed in Appendix A for the monostatic case. Eq. (4.34) may be reduced to

$$\begin{aligned}
P_{1bi}(\omega_d) =& \frac{A_r}{2\eta_0}\frac{(k_0^2\eta_0\Delta l I_0)^2}{(2\pi)^2}\frac{\rho_{10}'^2\sin^2(\theta_i)F(\rho_{20})^2(\Delta\rho_s)^2}{R_{10}^2\rho_{s0}(\rho_{s0}^2-q_0^2)}\frac{2\pi}{\Delta\rho_s} \\
& \frac{1}{2}\frac{2}{\sqrt{g}}\int_{\phi_s}\Psi_{bi}(\omega_s,\phi_s)d\phi_s,
\end{aligned} \tag{4.35}$$

where $\Psi_{bi}(\omega_d,\phi_s) = \Psi_{1bi}(\omega_d,\phi_s) + \Psi_{2bi}(\omega_d,\phi_s)$ with

$$\begin{aligned}
\Psi_1(\omega_d,\phi_s) =& \int_{K_i} K_i K_o^{5/2}\frac{\cos^2(\theta_o-\theta_1)}{\cos(\theta_o-\theta_s)}\left|\frac{\vec{K}_o\cdot\vec{K}_s}{K_s}\right| S_o(K_o,\phi_o)S_i(K_i) \\
& \cdot \left|\frac{K_i\cos(\phi_i-\phi_s)-K_s}{K_iK_s\sin(\phi_i-\phi_s)-K_o\frac{dK_o}{d\phi_i}}\right| dK_i,
\end{aligned} \quad \text{for m=1,}$$

and

$$\Psi_2(\omega_d,\phi_s) = \int_{K_i} K_i K_o^{5/2} \frac{\cos^2(\theta_o-\theta_1)}{\cos(\theta_o-\theta_s)} \left|\frac{\vec{K}_o\cdot\vec{K}_s}{K_s}\right| S_o(K_o,\phi_o+\pi) S_i(K_i) \cdot \left|\frac{K_i\cos(\phi_i-\phi_s)-K_s}{K_i K_s \sin(\phi_i-\phi_s)+K_o\frac{dK_o}{d\phi_i}}\right| dK_i, \quad \text{for m=-1.}$$

The simulated PSD for the bistatic case is also normalized by the average first-order ocean clutter peak power density. The parameters of the radar system, bistatic configurations, and ionosphere and sea conditions are given in Table 4.2.

Table 4.2: Main parameters involved in the simulations

radar operating frequency (f_0)	4.1 MHz
radar pulse length (τ_0)	50 μs
distance between transmitter and receiver (ρ)	100 km
bistatic angle (ϕ)	30°
ionosphere height ($H/2$)	300 km
typical ionosphere speed (v_0)	100 m/s
ionosphere direction (θ_{ih})	90°
wind speed (U)	10 m/s
wind direction (θ)	0°

The bistatic normalized PSD is compared with that of the monostatic configuration looking at the same scattering patch (see Figure 4.9). It is assumed that a transmitter and receiver are at one radar site (monostatic) and a receiver at another (bistatic). The direction

of the ellipse normal for the bistatic case is taken to be perpendicular to the wind direction. For a particular scattering point, this produces Bragg peaks of equal magnitudes. Since, in the example, the bistatic angle is 30° and the direction of the normal to the scattering ellipse is 90° in the bistatic case, the apparent range of $(R_1 + \rho_2)/2$ is calculated to be 350 km. Thus, the direction of ρ_1 in Figure 4.7 is given as 76° (noting that in this case, the transmitter is located between of foci of the scattering ellipse), which is set to be the look direction of the monostatic radar. In the monostatic case, the surface wind has more of a outward component along the look direction for the monostatic case. This enhances the peak value in the negative Doppler region. This also indicates that simultaneous bistatic and monostatic operation can provide surface wind direction information. Of course, due to the bistatic angle, the bistatic Doppler frequencies of the Bragg peaks are slightly smaller than those of the monostatic case .

Simulation results for the first-order received PSD of the mixed-path propagation for various angles are depicted in Figure 4.10. Setting the direction of the ellipse normal as 90°, the corresponding apparent ranges for bistatic angles of 15°, 30° and 45° are 410 km, 350 km and 335 km, respectively. The Doppler frequencies of the peaks become smaller for larger bistatic angle, since the Bragg peaks directly depend on the cosine of the bistatic angle. The normalized power density is roughly 35 dB relative to the first-order ocean clutter average peak power density, and the bandwidth remains the same as 0.2 Hz.

Finally, keeping the bistatic angle as 30° and the direction of the ellipse normal as 90°, the normalized PSD is investigated by changing the distance between transmitters and receivers. The apparent ranges may vary correspondingly. It is observed from Figure 4.11 that the overall shapes remain unchanged, and major peak positions of the Doppler spectrum

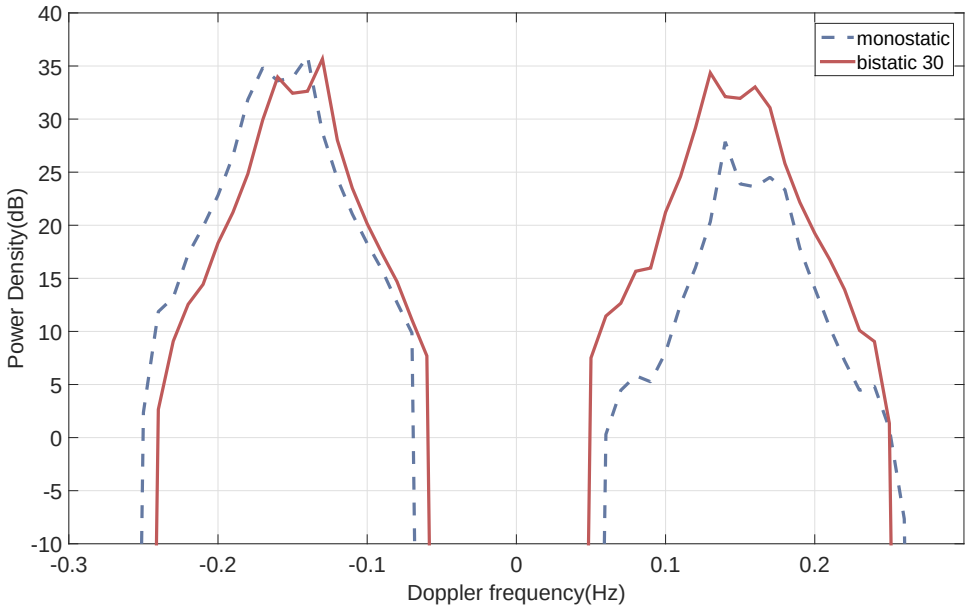

Figure 4.10: First-order PSD for bistatic and monostatic HF radar.

shift slightly, an effect which may be caused by the variation of the incidence angle. The normalized peak power density are also about 35 dB. In reality, this value may be modified by considering the radar system parameters and environmental absorption factors.

4.4 General Chapter Summary

In this Chapter the ionospheric clutter power spectral density (PSD) model has been derived for the cases of vertical ionospheric clutter for monostatic radar and first-order mixed-path ionospheric clutter for bistatic radar.

For the vertical ionospheric clutter case, the derivation started from the received electric field of radio waves travelling vertically upwards and being reflected by the ionosphere to the receivers based on the image theory. The next key steps were to incorporate a pulsed

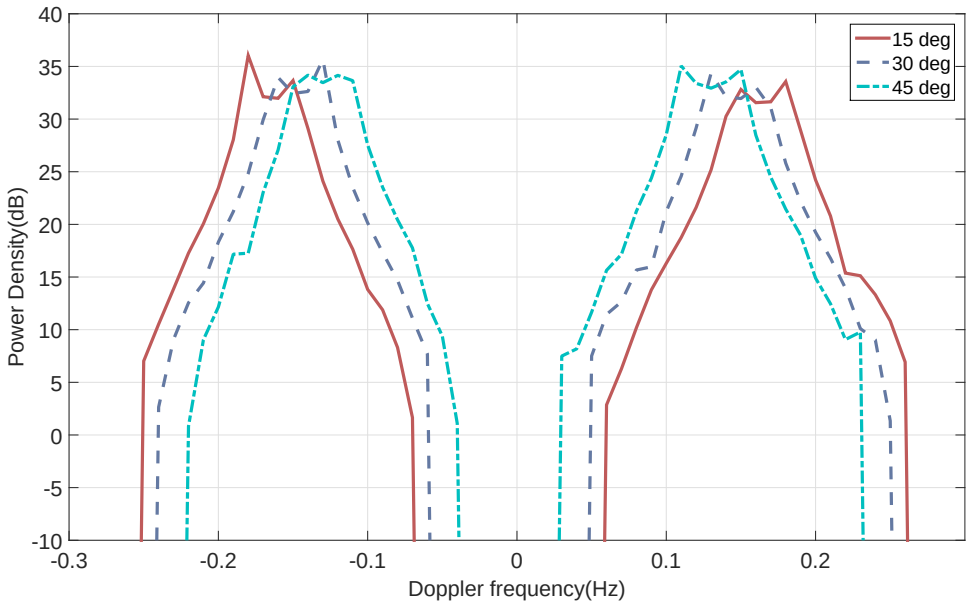

Figure 4.11: First-order PSD for different bistatic angle.

source current into the field equation and apply a simplified practical model of the electron density irregularities into the spectral density of the IRC. Finally, the PSD of the vertical ionospheric clutter for the monostatic case was simulated for varying vertical and horizontal ionospheric plasma drift velocities and radio waves of different radar operating frequency reflected from different ionospheric layers. Simulations illustrate that the vertical ionospheric clutter was shaped as an impulse with oscillations and the peak power density of the ionospheric clutter exceeds that of the average first-order ocean clutter peak by about 45 dB. Of course, the peak value and the Doppler spread of the power spectral density will be determined by the particular radar operation parameters and ionosphere conditions.

Next, a first-order ionospheric clutter PSD model for mixed-path propagation has been extended to the case of bistatic HF radar. This model includes the scattering processes from both the ionosphere and the ocean surface for a particular bistatic angle. With the

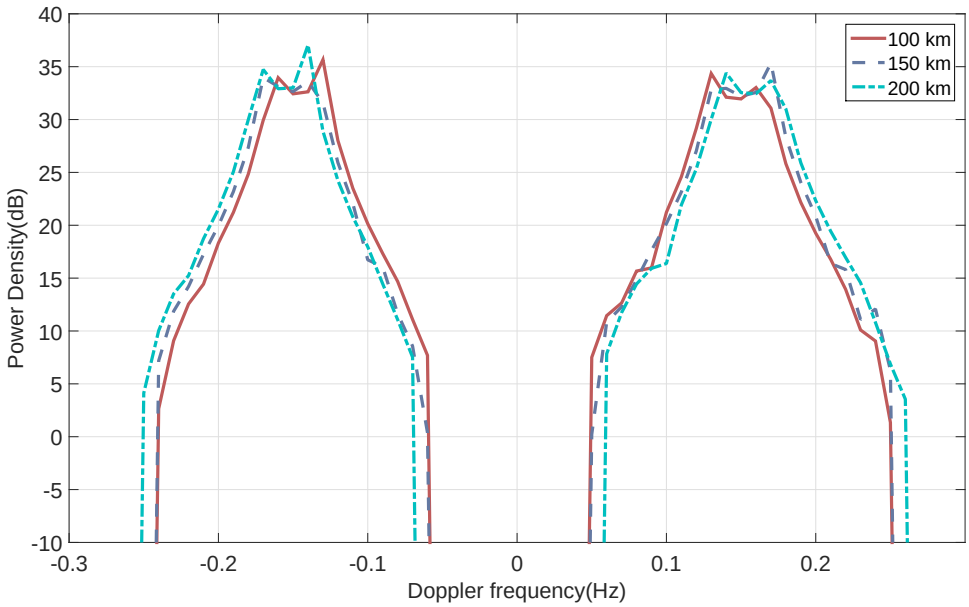

Figure 4.12: First-order PSD for different distance between transmitters and receivers.

aid of the elliptical coordinates, the form of the electric field was derived. Simulations of the normalized PSD were compared with the monostatic case and then conducted for a variety of bistatic features including bistatic angle and the distance between transmitters and receivers. Results showed that simultaneous operation of the radar system in the monostatic and bistatic modes may provide adequate information of surface winds.

Chapter 5

The First-Order HF Radar Power Density Model for Monostatic Mixed-Path Propagation with a Frequency-Modulated Continuous Waveform Source

5.1 Introduction

In a pulsed radar system, for a given operating frequency, the maximum range of detection is determined by the total transmitted energy, and long-duration pulses should be used to achieve high energy; on the other hand, shorter pulses would result in better range resolu-

tion. Thus, these divergent needs require the radar to transmit high peak power in narrow pulses for good operating performance [81]. Fortunately, frequency-modulated continuous wave (FMCW) systems may be designed with sufficient bandwidth to provide good maximum range and range resolution with power levels significantly smaller than the typical peak power in pulsed systems [82], [83]. In recent years, low power FMCW HF radar systems have become popular in ocean remote sensing applications. This fact provides the motivation for revisiting the work for the mixed-path case with monostatic radar [84].

This chapter presents a continuation of the development of the mixed-path propagation models, which have been investigated for first- and second-order power spectral density (PSD) with a pulsed dipole [41, 72]. Here, the analysis is extended to the first-order HF radar clutter power density for mixed-path propagation incorporating an FMCW source. Background information for mixed-path propagation and the FMCW radar source is introduced in Section 5.2. In Section 5.3, the received field equation incorporating a general vertical dipole source is modified for an FMCW source. Then, the corresponding first-order received PSD is derived. In Section 5.4, simulations are conducted for a variety of ionospheric conditions, and a comparison is made with results from a pulsed system.

5.2 Frequency-Modulated Continuous Waveform

The time-domain expression for the FMCW transmitting antenna current waveform within one sweep interval is given as

$$i_T(t) = I_0 \cos[2\pi(f_0 + \frac{\alpha t}{2})t], \quad -\frac{T_r}{2} \leq t < \frac{T_r}{2}, \tag{5.1}$$

where I_0 is the peak current, f_0 is the centre frequency, α is the sweep rate, and T_r is the sweep interval. The sweep frequency bandwidth B is given as $B = \alpha T_r$. This current waveform may also be expressed in the complex exponential form as

$$i_T(t) = I_0 e^{j(\omega_0 t + \alpha \pi t^2)} \left\{ h\left[t + \frac{T_r}{2}\right] - h\left[t - \frac{T_r}{2}\right] \right\}, \tag{5.2}$$

where h is the Heaviside function. A typical example of a linear FMCW signal and its frequency-time plot are shown in Figure 5.1. For the purpose of illustration, this upsweep waveform is chosen to have a center frequency of $f_0 = 20$ Hz and a sweep bandwidth $B = 20$ Hz. The FMCW signal is a periodic repetition version of the swept signal with finite sweep interval $T_r = 1$ s.

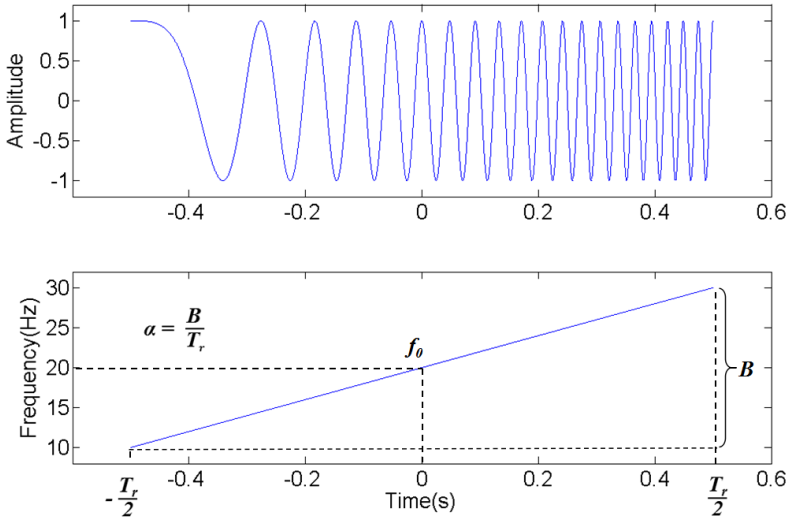

Figure 5.1: Example of FMCW signal and its frequency-time plot.

For the upsweep case, the basic method to measuring the range of one target is indicated in Figure 5.2. After transmission, the received waveform is both delayed in time and shifted in Doppler [82]. Assuming one simple target at the range R_0 at time $t = 0$ traveling at a

constant velocity v with respect to the radar, its range as a function of time is

$$R(t) = R_0 + vt.$$

The received signal $i_R(t)$ is a replica of the transmitted signal, but multiplied in amplitude by an attenuation factor A and delayed in time by a factor $t_d = 2R(t)/c$ and may be cast as

$$i_R(t) = Ai_T(t) = A\cos\left[2\pi\left(f_0 + \frac{\alpha(t-t_d)}{2}\right)(t-t_d)\right].$$

In order to extract the target information, the received signal is mixed with the transmitted signal. After appropriate filtering and approximation, the mixed signal may be represented mathematically by subtracting the phase $\phi_T(t)$ from the received phase $\phi_T(t-t_d)$ as

$$\begin{aligned} i_M(t) =& A\cos[\phi_T(t-t_d) - \phi_T(t)] \\ \approx& A\cos\left[2\pi\left(f_0\frac{2R_0}{c} + \frac{2\alpha R_0^2}{c^2}\right) - 2\pi\left(\frac{2v}{c}f_0 + \alpha\frac{2R_0}{c}\right)t\right]. \end{aligned} \tag{5.3}$$

The frequency of the mixed signal is given as

$$f_M = \frac{1}{2\pi}\frac{d}{dt}\phi_M(t) = \frac{2v}{c}f_0 + \alpha\frac{2R_0}{c}. \tag{5.4}$$

It is seen that the frequency offset is due to both the target velocity and the range of the target.

It must be emphasized that the analysis above is for the one-target case. For the ocean surface, which consists of a great number of waves travelling in different directions with different speeds, the radio waves may be reflected back to the receiver by any of these. The Doppler spectrum produced by scattering from this complex surface is used to extract the ocean information.

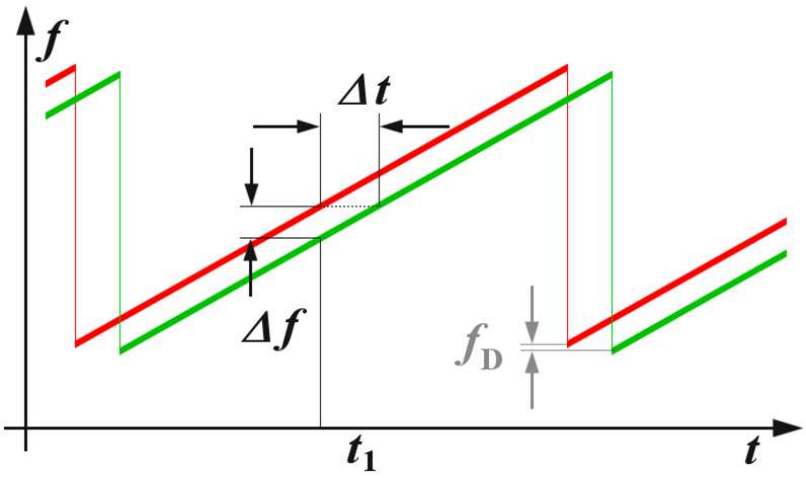

Figure 5.2: Transmitted and received waveforms for one target case.

5.3 Derivation of the Received Electric Field and Power Spectral Density

The development of the scattered electric field equations from the ionosphere-ocean path incorporating a general vertical dipole source is discussed in Section 1.2.3. For the backscatter case, this general first-order electric field in the frequency domain (from Eq. (2.4) in [40]) is given by

$$(E_{0n}^{+})_1 \sim -kC_0 \left\{ \left[(\nabla\varepsilon \cdot \hat{\rho}) R_i \sin\theta_i \frac{e^{-jkR}}{2\pi R} \right] \overset{xy}{*} F(\rho) \frac{e^{-jk\rho}}{2\pi\rho} \right\}. \tag{5.5}$$

Recalling that the ocean surface profile $\varepsilon(x,y)$ and the IRC $R_i(x,y)$ are considered to vary randomly with position and be represented by general Fourier forms, the integral form of Eq. (5.5) may be written as

$$\begin{aligned}(E_{0n}^{+})_1 = &- j\frac{kC_0}{(2\pi)^{3/2}} e^{-j\pi/4} \sum_{\vec{K}_o} \sum_{\vec{K}_i} P^{o}_{\vec{K}_o} P^{i}_{\vec{K}_i} \frac{\vec{K}_o \cdot \vec{K}_s}{K_s^{3/2}} \\ &\int_{\rho} \frac{F(\rho)}{R\sqrt{\rho}} \sin[\theta_i(\rho)] \cdot e^{jK_s\rho} e^{-jk(\rho+R)} d\rho.\end{aligned} \tag{5.6}$$

In order to incorporate a time-domain transmitted signal consisting of an FMCW waveform from a dipole antenna, Eq. (5.6) may be inversely Fourier transformed and is then given by

$$
\begin{aligned}
(E_{0n}^{+})_1(t) \sim & -j\frac{1}{(2\pi)^{3/2}}e^{-j\pi/4}\sum_{\vec{K}_o}\sum_{\vec{K}_i}P^{o}_{\vec{K}_o}P^{i}_{\vec{K}_i}\frac{\vec{K}_o\cdot\vec{K}_s}{K_s^{3/2}} \\
& \int_{\rho}\frac{F(\rho)}{R\sqrt{\rho}}\sin[\theta_i(\rho)]e^{jK_s\rho}\cdot[\mathcal{F}_t^{-1}(kC_0)*\delta(t-\frac{\rho+R}{c})]d\rho.
\end{aligned}
\tag{5.7}
$$

The inverse Fourier transform of (kC_0) is given by

$$
\mathcal{F}^{-1}\left[\frac{\eta_0\Delta l}{c^2}\omega^2 I(\omega)\right](t) = -\frac{\eta_0\Delta l}{c^2}\frac{\partial^2 i(t)}{\partial t^2}, \tag{5.8}
$$

where the second-order derivative of $i(t)$ with the FMCW excitation is

$$
\begin{aligned}
\frac{\partial^2 i(t)}{\partial t^2} = & -I_0(\omega_0^2+4\pi\alpha\omega_0 t+4\pi^2\alpha^2t^2-j2\pi\alpha)e^{j(\omega_0 t+\alpha\pi t^2)} \\
& \left\{h\left[t+\frac{T_r}{2}\right]-h\left[t-\frac{T_r}{2}\right]\right\} \\
\approx & -I_0\omega_0^2 e^{j(\omega_0 t+\alpha\pi t^2)}\left\{h\left[t+\frac{T_r}{2}\right]-h\left[t-\frac{T_r}{2}\right]\right\}.
\end{aligned}
\tag{5.9}
$$

The approximation is permissible because $|2\pi\alpha t| < 2\pi B \ll \omega_0$ for typical HF radar operating parameters. The convolution of Eq. (5.8) with $\delta\left(t-\frac{\rho+R}{c}\right)$ produces a shift of $(\rho+R)/c$ in the time variable t. Then the phase in Eq. (5.9) becomes

$$
\begin{aligned}
& \omega_0[t-(\rho+R)/c]+\alpha\pi[t-(\rho+R)/c]^2 \\
=& \omega_0 t+\alpha\pi t^2-k_0(\rho+R)-\pi\alpha\left[(\frac{\rho+R}{c})^2-2(\frac{\rho+R}{c})t\right].
\end{aligned}
$$

Up to this point, the electric field equation is developed for a sweep time interval T_r. Within one sweep, the ocean and ionosphere surfaces are illuminated by the radar signals and the surfaces are assumed to be fixed during this transmitting time. In order to emphasize this, the time variable of the electric field within a sweep interval T_r is renamed as t_r and

the time variable t will be retained when the time-varying ocean and ionosphere surfaces are introduced.

Thus, from Eq. (5.7), the first-order temporal field equation for the FMCW waveform in a sweep interval is

$$\begin{aligned}
&(E_0)_{1FM}(t_r) = \\
&\frac{-jI_0\eta_0\Delta l k_0^2}{(2\pi)^{3/2}} e^{-j\pi/4} \sum_{\vec{K}_o} \sum_{\vec{K}_i} P^o_{\vec{K}_o} P^i_{\vec{K}_i} \frac{\vec{K}_o \cdot \vec{K}_s}{K_s^{3/2}} \int_\rho \frac{F(\rho)}{R\sqrt{\rho}} \\
&\cdot \sin[\theta_i(\rho)] e^{j(\omega_0 t_r + \alpha\pi t_r^2)} e^{-jk_0(\rho+R)} e^{j\pi\alpha\left[(\frac{\rho+R}{c})^2 - 2(\frac{\rho+R}{c})t_r\right]} \\
&\cdot e^{jK_s\rho} \times \left\{ h\left[t_r - \frac{\rho+R}{c} + \frac{T_r}{2}\right] - h\left[t_r - \frac{\rho+R}{c} - \frac{T_r}{2}\right] \right\} d\rho.
\end{aligned} \tag{5.10}$$

In order to focus on the information generated during the transmission process, a demodulation of the received field is implemented before further processing. This is the typical "preprocess" which involves coherently mixing the acquired signal with the original signal and low-pass filtering the outcome to remove higher frequency components [85]. Applying the transformations found in Appendix D, an ideal demodulation shows that the original exponential factor $e^{j(\omega_0 t_r + \alpha\pi t_r^2)}$ will be eliminated, the phase term will be replaced by its complex conjugate, and the other factors remain the same as in Eq. (5.10). After demodulation, Eq. (5.10) is given as

$$\begin{aligned}
(E_0)^D_{1FM}(t_r) &= \frac{-jI_0\eta_0\Delta l k_0^2}{(2\pi)^{3/2}} e^{j\pi/4} \sum_{\vec{K}_o} \sum_{\vec{K}_i} P^o_{\vec{K}_o} P^i_{\vec{K}_i} \frac{\vec{K}_o \cdot \vec{K}_s}{K_s^{3/2}} \\
&\cdot \int_\rho \frac{F(\rho)}{R\sqrt{\rho}} \sin[\theta_i(\rho)] e^{-jK_s\rho} e^{jk_0(\rho+R)} e^{-j\pi\alpha(\frac{\rho+R}{c})^2} e^{j2\pi\alpha(\frac{\rho+R}{c})t_r} \\
&\times \left\{ h\left[t_r - \frac{\rho+R}{c} + \frac{T_r}{2}\right] - h\left[t_r - \frac{\rho+R}{c} - \frac{T_r}{2}\right] \right\} d\rho,
\end{aligned} \tag{5.11}$$

where the superscript D indicates demodulation.

As mentioned above, when the FM signal is scattered over the patch and received, the range information will be brought back with a time delay. For a certain time delay, there will be a corresponding frequency offset as depicted in Figure 5.2. This indicates that the frequency distribution of the demodulated electric field would indicate the range distribution of the scattering 'point' on the ocean surface. Thus, the next step of the process is to Fourier transform the electric field with respect to t_r to obtain the so-called "range transform". In Eq. (5.11), only the last two terms are functions of t_r and their Fourier transform is given by

$$\begin{aligned}
&\mathcal{F}\left[e^{j2\pi\alpha(\frac{\rho+R}{c})t_r}\times\left\{h\left[t-\frac{\rho+R}{c}+\frac{T_r}{2}\right]-h\left[t-\frac{\rho+R}{c}-\frac{T_r}{2}\right]\right\}\right]\\
=&\int_{\frac{\rho+R}{c}-\frac{T_r}{2}}^{\frac{\rho+R}{c}+\frac{T_r}{2}} e^{j2\pi\alpha(\frac{\rho+R}{c})t_r}e^{-j\omega t_r}dt_r \qquad (5.12)\\
=&T_r e^{j(\frac{2\pi\alpha(\rho+R)}{c}-\omega)\frac{\rho+R}{c}}Sa\left[\frac{T_r}{2}(\omega_r-\frac{2\pi\alpha(\rho+R)}{c})\right].
\end{aligned}$$

Thus, the range transform corresponding to the time-domain expression in Eq. (5.12) is given as

$$\begin{aligned}
(E_0)^D_{1FM}(\omega_r)=&\frac{-jI_0\eta_0\Delta l k_0^2T_r}{(2\pi)^{3/2}}e^{j\pi/4}\sum_{\vec{K}_o}\sum_{\vec{K}_i}P^o_{\vec{K}_o}P^i_{\vec{K}_i}\frac{\vec{K}_o\cdot\vec{K}_s}{K_s^{3/2}}\\
&\int_\rho\frac{F(\rho)}{R\sqrt{\rho}}\sin[\theta_i(\rho)]e^{-jK_s\rho}e^{jk_0(\rho+R)}e^{j\pi\alpha(\frac{\rho+R}{c})^2} \qquad (5.13)\\
&e^{j(\frac{2\pi\alpha(\rho+R)}{c}-\omega_r)(\frac{\rho+R}{c})}Sa\left[\frac{T_r}{2}\left(\omega_r-\frac{2\pi\alpha(\rho+R)}{c}\right)\right]d\rho.
\end{aligned}$$

For a given frequency, ω_r, the corresponding travel range is defined as $2\rho_r$, where

$$\rho_r=\frac{c\Delta t}{2}=\frac{c\omega_r}{4\pi\alpha}=\frac{\rho_0+R_0}{2},$$

and where Δt is the total travel time of the radio waves along the ionosphere-ocean path. As illustrated in Figure 5.3, ρ_0 represents the range between the radar and the centre point

of the scattering patch on the ocean surface, and R_0 is the range of the skywave from the transmitting radar to this point. Then, the argument of the sampling function in Eq. (5.13) can be rewritten as

$$\frac{T_r}{2}\left(\omega_r - \frac{2\pi\alpha(\rho+R)}{c}\right) = \frac{2\pi B}{c}\left(\frac{\rho_0+R_0}{2} - \frac{\rho+R}{2}\right) = k_B\left(\frac{\rho_0+R_0}{2} - \frac{\rho+R}{2}\right),$$

where $k_B = \frac{2\pi B}{c}$. The relationship between ρ_0 and R_0 is $R_0 = \sqrt{\rho_0^2 + H^2}$. Defining $\rho = \rho_0 + \rho'$ and $\sin\theta_0 = \rho_0/R_0$, the general skywave range R to a position on the ocean scattering patch is approximated as

$$R = \sqrt{(\rho_0+\rho')^2 + H^2} \approx R_0\sqrt{1 + \frac{2\rho'\rho_0}{R_0^2}} \approx R_0 + \sin\theta_0\rho'.$$

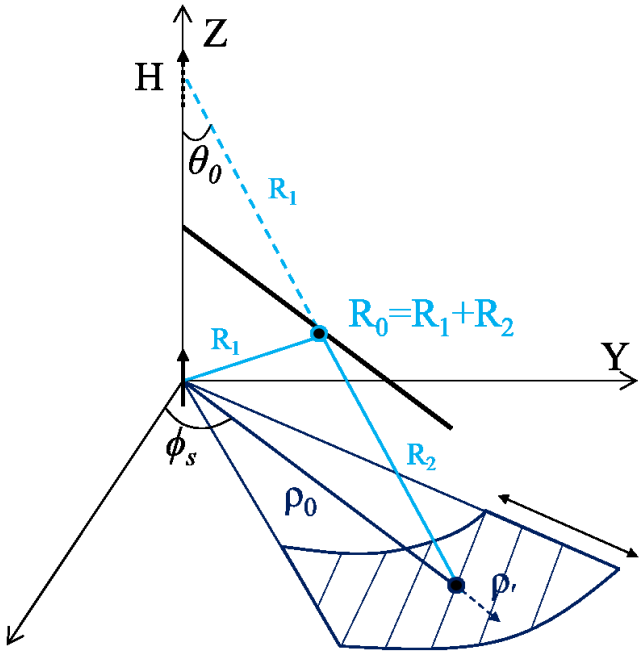

Figure 5.3: The geometry with a scattering patch.

The phase term $e^{-j\pi\alpha(\frac{\rho+R}{c})^2}$ in Eq. (5.13) may be expanded as

$$\begin{aligned} e^{j\pi\alpha(\frac{\rho+R}{c})^2} &= e^{j\pi\alpha\left[\left(\frac{\rho_0+R_0}{c}\right)^2+k_r(\rho'+R')+\left(\frac{\rho'+R'}{c}\right)^2\right]} \\ &\approx e^{j\pi\alpha\left[\left(\frac{\rho_0+R_0}{c}\right)^2+k_r(1+\sin\theta_0)\rho'\right]} \end{aligned} \tag{5.14}$$

Then, changing the integration variable from ρ to ρ', Eq. (5.13) becomes

$$\begin{aligned} (E_0)^D_{1FM}(\omega_r) = &\frac{-jI_0\eta_0\Delta l k_0^2 T_r}{(2\pi)^{3/2}} e^{j\pi/4} \sum_{\vec{K}_o}\sum_{\vec{K}_i} P^o_{\vec{K}_o} P^i_{\vec{K}_i} \frac{\vec{K}_o\cdot\vec{K}_s}{K_s^{3/2}} \\ &\cdot \frac{F(\rho_0)}{R_0\sqrt{\rho_0}}\sin(\theta_0) e^{-jK_s\rho_0} e^{j2(k_0-k_r)\rho_r} e^{j\pi\alpha(\frac{2\rho_r}{c})^2} \\ &\cdot \int_{\rho'_{min}}^{\rho'_{max}} e^{-jK_s\rho'} e^{jk_0(1+\sin\theta_0)\rho'} Sa\left[k_B\left(\frac{1+\sin\theta_0}{2}\right)\rho'\right] d\rho' \end{aligned} \tag{5.15}$$

Noting that $Sa(-x) = Sa(x)$, the integral limits ρ'_{min} and ρ'_{max} are defined as $\pm\Delta r$. In physical sense, the lower limit of the ρ'-integral ρ'_{min} corresponds to the range of the radar relative to the position of the scattering point, while the upper limit ρ'_{max} indicates the range at which the radar return becomes negligible. Meanwhile, it is considered that the sampling function in the integral part is "narrow band" and most of the contribution to the integral comes from within the half power points of the main lobe, which gives

$$-\pi/2 < k_B\left(\frac{1+\sin\theta_0}{2}\right)\rho' < \pi/2.$$

In this case, $2\Delta r$ represents the radial width of the scattering patch on the ocean surface and the "range resolution" is defined as $\Delta\rho$, which is specified approximately as $\Delta\rho = 2\pi/[k_B(1+\sin\theta_0)]$. Because of the sidelobes of the sampling function, the FMCW radar does not have an absolutely defined range resolution. The range resolution $\Delta\rho$ only represents the range of the scattering patch from which the return energy is predominantly received at a given range frequency ω_r. The size of the interaction between range bins

is specified by the parameter Δr. Evaluating the ρ'-integral with these limits, Eq. (5.15) reduces to

$$
\begin{aligned}
(E_0)^D_{1FM}(\omega_r) = {} & \frac{-jI_0\eta_0\Delta l k_0^2 T_r}{(2\pi)^{3/2}} e^{j\pi/4} \sum_{\vec{K}_o} \sum_{\vec{K}_i} P^o_{\vec{K}_o} P^i_{\vec{K}_i} \\
& \cdot \frac{\vec{K}_o \cdot \vec{K}_s}{K_s^{3/2}} \frac{F(\rho_0)}{R_0\sqrt{\rho_0}} \sin\theta_0 e^{j2(k_0-k_r)\rho_r} e^{j\pi\alpha(\frac{2\rho_r}{c})^2} e^{-jK_s\rho_0} \\
& \cdot \frac{2\pi}{k_B(1+\sin\theta_0)} \cdot Sm(K_s, k_B, \Delta r),
\end{aligned}
\tag{5.16}
$$

where $Sm(K_s, k_B, \Delta r)$ is defined as

$$
\begin{aligned}
& Sm(K_s, k_B, \Delta r) = \\
& \frac{1}{\pi}\left\{ Si\left[(K_s - (k_0 + \frac{k_B}{2})(1+\sin\theta_0))\Delta r\right] - Si\left[(K_s - (k_0 - \frac{k_B}{2})(1+\sin\theta_0))\Delta r\right]\right\},
\end{aligned}
$$

and where $Si(x) = \int_0^x \frac{\sin(t)}{t} dt$, and $2\Delta r$ represents the radial width of the scattering patch on the ocean surface.

At this stage, the first-order range spectra for the frequency-modulated wave have been obtained by Fourier transforming the electric field equation over a sweep interval T_r. For the development of the power spectral density, the analysis will include many sweep periods to examine the Doppler shift effect. Firstly, a factor $e^{j(\omega_i+\omega_o)t}$ is introduced into the surface coefficients to indicate the time-varying properties of the ocean and ionosphere surfaces as discussed in previous cases. Additionally, recall that $(E_0)^D_{1FM}(\omega_r)$ is the Fourier transform of the electric field during a sweep at a certain received time t_r. Note too that most of the energy of the sampling function in Eq. (5.13) is associated with its main lobe. Thus, the frequency bandwidth Δf_r for a given ω_r may be specified as

$$
-\frac{\pi}{2} < \frac{T_r\omega_r}{2} < \frac{\pi}{2} \rightarrow \Delta f_r = \frac{1}{T_r}.
$$

Then, the time-varying electric field from successive sweeps is modified as

$$(E_0)^D_{1FM}(\omega_r, t) = (E_0)^D_{1FM}(\omega_r) e^{j(\omega_i+\omega_o)t} \frac{1}{T_r}. \tag{5.17}$$

As discussed in Chapter 2, it is also assumed that ε and R_i represent stationary, homogeneous and independent random processes, making it meaningful to investigate the statistical properties of the received electric field by first introducing its autocorrelation as

$$\mathcal{R}_{1FM}(\tau) = \frac{A_r}{2\eta_0} \langle (E_0)^D_{1FM}(t+\tau)(E_0)^{D*}_{1FM}(t) \rangle. \tag{5.18}$$

With the autocorrelation in place, the first-order received PSD for an FMCW source is found by the Fourier transform of $\mathcal{R}_{1FM}(\tau)$ with respect to the lag time τ as

$$\begin{aligned} \mathcal{P}_{1FM}(\omega_d) =& \mathcal{F}[\mathcal{R}_{1FM}(\tau)] \\ =& \frac{A_r \eta_0 |I_0 \Delta l|^2 k_0^4 \Delta\rho^2}{2(2\pi)^2} \frac{|F(\rho_0)|^2}{R_0^2 \rho_0} \sin^2\theta_0 \\ & \int_{\vec{K}_o} \int_{\vec{K}_i} \int_{\omega_o} \int_{\omega_i} \left(\frac{\vec{K}_o \cdot \vec{K}_s}{K_s^{3/2}} \right)^2 S_o(\vec{K}_o, \omega_o) S_i(\vec{K}_i, \omega_i) \\ & Sm^2(K_s, k_B, \Delta r) \delta\left[\omega_d - (\omega_o + \omega_i)\right] d\vec{K}_o d\vec{K}_i d\omega_o d\omega_i. \end{aligned} \tag{5.19}$$

This integration spans all spatial wave number and temporal frequencies for both the ocean wave spectrum and the spectral representation of the ionospheric reflection coefficient.

5.4 Simulation and Analysis

Before conducting simulations, the power density of the mixed-path ionospheric clutter for an FMCW source is further investigated. First, in Eq. (5.19), the integration over ω_o and ω_i may be performed immediately by incorporating the delta functions, as found in Eq. (1.23) and Eq. (2.23), respectively, which describe the relationships between wavenumbers

and frequencies for ocean waves and ionospheric irregularities, respectively. Then, the $Sm(K_s, k_B, \Delta r)$, which is defined in Eq. (5.12), approaches a rectangular function for the case of large Δr, since, from its definition,

$$\begin{aligned}
&\lim_{\Delta r\to\infty}\left[Sm(K_s, k_B, \Delta r)\right] \\
=&\begin{cases} 1, & (k_0 - \frac{k_B}{2})(1+\sin\theta_0) < K_s < (k_0 + \frac{k_B}{2})(1+\sin\theta_0), \\ 0, & \text{otherwise.} \end{cases} \\
=&\left\{ h\left[K_s - (k_0 - \frac{k_B}{2})(1+\sin\theta_0)\right] - h\left[K_s - (k_0 + \frac{k_B}{2})(1+\sin\theta_0)\right]\right\}.
\end{aligned} \tag{5.20}$$

After a series of derivations similar to the discussion in Appendix A for pulsed source case, the received PSD reduces to

$$\begin{aligned}
\mathcal{P}_{1FM}(\omega_d) =& \frac{A_r\eta_0|I_0\Delta l|^2 k_0^4 \Delta\rho^2}{2(2\pi)^2}\frac{|F(\rho_0)|^2 R_{ia}^2}{R_0^2\rho_0}\sin^2\theta_0 \\
& \frac{k_B(1+\sin\theta_0)}{\sqrt{g}}\int_{\phi_s}\Psi(\omega_d,\phi_s)d\phi_s.
\end{aligned} \tag{5.21}$$

where $\Psi(\omega_d, \phi_s) = \Psi_1(\omega_d, \phi_s) + \Psi_2(\omega_d, \phi_s)$ with

$$\begin{aligned}
\Psi_1(\omega_d,\phi_s) = &\int_{K_i} K_i K_o^{3/2}\left|\frac{\vec{K}_o\cdot\vec{K}_s}{K_s}\right| S_o(K_o,\phi_o)S_i(K_i) \\
&\cdot\left|\frac{K_i\cos(\phi_i-\phi_s)-K_s}{K_iK_s\sin(\phi_i-\phi_s)-K_o\frac{dK_o}{d\phi_i}}\right| dK_i,
\end{aligned} \quad \text{for m=1,}$$

and

$$\begin{aligned}
\Psi_2(\omega_d,\phi_s) = &\int_{K_i} K_i K_o^{3/2}\left|\frac{\vec{K}_o\cdot\vec{K}_s}{K_s}\right| S_o(K_o,\phi_o+\pi)S_i(K_i) \\
&\cdot\left|\frac{K_i\cos(\phi_i-\phi_s)-K_s}{K_iK_s\sin(\phi_i-\phi_s)+K_o\frac{dK_o}{d\phi_i}}\right| dK_i,
\end{aligned} \quad \text{for m=-1.}$$

Then, $S_o(K_o, \phi_o)$ and $S_i(K_i)$ are specified by particular physical models of the ocean surface and the IRC as discussed in Sections 1.2.3 and 2.3.2. Finally, this power density is also normalized by the average first-order ocean clutter peak power density, and the main

Table 5.1: Main parameters involved in the simulations

centre frequency for FMCW (f_0)	4.1 MHz
sweep interval (T_r) for FMCW	0.5 s
sweep bandwidth (B) for FMCW	100 kHz
radar look direction (ϕ_s)	0°
ionosphere height ($H/2$)	300 km
typical ionospheric horizontal plasma drift velocity (v_h)	100 m/s
ionosphere direction (θ_{ih})	0°
wind speed (U)	10 m/s
wind direction (θ)	90°

parameters involved in the simulation are listed in Table 5.1. Using these parameters, the first-order normalized received power density via the mixed-path path for a FMCW source is compared with that of a pulsed radar for the same ocean scattering patch. The range resolution for the FMCW source is given as $\frac{c}{2B}$, and since B is chosen as 100kHz thus the radial width of the scattering is calculated to be 1.5 km. In the case of the pulsed radar, the corresponding pulse length is set to be 10 μs. Figure 5.4 shows that the plots with the two sources are coincident with each other. The power density of the ionospheric clutter exceeds that of the average first-order ocean clutter peak by roughly 45 dB. Since the mixed-path echo travels much less distance over the ocean surface than that through pure surface wave propagation with the same apparent range, the mixed-path clutter suffers less surface attenuation. Additionally, at the range of 300 km the backscatter power density of

the sea clutter is very low.

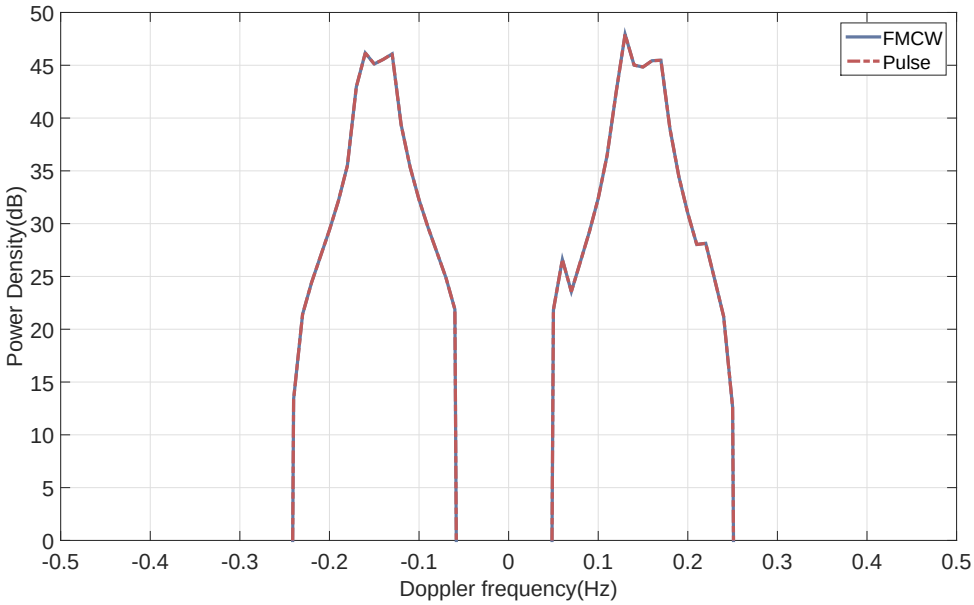

Figure 5.4: First-order PSD for FMCW and pulsed HF radar.

Next, the dependence of the first-order received normalized PSD of the ionosphere-ocean scatter for an FMCW source on radar operating frequency is simulated and shown in Figure 5.5. Assuming that the radio waves with different frequencies are reflected by the ionosphere at the same height, it is observed that the Doppler frequencies of the first-order dominant peaks increases with the operating frequency. This may be explained by the fact that, according to the the Bragg scattering condition, the radio waves with higher frequency are Bragg scattered by the ionospheric irregularities and ocean waves with greater wavenumers. Since the velocity of the ionosphere is assumed to be constant, the Doppler frequency of the Bragg peak depends on the frequency of ocean waves, and the dispersion relationship of ocean waves indicates that greater wavenumber corresponds to higher frequency. It may

be also noticed that the average normalized power density of the ionospheric clutter varies from 40 dB to 50 dB when the operating frequency increase from 2.5 MHz to 13 MHz. The Doppler spread is about 0.2 Hz in all cases.

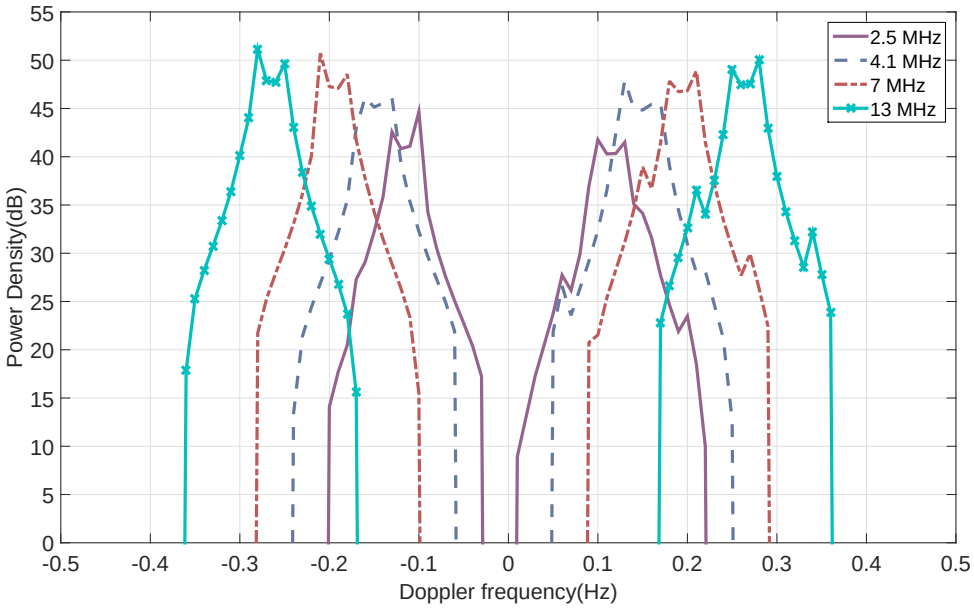

Figure 5.5: First-order ionosphere clutter PSD for FMCW with varying radar operating frequency.

Finally, with the height of the ionospheric reflection layer set as 300 km, normalized ionospheric clutter PSD for different apparent ranges ($(R_1 + \rho_1)/2$) are simulated and depicted in Figure 5.6. This figure shows that the Doppler frequencies of the first-order dominant peaks increases with the apparent range of the mixed-path propagation, but the peak power density decreases from 45 dB to 38 dB when the apparent range varies from 310 km to 400 km. On one hand, the variation of the apparent range for a fixed ionosphere height corresponds to the change of the incidence angle θ_i of the radio waves on the ionosphere,

which may affect the Doppler frequencies corresponding to the Bragg scattering. On the other hand, increasing apparent ranges may cause longer surface propagation ranges, in which cases the received power density will decrease. The bandwidth of each spectrum changes slightly for different apparent ranges.

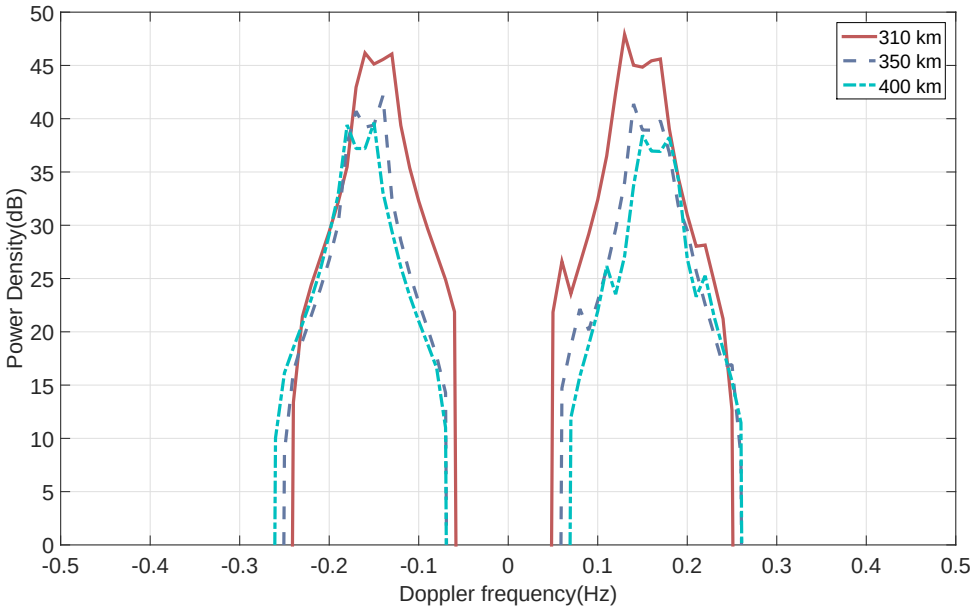

Figure 5.6: First-order ionosphere clutter PSD for FMCW with different apparent ranges.

5.5 General Chapter Summary

The first-order FMCW backscatter power spectral density (PSD) for mixed-path ionosphere-ocean propagation has been derived in this chapter. The general method followed that appearing in [83] and [86]. First, an expression for the first-order electric field was derived for the mixed-path case in which scattering occurs from both the ionosphere and the ocean

surface. Then, this field was Fourier transformed and the frequency distribution of the demodulated electric field indicates range information of the mixed-path propagation. Finally, the first-order PSD was developed by assuming the ocean surface and the ionosphere are stochastic processes. To investigate the PSD of this ionospheric-clutter mode and its relative power density to that of the average first-order ocean clutter peak, a normalized ionospheric-clutter power density was simulated and compared with that for a pulsed radar for the same ocean scattering patch. Subsequently, it was shown that changes in radar operating frequency and the apparent range result in the variation of the Doppler frequency and power density of the first-order dominant peaks in the power density spectrum of this mixed-path propagation. Other factors, such as ionospheric plasma drift velocities and surface wind direction, will have similar effects on the normalized PSD obtained using an FMCW source to that with a pulsed source. The ratio of the ionospheric clutter to the average first-order ocean clutter peak power density indicates this clutter may have a significantly negative impact on the performance of the HFSWR.

Chapter 6

Conclusions

6.1 General Summary and Significant Results

This thesis has addressed the development of ionospheric clutter models for high frequency surface wave radar (HFSWR). The ionospheric clutter includes two feasible propagation paths. The upwards transmitted signal may be reflected from the ionosphere to the receivers directly (vertical ionospheric clutter) or via the ocean surface (mixed-path ionospheric clutter). Both cases have been investigated based on previous work analyzing the radar cross sections of the sea surface scattering for oceanic remote sensing [37–39] and Walsh's mixed-path model [41]. The work in this thesis is intended to provide theoretical characterizations of the ionospheric clutter which may be later implemented in suppression schemes, particularly as applied to sea state monitoring or hard target detection using HF radar.

First, the representation of the ionospheric reflection coefficient (IRC) was addressed in Chapter 2. This helped to indicate the influence of the ionosphere on radio waves propa-

gation. Based on the ionospheric layered model, this reflection coefficient is shown to be a function of the ionospheric electron density and to be dependent on both ocean surface observation position and radio wave frequency. The IRC's real part accounts for the ionospheric absorption of the radio wave energy by electron collisions, and its imaginary part represents phase deviations of the radio wave's electric field because of the interaction with the ionosphere. In the absence of the Earth's magnetic field and the ionospheric absorption, the phase part may be taken as a zero mean random variable, which is fundamentally caused by the electron density irregularities, such as small-scale irregularities and large-scale travelling ionospheric disturbances (TIDs). In this thesis, the relationship between the ionospheric spectral density of the IRC and the electron density irregularities is derived and includes various ionospheric parameters. This IRC model has been incorporated into the ionospheric clutter models of the mixed-path and vertical propagation in subsequent chapters.

The analysis of the mixed-path ionospheric clutter started from the received electric field equation of the rough surface scattering for ionosphere-ocean propagation. In Chapter 3, an approximate solution for this field is expanded to second-order for ocean surface scattering using a Neumann series, and the second-order monostatic power spectral density (PSD) model is investigated for a pulsed source. In this case, the signals from the ionosphere may be reflected back to the receivers by two scatters from first-order ocean waves (electromagnetic effect) or one scatter from a second-order ocean wave (hydrodynamic effect). The contribution from the so-called electromagnetic effect is derived for the patch scatter condition, while that of the hydrodynamic effect is similarly obtained by appropriately modifying the first-order field equation. The total frequency-domain electric field for

a general source current is inversely Fourier transformed and a time-domain pulsed radar source is incorporated into the analysis. Assuming that the ionosphere and the ocean surface roughness may be represented as stochastic processes, the second-order received PSD model is developed by Fourier transforming the field autocorrelation.

In Chapter 4, two special cases incorporating a pulsed radar source are introduced. For the vertical ionospheric clutter case, the received electric field of radio waves travelling vertically upwards and reflected by the ionosphere to the receivers is treated based on image theory. Then, the PSD of the vertical ionospheric clutter for the monostatic case incorporating a pulsed source is derived by taking steps corresponding to those used in the mixed-path case [41]. Subsequently, for the first-order bistatic mixed-path ionospheric clutter, the frequency-domain electric field was determined with the aid of elliptical coordinates. After incorporating a pulsed source current, the first-order power spectrum for the bistatic configuration was derived.

Finally, in Chapter 5, an investigation of the first-order monostatic mixed-path ionospheric clutter was presented for a frequency-modulated continuous waveform (FMCW) radar source current. The motivation for this lies in the fact that such waveforms have been widely applied in HFSWR remote sensing applications. The frequency distribution of the demodulated field incorporating an FMCW source indicates range information of the mixed-path propagation and its PSD model is then obtained.

In order to investigate the PSD of this ionospheric clutter and its relative intensity to that of the average first-order ocean clutter peak, the normalized ionospheric clutter power density is simulated under a variety of ionospheric conditions, radar parameters and sea states.

For the mixed-path case involving various ionospheric conditions, simulation results show that the horizontal ionospheric plasma drift velocity results in a significant Doppler spreading of the power density spectra, while the vertical ionospheric motion introduces a Doppler shift corresponding to its velocity. The Doppler bandwidth of the ionospheric clutter may also be broadened by increasing the wavenumber bandwidth of the IRC, which is determined by the wavenumber range of the ionospheric irregularities. Furthermore, the Doppler frequencies of the first-order dominant peaks increase with the radar operating frequency and the apparent range. This may be explained by the fact that the Bragg scattering conditions for the radio waves scattering from the ionosphere and ocean surface depend on the wavelength of the radio waves and the incidence angle. It is also observed that higher peak values occur for higher operating frequencies and lower apparent ranges. The PSD for the mixed-path case is further investigated for various sea states. When the angle between the surface wind direction and the radar look direction for monostatic radar (or the direction of the ellipse normal for bistatic radar) increases from 0° to 180°, the average power density for the negative Doppler frequency decreases from its maximum, while that of the positive Doppler frequency increases from its minimum. This is due to the fact that the outward component of the surface wind enhances the power density in the negative Doppler region and vice versa. The second-order power density of the mixed-path propagation is also influenced by surface wind speeds. This shows that the average power density increases and the bandwidth becomes narrower with increasing wind speeds, indicating that higher sea states may enhance the second-order radar backscatter for mixed-path propagation.

For vertical ionospheric clutter, simulations of the normalized power density were first conducted with different ionospheric conditions. The results also show that the horizontal

ionospheric velocity and the wavenumber bandwidth of the IRC lead to Doppler spreading, and vertical directional velocity leads to an observed Doppler shift. In addition, the PSDs with higher radar operating frequencies and greater reflection heights have higher peak values and broader bandwidths.

The average ionospheric clutter power density in all cases exceeds that of the average first-order sea clutter peak by more than 30 dB. In practice, this value may vary with ionospheric absorption, attenuation imposed by the surface, the relative ranges of mixed-path and surface propagation, and the size of the ocean surface scattering patch. It should be noted that the simulated results seem to differ from the Doppler spectra generated from real HF radar data since the latter contains both the first and higher order continuum sea clutter and ionospheric clutter at the same apparent range, while the simulations illustrate only one kind of ionospheric clutter normalized to the average peak power density of the first-order ocean clutter.

The better understanding of the ionospheric clutter problem in this thesis gives a sense of how this clutter was characterized for a variety of sea states, ionospheric conditions and radar parameters in the range-Doppler spectra of HFSWR. These insights may potentially lead to better ionospheric clutter suppression schemes that will facilitate sea state parameter extraction and hard target detection using HFSWR systems. Moreover, the modelling of ionosphere and sea surface scattering presented in this thesis may be applied to a theoretical analysis for sky wave or sky-surface wave hybrid HF radar.

6.2 Suggestions for Future Work

Based on the analyses in this thesis, several points may be suggested for future experimental and theoretical research work.

The activities of the ionosphere are likely to be far more complex in reality than presented in the models in this thesis. Although the statistical relationship between the ionospheric reflection coefficient and the electron density for the case of single scattering of the radio waves by small-scale ionospheric irregularities has been derived, models of the real-time ionospheric characteristics, in which both the earth's magnetic field and ionospheric absorption are included, should be further investigated. As the ionospheric electron density irregularities ΔN_e increase, multiple scattering effects become significant and may create a regular spatio-angular pattern in the amplitude of radio waves reflected by the anisotropic ionosphere at the sea level. Additionally, in practice, TIDs may cause multipath reflections of the radio waves within the ionosphere. Moreover, several prominent TIDs propagating in different directions may exist simultaneously. While these effects are not addressed here, they may be examined in future work by introducing appropriate complexities into the ionospheric model.

The multiple scattering of the radio waves due to plasma irregularities and turbulences within the ionosphere may also be taken into account. Moreover, some of the radar and environmental parameters (antenna gains, beam-widths, spherical earth attenuation, etc.) affect only the predicted magnitude of the ionospheric clutter for all Doppler frequencies. The numerical simulations are meant to exhibit general properties of the modelled ionospheric clutter by setting these parameters to constant values. These parameters may be

considered and analysed in future experimental designs.

The models detailed in this thesis are analytical in nature and derived with restrictions. It is necessary to examine them comprehensively using field data obtained from subsequent HFSWR experimentation with simultaneous operation of an ionosonde recently obtained by the radar group at Memorial University. As discussed, the ionospheric conditions, such as horizontal and vertical ionospheric drift velocities, spectral densities of the electron density irregularities, and reflection heights of the ionospheric layers, may be expected to influence the features observed in the ionospheric clutter. Thus, the theoretical models may be evaluated and improved by comparing the ionospheric information extracted from the range-Doppler spectra of the radar echoes with those obtained from corresponding ionograms simultaneously measured by an ionosonde.

Bibliography

[1] E. D. R. Shearman, “Radio science and oceanography,” *Radio Science*, vol. 18, pp. 299–320, May 1983.

[2] T. Helzel, M. Kniephoff, and L. Petersen, “WERA: Remote ocean sensing for current, wave and wind direction,” in *Proceedings of IEEE US/EU Baltic International Symposium*, pp. 1–8, May 2006.

[3] W. J. G. Beynon and P. J. S. Williams, “Incoherent scatter of radio waves from the ionosphere,” *Reports on Progress in Physics*, vol. 41, no. 6, p. 909, 1978.

[4] L. R. Wyatt, “HF radar for coastal monitoring - a comparison of methods and measurements,” in *Proceedings of Europe Oceans Conference*, vol. 1, pp. 314–318 Vol. 1, June 2005.

[5] D. E. Barrick, “HF radio oceanography - A review,” *Boundary-Layer Meteorol*, vol. 13, pp. 23–43, Jan. 1978.

[6] B. Lipa and B. Nyden, “Directional wave information from the SeaSonde,” *IEEE Journal of Oceanic Engineering*, vol. 30, pp. 221–231, Jan. 2005.

[7] L. R. Wyatt, J. J. Green, A. Middleditch, M. D. Moorhead, J. Howarth, M. Holt, and S. Keogh, "Operational wave, current, and wind measurements with the pisces HF radar," *IEEE Journal of Oceanic Engineering*, vol. 31, pp. 819–834, Oct. 2006.

[8] R. Jones, T. Georges, and J. Riley, "Measured ionospheric distortion of HF ground-backscatter spectra," *IEEE Transactions on Antennas and Propagation*, vol. 34, pp. 563–568, Apr. 1986.

[9] L. Sevgi, A. Ponsford, and H. C. Chan, "An integrated maritime surveillance system based on high-frequency surface-wave radars. 1. Theoretical background and numerical simulations," *IEEE Antennas and Propagation Magazine*, vol. 43, pp. 28–43, Aug. 2001.

[10] K. Davies, *Ionospheric Radio*. Peregrinus, 1990.

[11] K. G. Budden, *The Propagation of Radio Waves: the Theory of Radio Waves of Low Power in the Ionosphere and Magnetosphere*. New York: Cambridge University Press, 1985.

[12] G. Wyman, "Characterising the ionosphere," Technical report, NATO Science Technology Organization, TR-IST-051, Sept. 2009.

[13] L. Sevgi, "A mixed-path groundwave field strength prediction virtual tool for digital radio broadcast systems in medium and short wave bands," *IEEE Antennas and Propagation Magazine*, vol. 48, pp. 19–27, Aug. 2006.

[14] G. A. Fabrizio, *High Frequency Over-the-Horizon Radar: Fundamental Principles, Signal Processing, and Practical Applications*. McGraw-Hill Education, 2013.

[15] T. Thayaparan and J. MacDougall, “The role of ionospheric clutter in mid-latitude and arctic regions for assessment of hfswr surveillance,” Technical report, Defence R & D Canada - Ottawa, DRDC-OTTAWA-TR-2004-093, 2004.

[16] T. Thayaparan and J. MacDougall, “Investigation of ionospheric clutter using ionosondes in mid-latitude and arctic regions aimed at feasibility assessment of the high-frequency surface-wave radar surveillance,” in *Remote Sensing of Clouds and the Atmosphere VIII*, vol. 5235, pp. 607–618, 2004.

[17] G. Chisham, M. Lester, S. E. Milan, *et al.*, “A decade of the super dual auroral radar network (SuperDARN): Scientific achievements, new techniques and future directions,” *Surveys in Geophysics*, vol. 28, pp. 33–109, Jan. 2007.

[18] R. T. Tsunoda, R. C. Livingston, J. J. Buonocore, and A. V. McKinley, “The frequency-agile radar: A multifunctional approach to remote sensing of the ionosphere,” *Radio Science*, vol. 30, pp. 1623–1643, Sept. 1995.

[19] H. Leong, “Adaptive nulling of skywave interference using horizontal dipole antennas in a coastal surveillance HF surface wave radar system,” in *IEE Proceedings, Radar Conference*, pp. 26–30, Oct. 1997.

[20] H. Gao, X. Zheng, and J. Li, “Adaptive anti-interference technique using subarrays in HF surface wave radar,” *IEE Proceedings, Radar, Sonar and Navigation*, vol. 151, pp. 100–104, Apr. 2004.

[21] W. Xianrong, K. Hengyu, and W. Biyang, "Adaptive ionospheric clutter suppression based on subarrays in monostatic HF surface wave radar," *IEE Proceedings, Radar, Sonar and Navigation*, vol. 152, pp. 89–96, Apr. 2005.

[22] H. Zhou, B. Wen, and S. Wu, "Ionospheric clutter suppression in HFSWR using multilayer crossed-loop antennas," *IEEE Geoscience and Remote Sensing Letters*, vol. 11, pp. 429–433, Feb. 2014.

[23] R. J. Riddolls, "Mitigation of ionospheric effects on high frequency surface wave radar," in *Proceedings of NATO RTO Specialists' Meeting on Characterising the Ionosphere, RTO-MP-IST-056*, June 2006.

[24] L. E. Brennan and L. S. Reed, "Theory of adaptive radar," *IEEE Transactions on Aerospace and Electronic Systems*, vol. AES-9, pp. 237–252, Mar. 1973.

[25] S. Bidon, O. Besson, and J. Y. Tourneret, "Knowledge-aided STAP in heterogeneous clutter using a hierarchical bayesian algorithm," *IEEE Transactions on Aerospace and Electronic Systems*, vol. 47, pp. 1863–1879, July 2011.

[26] J. Xie, Y. Yuan, and Y. Liu, "Suppression of sea clutter with orthogonal weighting for target detection in shipborne HFSWR," *IEE Proceedings, Radar, Sonar and Navigation*, vol. 149, pp. 39–44, Feb. 2002.

[27] G. A. Fabrizio, A. Farina, and M. Turley, "Spatial adaptive subspace detection in OTH radar," *IEEE Transactions on Aerospace and Electronic Systems*, vol. 39, pp. 1407–1428, Oct. 2003.

[28] G. A. Fabrizio and A. Farina, “GLRT-based adaptive Doppler processing for HF radar systems,” in *Proceedings of IEEE International Conference on Acoustics, Speech and Signal Processing*, vol. 2, pp. 949–952, Apr. 2007.

[29] M. Ravan, O. Saleh, R. S. Adve, K. Plataniotis, and P. Missailidis, “KB-STAP implementation for HFSWR,” Technical report, Defence R & D Canada - Ottawa, DSS Contract No. W7714-060999/001/SV, Mar. 2008.

[30] O. Saleh, R. Adve, and R. Riddolls, “Fast fully adaptive processing: A multistage STAP approach,” in *Proceedings of IEEE Radar Conference*, pp. 1–6, May 2009.

[31] Y. Li, Y. Wei, R. Xu, Z. Wang, and T. Chu, “An ionospheric Es layer clutter model and suppression in HF surfacewave radar,” *International Journal of Antennas and Propagation*, vol. 2013, pp. 1–18, June 2013.

[32] X. Zhang, W. Deng, Q. Yang, and Y. Dong, “Modified space-time adaptive processing with first-order bragg lines kept in HFSWR,” in *Proceedings of IEEE Radar Conference*, pp. 1–4, Oct. 2014.

[33] G. A. Fabrizio, *Space-time characterisation and adaptive processing of ionospherically-propagated HF signals*. PhD thesis, University of Adelaide, 2000.

[34] R. J. Riddolls, “A model of radio wave propagation in ionospheric irregularities for prediction of high-frequency radar performance high frequency surface wave radar,” Technical report, Defence R & D Canada - Ottawa, TM 2006-284, Dec. 2006.

[35] C. J. Coleman, "A model of HF sky wave radar clutter," *Radio Science*, vol. 31, pp. 869–875, July 1996.

[36] M. Ravan, R. J. Riddolls, and R. S. Adve, "Ionospheric and auroral clutter models for HF surface wave and over-the-horizon radar systems," *Radio Science*, vol. 47, p. RS3010, June 2012.

[37] J. Walsh and E. W. Gill, "An analysis of the scattering of high-frequency electromagnetic radiation from rough surfaces with application to pulse radar operating in backscatter mode," *Radio Science*, vol. 35, pp. 1337–1359, Nov. 2000.

[38] E. W. Gill and J. Walsh, "Bistatic form of the electric field equations for the scattering of vertically polarized high-frequency ground wave radiation from slightly rough, good conducting surfaces," *Radio Science*, vol. 35, pp. 1323–1335, Nov. 2000.

[39] E. W. Gill and J. Walsh, "High-frequency bistatic cross sections of the ocean surface," *Radio Science*, vol. 36, pp. 1459–1475, Nov. 2001.

[40] J. Walsh, "Mixed-path propagation theory," Technical report, Defence R & D Canada - Ottawa, DSS Contract No. W7714-1-050932/001- SV, Jan. 2006.

[41] J. Walsh, E. Gill, W. Huang, and S. Chen, "On the development of a high-frequency radar cross section model for mixed path ionosphere-ocean propagation," *IEEE Transactions on Antennas and Propagation*, vol. 63, pp. 2655–2664, June 2015.

[42] H. Chan, "Characterization of ionospheric clutter in HF surface-wave radar," Technical report, Defence R & D Canada - Ottawa, TR-2003-114, 2003.

[43] D. E. Barrick, “Theory of HF and VHF propagation across the rough sea, 1, the effective surface impedance for a slightly rough highly conducting medium at grazing incidence,” *Radio Science*, vol. 6, pp. 517–526, May 1971.

[44] S. Srivastava and J. Walsh, “An analysis of the second-order Doppler return from the ocean surface,” *IEEE Journal of Oceanic Engineering*, vol. 10, pp. 443–445, Oct. 1985.

[45] J. Walsh, R. Howell, and B. Dawe, “Model development for evaluation studies of ground wave radar,” Technical report, Contract report for the Department of National Defence, Government of Canada, DSS Contract No. W7714-8-563/01-SS, 1990.

[46] J. Walsh and R. Donnelly, “Consolidated approach to two-body electromagnetic scattering,” *Physical Review A*, vol. 36, pp. 4474–4485, Nov. 1987.

[47] A. Sommerfeld, “The propagation of waves in wireless telegraphy,” *Annals of Physics*, vol. 28, pp. 665–736, Jan. 1909.

[48] E. H. Newman, “An investigation of the effects of a lossy earth on antenna patterns at vhf,” tech. rep., DTIC Document, 1972.

[49] N. Bleistein and R. Handelsman, *Asymptotic Expansion of Integrals*. International Geophysics, New York: Holt, Rinehart and Winston, 1975.

[50] B. Kinsman, *Wind Waves: Their Generation and Propagation on the Ocean Surface*. Courier Corporation, 2002.

[51] M. Tucker, *Waves in Ocean Engineering*. International Geophysics, New York: Ellis Horwood, 1991.

[52] W. J. Pierson and L. Moskowitz, "A proposed spectral form for fully developed wind seas based on the similarity theory of S. A. Kitaigorodskii," *Journal of Geophysical Research*, vol. 69, pp. 5181–5190, Dec. 1964.

[53] E. W. Gill, *The scattering of high frequency electromagnetic radiation from the ocean surface : An analysis based on a bistatic ground wave radar configuration*. PhD thesis, Memorial University of Newfoundland, 1999.

[54] J. Walsh, W. Huang, and E. Gill, "The second-order high frequency radar ocean surface cross section for an antenna on a floating platform," *IEEE Transactions on Antennas and Propagation*, vol. 60, pp. 4804–4813, Oct. 2012.

[55] K. B. Baker, R. A. Greenwald, J. P. Villian, and S. Wing, "Spectral characteristics of high frequency (HF) backscatter for high latitude ionospheric irregularities: Preliminary analysis of statistical properties," Technical report, Johns Hopkins University Applied Physics Laboratory, July 1988.

[56] X. Vallires, J. Villain, C. Hanuise, and R. Andr, "Ionospheric propagation effects on spectral widths measured by SuperDARN HF radars," *Annales Geophysicae*, vol. 22, pp. 2023–2031, June 2004.

[57] R. F. Woodman and S. Basu, "Comparison between in-situ spectral measurements of F-region irregularities and backscatter observations at 3 m wavelength," *Geophysical Research Letters*, vol. 5, pp. 869–872, Oct. 1978.

[58] F. F. Chen, *Introduction to Plasma Physics and Controlled Fusion*. Boston, MA: Springer US, 1984.

[59] V. E. Gherm, N. N. Zernov, and H. J. Strangeways, "HF propagation in a wideband ionospheric fluctuating reflection channel: Physically based software simulator of the channel," *Radio Science*, vol. 40, p. RS1001, Feb. 2005.

[60] J. Walsh, S. Chen, E. Gill, and W. Huang, "High frequency radar clutter power for mixed ionosphere-ocean propagation," in *Proceedings of 16th International Symposium on Antenna Technology and Applied Electromagnetics*, pp. 1–2, July 2014.

[61] R. G. Gillies, G. C. Hussey, G. J. Sofko, and K. A. McWilliams, "A statistical analysis of SuperDARN scattering volume electron densities and velocity corrections using a radar frequency shifting technique," *J. Geophys. Res.*, vol. 117, p. A08320, Aug. 2012.

[62] V. S. Beley, V. G. Galushko, and Y. M. Yampolski, "Traveling ionospheric disturbance diagnostics using HF signal trajectory parameter variations," *Radio Science*, vol. 30, pp. 1739–1752, Nov. 1995.

[63] S. Anderson, "Multiple scattering of HF skywave radar signals: Physics, interpretation and exploitation," in *Proceedings of IEEE Radar Conference*, pp. 1–5, May 2008.

[64] P. Liu, *Theory of Ionospheric Waves*. International Geophysics, Elsevier Science, 1973.

[65] J. Wagen and K. C. Yeh, "A numerical study of waves reflected from a turbulent ionosphere," *Radio Science*, vol. 21, pp. 583–604, July 1986.

[66] V. I. Tatarskii, *The Effects of the Turbulent Atmosphere on Wave Propagation*. Jerusalem: Israel Program for Scientific Translations, 1971.

[67] G. Crowley and F. S. Rodrigues, "Characteristics of traveling ionospheric disturbances observed by the TIDDBIT sounder," *Radio Science*, vol. 47, p. RS0L22, Aug. 2012.

[68] H. Zhou, B. Wen, and S. Wu, "Ionosphere probing with a high frequency surface wave radar," *Progress In Electromagnetics Research C*, vol. 20, pp. 203–214, 2011.

[69] M. Kelley, *The Earth's Ionosphere: Plasma Physics & Electrodynamics*. International Geophysics, Elsevier Science, 2009.

[70] B. W. Reinisch, J. L. Scali, and D. L. Haines, "Ionospheric drift measurements with ionosondes," *Annals of Geophysics*, vol. 41, Nov. 1998.

[71] S. Basu, S. Basu, E. MacKenzie, W. R. Coley, W. B. Hanson, and C. S. Lin, "F region electron density irregularity spectra near auroral acceleration and shear regions," *Journal of Geophysical Research*, vol. 89, pp. 5554–5564, July 1984.

[72] S. Chen, E. Gill, and W. Huang, "A high frequency surface wave radar ionospheric clutter model for mixed-path propagation with second-order sea scattering," *IEEE Transactions on Antennas and Propagation*, 2016. In press, DOI: 10.1109/TAP.2016.2618538.

[73] S. Chen, E. Gill, and W. Huang, "A second-order monostatic high frequency radar power model for mixed-path propagation," in *Proceedings of 17th International Symposium on Antenna Technology and Applied Electromagnetics*, pp. 1–2, July 2016.

[74] M. Abramowitz and I. A. Stegun, *Handbook of Mathematical Functions*. New York: Dover, 1970.

[75] K. Hasselmann, "Determination of ocean wave spectra from Doppler radio return from the sea surface," *Nature*, vol. 229, pp. 16–17, Jan. 1971.

[76] B. L. Weber and D. E. Barrick, "On the nonlinear theory for gravity waves on the ocean's surface. part I: Derivations," *Journal of Physical Oceanography*, vol. 7, pp. 3–10, Jan. 1977.

[77] S. Chen, W. Huang, and E. W. Gill, "A vertical reflection ionospheric clutter model for high frequency surface wave radar," in *Proceedings of IEEE International Symposium on Antennas and Propagation USNC/URSI National Radio Science Meeting*, pp. 999–1000, July 2015.

[78] S. Chen, W. Huang, and E. Gill, "A vertical reflection ionospheric clutter model for HF radar used in coastal remote sensing," *IEEE Antennas and Wireless Propagation Letters*, vol. 14, pp. 1689–1693, 2015.

[79] S. Chen, W. Huang, and E. Gill, "First-order bistatic high frequency radar power for mixed-path ionosphere-ocean propagation," *IEEE Geoscience and Remote Sensing Letters*, 2016. In press, DOI: 10.1109/LGRS.2016.2618855.

[80] D. D. Crombie, "Doppler spectrum of sea echo at 13.56 Mc./s.," *Nature*, vol. 175, pp. 681–682, Apr. 1955.

[81] B. Edde, *Radar: Principles, Technology, Applications*. Englewood Cliffs, N.J: Prentice Hall, Sept. 1992.

[82] D. E. Barrick, “FM/CW radar signals and digital processing,” Technical report, NOAA,ERL283-WPL, July 1973.

[83] J. Walsh, J. Zhang, and E. Gill, “High-frequency radar cross section of the ocean surface for an FMCW waveform,” *IEEE Journal of Oceanic Engineering*, vol. 36, pp. 615–626, Oct. 2011.

[84] S. Chen, W. Huang, and E. Gill, “The first-order FMCW HF radar cross section model for ionosphere-ocean propagation,” in *Proceedings of IEEE Oceans Conference*, pp. 1–5, Sept. 2014.

[85] J. Zhang, *On the variability of doppler spectra in HF groundwave radar remote sensing over the ocean surface: An investigation based on pulsed and frequency modulated sources*. PhD thesis, Memorial University of Newfoundland, 2009.

[86] S. Chen, E. W. Gill, and W. Huang, “A first-order HF radar cross section model for mixed-path ionosphere-ocean propagation with an FMCW source,” *IEEE Journal of Oceanic Engineering*, vol. 41, no. 4, pp. 982–992, 2016.

[87] A. Ishimaru, *Electromagnetic Wave Propagation, Radiation and Scattering*. Englewood Cliffs, New Jersey: Prentice-Hall Inc., 1991.

[88] R. Khan, B. Gamberg, D. Power, J. Walsh, B. Dawe, W. Pearson, and D. Millan, “Target detection and tracking with a high frequency ground wave radar,” *IEEE Journal of Oceanic Engineering*, vol. 19, pp. 540–548, Oct. 1994.

Appendix A

Evaluation of Integral in the First-Order Power Spectral Density Equation (2.28)

Attention is now turned to the evaluation of the integral portion of Eq. (2.28), symbolized here as

$$\begin{aligned} I = & \int_{K_o} \int_{K_i} \int_{\phi_o} \int_{\phi_i} \left(\frac{\vec{K}_o \cdot \vec{K}_s}{K_s^{3/2}} \right)^2 \sum_{m=\pm 1} S_o(m\vec{K}_o) S_i(K_i) \\ & \cdot \delta(\omega_d + m\sqrt{gK_o} + \vec{K}_i \cdot \vec{v}_h + 2k_0 v_v \cos\theta_i) \\ & \cdot Sa^2 \left[\frac{\triangle\rho}{2} \{K_s - k_0(1+\sin\theta_0)\} \right] d\phi_i d\phi_o dK_i dK_o. \end{aligned} \tag{A.1}$$

Firstly, the sampling function in Eq. (A.1) has quite narrow band width about the point $K_s = k_0(1+\sin\theta_0)$ and may be simplified to produce a tractable form of the integration I. It seems appropriate to approximate this function by its limit $\Delta\rho \to \infty$, and then,

$$Sa^2 \left[\frac{\triangle\rho}{2} \{K_s - k_0(1+\sin\theta_0)\} \right] \sim \frac{2\pi}{\Delta\rho} \delta[K_s - k_0(1+\sin\theta_0)].$$

For the case of $m = 1$, Eq. (A.1) becomes

$$\begin{aligned} I_1 =& \frac{2\pi}{\Delta\rho} \int_{K_o} \int_{K_i} \int_{\phi_o} \int_{\phi_i} \left(\frac{\vec{K}_o \cdot \vec{K}_s}{K_s^{3/2}} \right)^2 S_o(K_o, \phi_o) S_i(K_i) \\ & \cdot \delta(\omega_d + \sqrt{gK_o} + \vec{K}_i \cdot \vec{v}_h + 2k_0 v_v \cos\theta_i) \\ & \cdot \delta[K_s - k_0(1 + \sin\theta_0)] K_i K_o d\phi_i d\phi_o dK_i dK_o. \end{aligned} \tag{A.2}$$

The K_o-integral will be performed firstly by setting

$$u = \omega_d + \sqrt{gK_o} + \vec{K}_i \cdot \vec{v}_h + 2k_0 v_v \cos\theta_i.$$

Thus,

$$dK_o = \frac{2}{\sqrt{g}} \sqrt{K_o} du,$$

and according to the first delta function, K_o satisfies the equation

$$\begin{aligned} \sqrt{gK_o} =& -(\omega_d + \vec{K}_i \cdot \vec{v}_0) + 2k_0 v_v \cos\theta_i \\ =& -[\omega_d + K_i v_0 \cos(\phi_i - \phi_v) + 2k_0 v_v \cos\theta_i], \end{aligned} \tag{A.3}$$

where ϕ_v is the direction of the horizontal ionospheric plasma drift and noting that K_o is a function of K_i and ϕ_i.

Next, with the aid of the triangle relationship of $\vec{K}_i, \vec{K}_o$ and $\vec{K}_s$– i.e. $\vec{K}_s = \vec{K}_o + \vec{K}_i$–, the integral variable ϕ_o is changed to ϕ_s, which refers to the radar look direction. The relationship

$$K_o \sin(\phi_o - \phi_s) + K_i \sin(\phi_i - \phi_s) = 0$$

gives,

$$d\phi_o = \frac{K_o \cos(\phi_o - \phi_s) + K_i \cos(\phi_i - \phi_s)}{K_o \cos(\phi_o - \phi_s)} d\phi_s = \frac{K_s^2}{\vec{K}_o \cdot \vec{K}_s} d\phi_s. \tag{A.4}$$

Finally, the second delta function is used to evaluate the integral with respect to ϕ_i. The equation relating K_s and ϕ_i is,

$$2K_iK_s\cos(\phi_i-\phi_s)=K_i^2+K_s^2-K_o^2.$$

Accordingly,

$$d\phi_i=\frac{K_i\cos(\phi_i-\phi_s)-K_s}{K_iK_s\sin(\phi_i-\phi_s)-K_o\frac{dK_o}{d\phi_i}}dK_s, \tag{A.5}$$

where, based on Eq. (A.3),

$$\frac{dK_o}{d\phi_i}=2\sqrt{\frac{K_o}{g}}K_iv_0\sin(\phi_i-\phi_v). \tag{A.6}$$

Substituting Eq. (A.3), (A.4) and (A.5) into Eq. (A.2) gives

$$I_1=\frac{2\pi}{\Delta\rho}\frac{2}{\sqrt{g}}\int_{\phi_s}\Psi_1(\omega_d,\phi_s)d\phi_s, \tag{A.7}$$

where $\Psi_1(\omega_d,\phi_s)$ is defined as

$$\begin{aligned}(\omega_d,\phi_s)=\int_{K_i}K_iK_o^{3/2}\left|\frac{\vec{K}_o\cdot\vec{K}_s}{K_s}\right|S_o(K_o,\phi_o)S_i(K_i)\\ \left|\frac{K_i\cos(\phi_i-\phi_s)-K_s}{K_iK_s\sin(\phi_i-\phi_s)-K_o\frac{dK_o}{d\phi_i}}\right|dK_i.\end{aligned}$$

For the case of $m=-1$, the integral in Eq. (A.1) becomes

$$\begin{aligned}I_2=&\frac{2\pi}{\Delta\rho}\int_{K_o}\int_{K_i}\int_{\phi_o}\int_{\phi_i}\left(\frac{\vec{K}_o\cdot\vec{K}_s}{K_s^{3/2}}\right)^2S_o(K_o,\phi_o+\pi)S_i(K_i)\\ &\cdot\delta(\omega_d-\sqrt{gK_o}+\vec{K}_i\cdot\vec{v}_h+2k_0v_v\cos\theta_i)\\ &\cdot\delta[K_s-k_0(1+\sin\theta_0)]K_iK_od\phi_id\phi_odK_idK_o.\end{aligned} \tag{A.8}$$

The evaluation of the integral I_2 may take the same series of steps given above for I_1 with the following differences: K_o now satisfies

$$\begin{aligned}\sqrt{gK_o}=&\omega_d+\vec{K}_i\cdot\vec{v}_0+2k_0v_v\cos\theta_i\\ =&\omega_d+K_iv_0\cos(\phi_i-\phi_v)+2k_0v_v\cos\theta_i,\end{aligned}$$

and accordingly, the derivative in Eq. (A.5) is modified to the negative of (A.6). Thus, the evaluation of I_2 integral is identical with (A.7) with the modification above and $S_o(K_o, \phi_o)$ replaced by $S_o(K_o, \phi_o + \pi)$ as

$$I_2 = \frac{2\pi}{\Delta\rho}\frac{2}{\sqrt{g}}\int_{\phi_s} \Psi_2(\omega_d, \phi_s)d\phi_s, \tag{A.9}$$

where $\Psi_2(\omega_d, \phi_s)$ is defined as

$$(\omega_d, \phi_s) = \int_{K_i} K_i K_o^{3/2} \left|\frac{\vec{K}_o \cdot \vec{K}_s}{K_s}\right| S_o(K_o, \phi_o + \pi) S_i(K_i) \left|\frac{K_i \cos(\phi_i - \phi_s) - K_s}{K_i K_s \sin(\phi_i - \phi_s) + K_o \frac{dK_o}{d\phi_i}}\right| dK_i.$$

The complete integral I is therefore,

$$I = I_1 + I_2 = \frac{2\pi}{\Delta\rho}\frac{2}{\sqrt{g}}\int_{\phi_s} \Psi(\omega_d, \phi_s)d\phi_s, \tag{A.10}$$

where $\Psi(\omega_d, \phi_s) = \Psi_1(\omega_d, \phi_s) + \Psi_2(\omega_d, \phi_s)$.

Appendix B

Evaluation of Integral in the Second-Order Power Spectral Density Equation (3.32)

The integral in Eq. (3.32) is symbolized by

$$
\begin{aligned}
I_{2nd} = & \int_{\vec{K}_{mn}} \int_{\vec{K}_i} \int_{\vec{K}_{pq}} \int_{\omega_{mn}} \int_{\omega_i} \int_{\omega_{pq}} \Gamma_P^2 \left(\frac{\vec{K}_o \cdot \hat{K}_s}{\sqrt{K_s}} \right)^2 \\
& \delta[\omega_d - (\omega_{mn} + \omega_i + \omega_{pq})] S_o(\vec{K}_{mn}, \omega_{mn}) S_i(\vec{K}_i, \omega_i) \\
& \cdot S_o(\vec{K}_{pq}, \omega_{pq}) S a^2 \left\{ \frac{\Delta\rho}{2} \left[K_s - k_0(1 + \sin\theta_i) \right] \right\} \\
& d\omega_{pq} d\omega_i d\omega_{mn} d\vec{K}_{pq} d\vec{K}_i d\vec{K}_{mn}.
\end{aligned}
\tag{B.1}
$$

With the aid of the relationship between the wavenumber $\vec{K}_o$, $\vec{K}_i$ and the frequency ω_o, ω_i for ocean waves and ionospheric irregularities, as given in Eq. (1.23) and Eq. (2.23), and

the approximation of the the sampling function, the integral I_{2nd} reduces to

$$\begin{aligned} I_{2nd} = & \int_{\vec{K}_{mn}} \int_{\vec{K}_i} \int_{\vec{K}_{pq}} \Gamma_P^2 \left(\frac{\vec{K}_o \cdot \hat{K}_s}{\sqrt{K_s}} \right)^2 \\ & \sum_{m_1=\pm 1} \sum_{m_2=\pm 1} S_o(m_1 \vec{K}_{mn}) S_i(K_i) S_o(m_2 \vec{K}_{pq}) \\ & \cdot \delta(\omega_d + m_1 \sqrt{gK_{mn}} + \vec{K}_i \cdot \vec{v}_h + 2k_0 v_v \cos\theta_i + m_2 \sqrt{gK_{pq}}) \\ & \cdot \delta\left[K_s - k_0(1+\sin\theta_i)\right] d\vec{K}_{pq} d\vec{K}_i d\vec{K}_{mn}. \end{aligned} \tag{B.2}$$

The integrals are further simplified with the aid of the delta function constraints in (B.2). The $\vec{K}_{pq}$-integral is changed to $d\vec{K}_s$ as follows,

$$d\vec{K}_{pq} = d\vec{K}_s = K_s dK_s d\phi_s, \tag{B.3}$$

and K_s-integral is eliminated by setting $K_s = k_0(1+\sin\theta_i)$. Furthermore, defining Y and D_p, respectively, as

$$Y = \sqrt{K_{mn}},$$

and

$$D_p(Y, \phi_{mn}) = -m_1 \sqrt{gK_{mn}} - m_2 \sqrt{gK_{pq}},$$

their relationship may be given as

$$\begin{aligned} Y = & \frac{-D_p(Y, \theta_{mn})}{m_1 \sqrt{g}} \\ & - \frac{m_2 [g^2 (Y^4 + K_o^2 - 2K_o Y^2 \cos(\theta_{mn} - \theta_o))]^{1/4}}{m_1 \sqrt{g}}, \end{aligned} \tag{B.4}$$

where $\vec{K}_o = \vec{K}_{mn} + \vec{K}_{pq}$. The K_{mn}-integral may be changed to dD_p for a given θ_{mn} as,

$$dK_{mn} = 2Y \mid \frac{\partial Y}{\partial D_p} \mid_{\theta_{mn}} dD_p.$$

Based on the Jacobian transformation,

$$\mid \frac{\partial Y}{\partial D_p} \mid_{\theta_{mn}} = \frac{1}{\sqrt{g} \mid 1 + \frac{m_1 m_2 (Y^3 - Y K_o \cos(\theta_{mn} - \theta_o))}{[Y^4 + K_o^2 - 2K_o Y^2 \cos(\theta_{mn} - \theta_o)]^{3/4}} \mid}. \tag{B.5}$$

The D_p-integral is solved numerically based on another delta function constraint of Eq. (B.2). The value of $Y = Y^*$ may be sought through the Newton-Raphson method to satisfy

$$D_p(Y^*, \theta_{mn}) = \omega_o,$$

where ω_o is equal to $\omega_d + \vec{K}_i \cdot \vec{v}_h + 2k_0 v_v \cos\theta_i$. Thus, the integral becomes

$$\begin{aligned} I_{2nd}(\omega_d) = & \int_{\phi_{mn}} \int_{K_i} \int_{\phi_i} \int_{\phi_s} 2Y^* \Gamma_P^2 \left(\vec{K}_o \cdot \hat{K}_s \right)^2 \\ & \sum_{m_1 = \pm 1} \sum_{m_2 = \pm 1} S_o(m_1 \vec{K}_{mn}) S_i(K_i) S_o(m_2 \vec{K}_{pq}) \\ & \cdot \mid \frac{\partial Y}{\partial D_p} \mid_{\theta_{mn}, Y^*} d\phi_s d\phi_i dK_i d\phi_{mn}. \end{aligned} \tag{B.6}$$

Appendix C

Stationary Phase Approximation for Mixed-path Bistatic Case

Under the conditions stated in Section 4.3.2, the δ-integral of Eq. (4.22) may be determined via a stationary phase method. This method is a procedure for evaluation of integrals of the form [87]

$$I = \int_{-\infty}^{\infty} G(\delta) e^{jZ\Phi(\delta)} dx, \tag{C.1}$$

where Z is a large real number and $G(\delta)$ varies much slower than $\Phi(\delta)$. The rapid oscillations of the exponential term indicates that the significant non-zero contributions to the integral occur in regions where $d\Phi(\delta)/d\delta = 0$, which is referred to as the stationary phase points δ_s. Applying the stationary phase method to I gives

$$I \approx \sqrt{\frac{2\pi}{Z}} \frac{G(\delta_s)}{\sqrt{-j\frac{\partial^2 \phi(\delta_s)}{\partial \delta^2}}} e^{jZ\Phi(\delta_s)}. \tag{C.2}$$

The δ-integral

$$I_\delta = \int_\delta \frac{\rho_1'}{R_1} \sin[\theta_i(\rho_1)] \cos(\theta_O - \theta_1) F(\rho_2) \cdot e^{jK_s q(\cos\theta_s \cosh\mu \cos\delta + \sin\theta_s \sinh\mu \sin\delta)} d\delta.$$

may now be evaluated in view of the stationary phase method here. The oscillation phase part $\Phi(\delta)$ is identified as

$$\Phi(\delta) = \cos\theta_s \cosh\mu \cos\delta + \sin\theta_s \sinh\mu \sin\delta,$$

and the stationary phase condition on δ is given by

$$\frac{d\Phi(\delta)}{d\delta} = -\cos\theta_s \cosh\mu \sin\delta + \sin\theta_s \sinh\mu \cos\delta = 0.$$

Thus, the stationary phase point is solved to satisfy

$$\tan\delta_s = \tanh\mu \tan\theta_s. \tag{C.3}$$

Given the second derivative of $\Phi(\delta)$ as

$$\frac{\partial^2(\Phi(\delta))}{\partial\delta^2} = -(\cos\theta_s \cosh\mu \cos\delta + \sin\theta_s \sinh\mu \sin\delta),$$

the δ-integral may be approximated as

$$I_\delta \approx \sqrt{2\pi} \frac{\rho_1'}{R_1} \sin[\theta_i(\rho_1)] \cos(\theta_O - \theta_1) F(\rho_2) \cdot \frac{e^{jK_s q(\cos\theta_s \cosh\mu \cos\delta_s + \sin\theta_s \sinh\mu \sin\delta_s)}}{\sqrt{jK_s q(\cos\theta_s \cosh\mu \cos\delta_s + \sin\theta_s \sinh\mu \sin\delta_s)}} \tag{C.4}$$

With reference to the geometry of the ellipse in Fig. B.1, the direction of $\vec{K}_s$ will be shown to be perpendicular to the ellipse at the scattering point. Shifting the origin of the XOY plane to $(x_0, 0)$, the expression of the scattering point in the new X'O'Y' plane is given as

$$\begin{aligned} x' &= x - x_0 = q\cosh\mu\cos\delta, \\ y' &= y = q\sinh\mu\sin\delta. \end{aligned} \tag{C.5}$$

The tangent $\vec{T}$ at (x', y') to the ellipse curve is given by

$$\vec{T} = \frac{\partial x'}{\partial \delta}\hat{x} + \frac{\partial y'}{\partial \delta}\hat{y},$$

and its normal is

$$\begin{aligned} \vec{N} =& \frac{\partial x'}{\partial \mu}\hat{x} + \frac{\partial y'}{\partial \mu}\hat{y} \\ =& q \sinh\mu \cos\delta\hat{x} + q\cosh\mu\cos\delta\hat{y}, \end{aligned} \tag{C.6}$$

since μ and δ are orthogonal coordinates. The direction θ_N of the ellipse normal is shown to be the same as θ_s in Eq. (C.3). Furthermore, converting $\vec{\rho}_1'$ and ρ_2 to elliptic coordinate form gives the following relationship as

$$\vec{\rho}_2 \cdot \vec{N} = -\left(\frac{\rho_2}{\rho_1'}\right)\vec{\rho}_1' \cdot \vec{N}. \tag{C.7}$$

This equation implies that $\vec{N}$ bisects the angle between the foci as viewed from the scattering point.

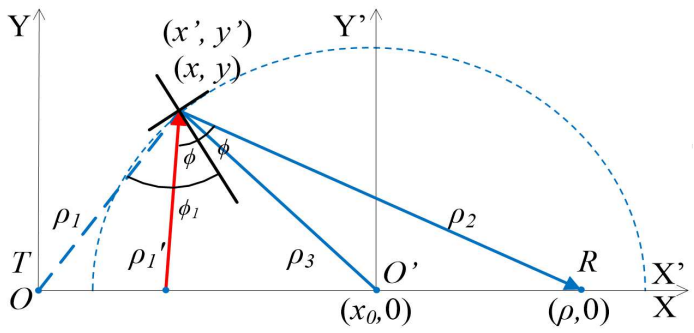

Figure C.1: Locus of the scattering points on X-Y plane.

With the aid of the ellipse geometry relationships, the evaluated δ-integral is further represented by the scattering range and angle information instead of μ and δ_s. As shown in Fig. B.1, the expression of $\vec{\rho}_3$ from (x, y) to $(x_0, 0)$ may be represented as

$$\vec{\rho}_3 = q\cosh\mu\cos\delta\hat{x} + q\sinh\mu\sin\delta\hat{y}.$$

Thus, the phase term in Eq. (C.4) may be written as

$$K_s q(\cos\theta_s \cosh\mu \cos\delta_s + \sin\theta_s \sinh\mu \sin\delta_s) = \vec{\rho}_3 \cdot \vec{K}_s. \tag{C.8}$$

On the other hand, $\vec{\rho}_3$ may also expressed as

$$\vec{\rho}_3 = (\vec{\rho}_1' - \vec{\rho}_2)/2.$$

Then, substituting Eq. (C.7) into $\vec{\rho}_3 \cdot \hat{N}$ gives

$$\vec{\rho}_3 \cdot \hat{N} = \rho_s \hat{\rho}_1' \cdot \hat{N}, \tag{C.9}$$

where $\rho_s = (\rho_1' + \rho_2)/2$ and noting that $\hat{\rho}_1' \cdot \hat{N} = \cos\phi$.

Combining the information in Eq. (C.8) and (C.9) and applying $\frac{1}{\sqrt{j}} = e^{-j\frac{\pi}{4}}$, the evaluation for I_δ becomes

$$I_\delta \approx \sqrt{2\pi}\frac{\rho_1'}{R_1}\sin[\theta_i(\rho_1)]\cos(\theta_O - \theta_1)F(\rho_2) \cdot \frac{e^{j\vec{\rho}_3\cdot\vec{K}_s}e^{-j\frac{\pi}{4}}}{\sqrt{\rho_s K_s \cos\phi}}. \tag{C.10}$$

Appendix D

Demodulation of the Mixed-Path Ionospheric Clutter with a FMCW Radar Source

The range and Doppler information of radio waves interacting with the ionosphere and ocean surface during mixed-path propagation may be extract by demodulating the received electric field for a FMCW radar source. The demodulation is the process which involves multiplying the acquired signal with the original transmitted signal followed by a low-pass filter [88]. In our analysis, the equation of the original transmitted FMCW current is rewritten here as

$$i_T(t_r) = I_0 \cos[2\pi(f_0 + \frac{\alpha t_r}{2})t_r], \quad -\frac{T_r}{2} \leq t < \frac{T_r}{2}, \tag{D.1}$$

where t_r is the time variable within the period T_r. All the other parameters are defined in Chapter 5. Furthermore, the first-order temporal field equation for the FMCW source in a

sweep interval (5.10) may be rewritten as

$$(E_0)_{1FM}(t_r) = E_c \cos[\omega_0 t_r + \alpha\pi t_r^2 + \Theta(t_r)], \qquad -\frac{T_r}{2} \leq t < \frac{T_r}{2}. \tag{D.2}$$

where E_c is a collection of irrelevant factors, and $\Theta(t_r)$ is summation of all the other phase terms with assumption that $\frac{d\Theta(t_r)}{dt_r} \ll (\omega_0 + \alpha\pi t_r)$. After absorbing I_0 into E_c, the demodulation of $(E_0)_{1FM}(t_r)$ gives,

$$\begin{aligned}
(E_0)^D_{1FM}(t_r) &= LPF\left\{i(t_r)(E_0)_{1FM}(t_r)\right\} \\
&= LPF\left\{E_c \cos\left[\omega_0 t_r + \alpha\pi t_r^2\right] \cos\left[\omega_0 t_r + \alpha\pi t_r^2 + \Theta(t_r)\right]\right\} \\
&= E_c/2 LPF\left\{\cos\left[2\omega_0 t_r + 2\alpha\pi t_r^2 + \Theta(t_r)\right] + \cos\left[-\Theta(t_r)\right]\right\} \\
&= E_c/2 \cos\left[-\Theta(t_r)\right]
\end{aligned} \tag{D.3}$$

where $(E_0)^D_{1FM}(t_r)$ represents the demodulation with respect to $(E_0)_{1FM}(t_r)$ and $LPF\cdot$ refers to the operation of an ideal low-pass filtering. As a result of the ideal demodulation, the exponential factor $e^{j(\omega_0 t_r + \alpha\pi t_r^2)}$ will be eliminated, the phase term will be replaced by its complex conjugation and the other factors remain the same.